

University of Alberta

**BIOPHYSICS UNDERLYING BISTABLE NEURONS WITH
BRANCHING DENDRITES**

by

Hojeong Kim

A thesis submitted to the Faculty of Graduate Studies and Research in partial fulfillment
of the requirements for the degree of

Doctor of Philosophy

in

Medical Sciences – Biomedical Engineering

© Hojeong Kim
Spring 2011
Edmonton, Alberta

Permission is hereby granted to the University of Alberta Libraries to reproduce single copies of this thesis and to lend or sell such copies for private, scholarly or scientific research purposes only. Where the thesis is converted to, or otherwise made available in digital form, the University of Alberta will advise potential users of the thesis of these terms.

The author reserves all other publication and other rights in association with the copyright in the thesis and, except as herein before provided, neither the thesis nor any substantial portion thereof may be printed or otherwise reproduced in any material form whatsoever without the author's prior written permission.

EXAMINING COMMITTEE

Dr. Kelvin Jones, Physical Education and Recreation, Biomedical Engineering

Dr. Keir Pearson, Department of Physiology, Centre for Neuroscience

Dr. David Bennett, Faculty of Rehabilitation Medicine, Centre for Neuroscience

Dr. Jack Tuszynski, Department of Physics, Division of Experimental Oncology

Dr. Youssef Belhamadia, Department of Mathematics, Biomedical Engineering

Dr. Randall Powers, Physiology and Biophysics, University of Washington

ABSTRACT

The goal of this thesis is to investigate the biophysical basis underlying the nonlinear relationship between firing response and current stimulation in single motor neurons. After reviewing the relevant motoneuron physiology and theories that describe complex dendritic signaling properties, I hypothesize that at least five passive electrical properties must be considered to better understand the physiological input-output properties of motor neurons in vivo: input resistance, system time constant, and three signal propagation properties between the soma and dendrites that depend on the signal direction (i.e. soma to dendrites or vice versa) and type (i.e. direct (DC) or alternating (AC) current). To test my hypothesis, I begin with characterizing the signal propagation of the dendrites, by directly measuring voltage attenuations along the path of dendrites of the type-identified anatomical neuron models. Based on this characterization of dendritic signaling, I develop the novel realistic reduced modeling approach by which the complex geometry and passive electrical properties of anatomically reconstructed dendrites can be analytically mapped into simple two-compartment modeling domain without any restrictive assumptions. Combining mathematical analysis and computer simulations of my new reduced model, I show how individual biophysical properties (system input resistance, time constant and dendritic signaling) contribute to the local excitability of the dendrites, which plays an essential role in activating the plateau generating membrane mechanisms and subsequent nonlinear input-output relations in a single neuron. The biophysical theories and computer simulations in this thesis are primarily applied to motor

neurons that compose the motor neuron pool for control of movement. However, the general features of the new reduced neuron modeling approach and important insights into neuronal computations are not limited to this area. My findings can be extended to other areas including artificial neural networks consisting of single compartment processors.

ACKNOWLEDGEMENTS

I am heartily thankful to my PhD supervisor, Dr. Kelvin Jones. This thesis would not have been possible without his patient guidance and sincere mentorship that have made me realize for myself not only how to do research as a scientist, but also what to do to be a respected scholar. I would also like to thank him for his endless support and encouragement that have been a wonderful boost for my morale throughout my PhD training.

I would like to thank my committee members, Dr. Keir Pearson and David Bennett, for their careful reading of my thesis and valuable advices that helped improve its presentation. I would also like to thank Dr. David Collins for his great encouragement during my ups and downs. Thanks must be given to Dr. Jack Tuszynski, Youssef Belhamadia and Randall Powers for being part of my examination committee.

It is a pleasure to thank my student colleagues, Chad Lorenz, Austin Bergquist, Yoshino Okuma and Juan Forero, for their friendship and support. I also want to thank Maisie Goh for assisting me in many different ways.

Finally, I am especially grateful to my parents and brother for their encouragement and belief in me in completing this degree. I wish to thank my wife, Kyoungsuk, and my son, Yeongjun, for their enduring patience and commitment for my PhD study. To them I dedicate this thesis.

TABLE OF CONTENTS

| | |
|--------------------------------------------------------------------------------------------------|-----------|
| CHAPTER 1:INTRODUCTION | 1 |
| 1.1 PREFACE..... | 1 |
| 1.2 MOTOR UNITS..... | 2 |
| 1.3 EXPERIMENTAL OBSERVATIONS OF MOTOR NEURON ELECTRICAL PROPERTIES | 2 |
| 1.3.1 Passive properties: Subthreshold response..... | 4 |
| 1.3.2 Active properties: Action potential | 4 |
| 1.3.3 Active properties: Spike train..... | 7 |
| 1.3.4 Active properties: Bistable firing behaviour | 8 |
| 1.4 THEORETICAL FOUNDATIONS OF NEURONAL ACTIVITY..... | 9 |
| 1.4.1 Passive properties: Subthreshold response..... | 10 |
| 1.4.2 Active properties: Action potential | 12 |
| 1.4.3 Active properties: Spike train..... | 16 |
| 1.4.4 Passive properties: Functional significance of branching dendrites . | 21 |
| 1.4.5 Active properties: Bistable firing behaviour | 26 |
| 1.5 COMPUTATIONAL MODELS FOR MOTOR NEURONS. | 26 |
| 1.6 THESIS OUTLINES | 30 |
| 1.6.1 Chapter 2: Formulation of a new reduced model for single MNs..... | 31 |
| 1.6.2 Chapter 3: Roles of asymmetric dendritic signaling in the bistability of MN models..... | 31 |
| 1.6.3 Chapter 4: Influence of back-propagating APs on model bistability | 32 |
| 1.6.4 Chapter 5 | 32 |
| 1.7 BIBLIOGRAPHY FOR CHAPTER 1..... | 33 |

**CHAPTER 2: Derivation of cable parameters for a reduced model
that retains asymmetric voltage attenuation of
reconstructed spinal motor neuron dendrites 41**

| | | |
|------------|-------------------------------------------------------------------|-----------|
| 2.1 | INTRODUCTION..... | 43 |
| 2.2 | METHODS | 46 |
| 2.2.1 | Preparation of motor neuron anatomy..... | 46 |
| 2.2.2 | Assignment of passive membrane properties..... | 46 |
| 2.2.3 | Generation of attenuation curves and voltage decay constant | 48 |
| 2.3 | RESULTS | 50 |
| 2.3.1 | Voltage attenuation in realistic motor neuron models | 50 |
| 2.3.2 | Voltage attenuation, motor neuron type and input resistance | 54 |
| 2.3.3 | Development of two-compartment motor neuron models | 57 |
| 2.3.4 | Direction-dependent current attenuation..... | 66 |
| 2.3.5 | Global sensitivity analysis..... | 67 |
| 2.3.6 | Input resistance in the dendritic compartment | 71 |
| 2.4 | DISCUSSION | 73 |
| 2.4.1 | Critical assessment of the models and results | 73 |
| 2.4.2 | Comparison with other studies..... | 76 |
| 2.5 | CONCLUSION | 77 |
| 2.6 | APPENDIX FOR CHAPTER 2..... | 77 |
| 2.7 | BIBLIOGRAPHY FOR CHAPTER 2..... | 79 |

**CHAPTER 3: Asymmetric electrotonic coupling between the soma
and dendrites alters the bistable firing behaviour of
reduced models 86**

| | | |
|------------|----------------------------------------------|-----------|
| 3.1 | INTRODUCTION..... | 86 |
| 3.2 | METHODS | 89 |
| 3.2.1 | Symmetric and asymmetric reduced models..... | 89 |
| 3.2.2 | Active dynamics of models: bistability..... | 95 |

| | | |
|------------|-------------------------------------------------------------------------------------------|------------|
| 3.2.3 | Comparison to anatomical models | 97 |
| 3.3 | RESULTS | 97 |
| 3.3.1 | Theory: passive input-output properties with respect to DDVA..... | 98 |
| 3.3.1.1 | Input resistance at dendrites | 98 |
| 3.3.1.2 | Multiple inputs and single output relationship..... | 101 |
| 3.3.2 | Bistability of asymmetric model | 103 |
| 3.3.3 | DDVA dependency of firing patterns and bistability..... | 107 |
| 3.3.3.1 | Insights from bifurcation analysis..... | 107 |
| 3.3.3.2 | Characteristic index space..... | 110 |
| 3.3.3.3 | Firing patterns on DDVA domain..... | 113 |
| 3.3.4 | Distribution of physiological DDVA values | 115 |
| 3.4 | DISCUSSION | 117 |
| 3.4.1 | Interaction of coupling parameters with firing patterns | 117 |
| 3.4.2 | Importance of initial values of coupling parameters for bistable firing behaviour..... | 118 |
| 3.4.3 | Comparison with other studies..... | 120 |
| 3.4.4 | Limitations in current modeling approach | 122 |
| 3.5 | CONCLUSION | 124 |
| 3.6 | APPENDIX FOR CHAPTER 3 | 124 |
| 3.7 | BIBLIOGRAPHY FOR CHAPTER 3 | 125 |

| | |
|---------------------------------------------------------------------|-------------------------------------|
| CHAPTER 4: Frequency response of the passive dendritic trees | |
| that constrains the bistable firing behaviour of a | |
| reduced neuron model..... | |
| | 132 |
| 4.1 | INTRODUCTION..... |
| | 132 |
| 4.2 | METHODS |
| | 135 |
| 4.2.1 | Anatomical neuron models..... |
| | 135 |
| 4.2.2 | Frequency response analysis |
| | 137 |
| 4.2.3 | Reduced neuronal modeling..... |
| | 138 |
| 4.2.3.1 | Passive electrical properties |
| | 138 |

| | | |
|--------------------------------------------|---------------------------------------------------------------------------------------|------------|
| 4.2.3.2 | Active electrical properties | 139 |
| 4.2.4 | Simulation | 140 |
| 4.3 | RESULTS | 141 |
| 4.3.1 | Frequency response of the anatomically reconstructed models | 142 |
| 4.3.2 | Expansion of two-compartment modeling framework..... | 146 |
| 4.3.3 | Frequency response of reduced neuron models | 149 |
| 4.3.4 | Bistability of the reduced model with AC signaling property of the dendrites | 154 |
| 4.3.4.1 | Hyperexcitable dendrite in the DC/AC-RM | 154 |
| 4.3.4.2 | Bistable firing patterns | 155 |
| 4.3.5 | Dependance of the reduced model dynamics on dendritic AC signaling property..... | 157 |
| 4.3.5.1 | Insights from bifurcation analysis..... | 157 |
| 4.3.5.2 | Bistable solution space..... | 160 |
| 4.3.6 | Spatial relationship of the bistable solution space | 163 |
| 4.4 | DISCUSSION | 165 |
| 4.4.1 | Passive versus active propagation of action potentials in motor neurons | 165 |
| 4.4.2 | Retrograde signaling of action potentials for short-term plasticity. | 166 |
| 4.4.3 | Type-dependency of AC signal attenuation property..... | 166 |
| 4.4.4 | Comparison with other studies..... | 169 |
| 4.4.5 | Limitations in current modeling approach | 171 |
| 4.5 | CONCLUSION | 172 |
| 4.6 | APPENDIX A FOR CHAPTER 4..... | 172 |
| 4.7 | APPENDIX B FOR CHAPTER 4 | 174 |
| 4.8 | BIBLIOGRAPHY FOR CHAPTER 4..... | 175 |
| CHAPTER 5: GENERAL DISCUSSION | | 180 |
| 5.1 | THESIS SUMMARY..... | 180 |

| | | |
|------------|----------------------------------------------------------------------------------|------------|
| 5.2 | ASYMMETRIC SIGNALING IN DENDRITIC NEURONS | 181 |
| 5.3 | PHYSIOLOGICAL REDUCED MODELING FRAMEWORK..... | 181 |
| 5.4 | BIOPHYSICAL PRINCIPLE UNDERLYING MOTOR NEURON BISTABILITY | 183 |
| 5.5 | FUTURE WORKS: REALISTIC MOTOR UNIT POOL MODELING..... | 184 |
| 5.6 | BIBLIOGRAPHY FOR CHAPTER 5..... | 187 |

LIST OF TABLES

| | |
|--------------------------------------------------------------------------------------------------------------|-----|
| Table 2-1. Passive membrane properties and electrotonic properties | 47 |
| Table 3-1. Standard parameter values for the asymmetric model | 94 |
| Table 4-1. Passive membrane properties of the type-identified anatomical motor neuron models | 136 |

LIST OF FIGURES

| | |
|---------------------------------------------------------------------------------------------------------------------------------------------------------------------------------|-----|
| Figure 1-1. Hierarchy of experimental observations on electrical properties of cat MNs..... | 3 |
| Figure 1-2. Schematic diagram of a single action potential and underlying conductances in generic adult motor neurons..... | 6 |
| Figure 1-3. Graphical representation of membrane potential (V) response over time (t) (top) onto the phase plane consisting of V & recovery variable (n) (bottom) | 15 |
| Figure 1-4. Four bifurcation mechanisms underlying the transition from the resting to sustained spiking activity as the intensity of the injected current increases..... | 18 |
| Figure 1-5. Schematic reduction of a neuron with synaptic inputs into a two-port network..... | 25 |
| Figure 1-6. Computational neuron modeling frameworks..... | 28 |
| | |
| Figure 2-1. Morphology of MNs and DDVA with curve fitting..... | 52 |
| Figure 2-2. Relationship between η and RN for V1 (Case I and II) | 54 |
| Figure 2-3. Relationship between η and R_N , and between P and D for all six models | 56 |
| Figure 2-4. Implicit and explicit models | 59 |
| Figure 2-5. Distribution of passive membrane parameters according to RN and D with $\tau_m = 7.1$ ms..... | 68 |
| Figure 2-6. Input resistance of two-compartment models..... | 72 |
| | |
| Figure 3-1. Schematic diagram of the asymmetrically coupled models | 91 |
| Figure 3-2. Bistable firing patterns of the asymmetric model..... | 105 |
| Figure 3-3. Bifurcation diagrams in the asymmetric model with physiological (a1 & b1, $A_{SD}(0.89) \gg A_{DS}(0.26)$), symmetric (a2 & b2, $A_{SD}(0.5) =$ | |

| | |
|--------------------------------------------------------------------------------------------------------------------------------------------------------------------------------------------------------------------------------------------------------------------------------------------|-----|
| $A_{DS}(0.5)$), and non-physiological (a_3 & b_3 , $A_{SD}(0.26) \ll A_{DS}(0.89)$) coupling..... | 108 |
| Figure 3-4. Distribution of characteristic indexes (CIs) for the asymmetric model on DDVA domain | 111 |
| Figure 3-5. Firing patterns of the asymmetric model on DDVA domain | 114 |
| Figure 3-6. Coincidence of bistable solution space with physiological DDVA properties on DDVA domain..... | 116 |
| Figure 3-7. Variability of bistable solution space on DDVA domain..... | 119 |
| | |
| Figure 4-1. Spatial frequency response of an anatomically reconstructed motor neuron model..... | 144 |
| Figure 4-2. Comparison of the frequency response between the DC/AC-RM, DC- RM and anatomical motor neuron model | 152 |
| Figure 4-3. Bistable firing behaviour of the DC/AC-RM | 156 |
| Figure 4-4. Bifurcation structures at the soma (left column) and dendrite (right column) of the DC/AC-RM with increasing AC signal attenuations ($V_{ASDAC} = 0.08, 0.49$ and 0.88) and constant DC signal attenuations ($V_{ASDDC}=0.89$ and $V_{ADSDC}=0.26$)..... | 158 |
| Figure 4-5. Bistable solution space of the DC/AC-RM | 162 |
| Figure 4-6. Coincidence of bistable solution space with physiological voltage attenuation properties | 164 |
| Figure 4-7. Relationship between the exponential decay coefficient (η) of the amplitude attenuation and input resistance (R_N) for six type-identified anatomical motor neuron models..... | 168 |

LIST OF ABBREVIATIONS AND SYMBOLS

| | |
|-------------------------------|----------------------------------------------------------------------------------------------------------------------------------------|
| R_N | input resistance at soma (M Ω) |
| $A_{SD}(D) = V_D/V_S$ | voltage attenuation factor from soma to dendrites at distance, D, from soma |
| $A_{DS}(D) = V_S/V_D$ | voltage attenuation factor from dendrites to soma at distance, D, from soma |
| η_{SD} | decay constant for voltage attenuation in the soma to dendrites direction (μm) |
| η_{DS} | decay constant for voltage attenuation in the dendrites to soma direction (μm) |
| $P(D) = SA_{soma}/SA_{total}$ | morphological factor for two-compartment model; the ratio of somatic surface area to total surface area at distance, D, from soma |
| $V_S = V_{m,S} - E_{leak}$ | deviation of somatic membrane potential from reversal potential of leak ion channel in soma of two-compartment models (mV) |
| $V_D = V_{m,D} - E_{leak}$ | deviation of dendritic membrane potential from reversal potential of leak ion channels in dendrite of two-compartment models (mV) |
| I_S | injected current density at soma in two-compartment models, normalized by somatic surface area ($\mu\text{A}/\text{cm}^2$) |
| I_D | injected current density at dendrite in two-compartment models, normalized by dendritic surface area ($\mu\text{A}/\text{cm}^2$) |
| $G_{C,S}$ | direction-dependent passive coupling conductance from soma to dendrite in explicit two-compartment model ($\mu\text{S}/\text{cm}^2$) |

| | |
|----------------------------------------------|----------------------------------------------------------------------------------------------------------------------------------------------------|
| $G_{C,D}$ | direction-dependent passive coupling conductance from dendrite to soma in explicit two-compartment model ($\mu\text{S}/\text{cm}^2$) |
| G_m | uniform passive membrane conductance in explicit two-compartment model ($\mu\text{S}/\text{cm}^2$) |
| G_C | directionless passive coupling conductance in implicit two-compartment model ($\mu\text{S}/\text{cm}^2$) |
| $G_{m,S}$ | passive membrane conductance of soma in implicit two-compartment model ($\mu\text{S}/\text{cm}^2$) |
| $G_{m,D}$ | passive membrane conductance of dendrite in implicit two-compartment model ($\mu\text{S}/\text{cm}^2$) |
| C_m | uniform passive membrane capacitance for two-compartment models ($\mu\text{F}/\text{cm}^2$) |
| $\tau_0 = \tau_m$ | passive membrane time constant for all models (ms) |
| τ_l | equalizing time constant for all models (ms) |
| C_0, C_1 | coefficients used to form linearly independent combination of exponential decays (mV) |
| $r_{N,implicit}, r_{N,explicit}$ | input resistance at somatic part in implicit and explicit models respectively, normalized by somatic surface area ($\text{M}\Omega\text{-cm}^2$) |
| $A_{SD,implicit}^V(D), A_{SD,explicit}^V(D)$ | voltage attenuation factor for soma to dendrite direction at distance, D, from soma; used in implicit and explicit models |
| $A_{DS,implicit}^V(D), A_{DS,explicit}^V(D)$ | voltage attenuation factor for dendrite to soma direction at distance, D, from soma; used in implicit and explicit models |
| R_{eff} | effective membrane resistivity for calculating passive membrane time constant in two-compartment models ($\text{M}\Omega\text{-cm}^2$) |

| | |
|----------------------------------------------|---------------------------------------------------------------------------------------------------------------------------------|
| $A_{SD,implicit}^I(D), A_{SD,explicit}^I(D)$ | current attenuation factor for soma to dendrite direction at distance, D, from soma; used in implicit and explicit models |
| $A_{DS,implicit}^I(D), A_{DS,explicit}^I(D)$ | current attenuation factor for dendrite to soma direction at distance, D, from soma; used in implicit and explicit models |
| <i>DDVA</i> | Direction Dependant Voltage Attenuation |
| A_{SD} | voltage Attenuation factor from Soma to Dendrites |
| A_{DS} | voltage Attenuation factor from Dendrites to Soma |
| <i>PIC</i> | Persistent Inward Current |
| <i>CI</i> | Characteristic Index |
| <i>TTP</i> | Time To onset of Plateau potential |
| <i>TES</i> | Time to End of Somatic spiking |
| <i>DSF</i> | Difference in Spiking Frequency |
| <i>VGIC</i> | Voltage Gated Ion Channel |
| <i>AC</i> | Alternating Current |
| <i>DC</i> | Direct Current |
| VA_{SD}^{DC} | Voltage Attenuation factor from Soma to Dendrites with DC input |
| VA_{DS}^{DC} | Voltage Attenuation factor from Dendrites to Soma with DC input |
| VA_{SD}^{AC} | Voltage Attenuation factor from Soma to Dendrites with AC input |

CHAPTER 1: INTRODUCTION

1.1 PREFACE

Theoretical neuroscience using computational methods (also called computational neuroscience) has grown tremendously since Hodgkin and Huxley demonstrated that the computational membrane model can be tightly connected to the biological phenomenon of action potentials and useful to understand the underlying mechanisms (Hodgkin and Huxley, 1952). Furthermore, our view on the roles of highly branching dendritic trees attached to their cell bodies (Ramón y Cajal, 1933) was changed by the Rall's theoretical studies for the passive dendrites (Rall, 1957; Rall et al., 1995). His biophysical model of the dendrites (i.e. cable) has served as the theoretical foundation in many experimental and computational studies that have investigated the neuronal output behaviour (i.e. action potentials) in response to synaptic inputs spatially and temporally distributed over the dendritic trees. More recently, it has been clear that voltage-gated ionic channels distributed over the dendrites are actively involved in modulating synaptic effects (Stuart et al., 1999). In this thesis, I focus on the roles of the dendrites including active membrane mechanisms that are responsible for the complex output behaviour of ventral horn motor neurons (MNs) in the mammalian spinal cord, which are the final path to excitation of muscle and production of movement. Combining mathematical analysis and computer simulations, I identify the essential properties of the dendrites and derive biophysical principles underlying *bistable output firing behaviour* of motor neurons (Hounsgaard et al., 1984). The theory established in this thesis will serve a basis for understanding how the dendritic signaling contributes to nonlinear dynamics of neurons including dendritic voltage-gated channels.

1.2 MOTOR UNITS

The spinal cord makes up the central nervous system (CNS) together with the brain. It transmits motor commands from the brain down to the rest of the body, as well as sensory information from the body up to the brain. In addition, the spinal neural circuits consisting of MNs and interneurons serve functionally independent operation modes without brain intervention, including various reflex actions (Sherrington, 1906) and central pattern generation (CPG) of rhythmic movements (Hooper, 2000). A single α -MN in the ventral horn of the spinal cord and the muscle fibers it innervates form the motor unit, which is the fundamental element for all motor output. In general, the MNs within the motor neuron pool controlling a single muscle have been classified into three types according to the mechanical properties of their corresponding muscle fibers: Slow twitch (S-type), Fatigue-Resistant fast twitch (FR-type) and Fatiguable Fast twitch (FF-type) (Burke et al., 1973). Several electrical properties (i.e. input resistance, time constant and rheobase) of MNs have been also reported to be correlated to MN types in the population (Zengel et al., 1985). Thus all movement depends on the pattern of recruitment and rate modulation of motor units (Fuglevand et al., 1993), which are determined by electrical properties of MNs.

1.3 EXPERIMENTAL OBSERVATIONS OF MOTOR NEURON ELECTRICAL PROPERTIES

To identify the essential electrical properties determining the complex firing response of MNs to current input, electrophysiological data mainly from the lumbar α -MNs of the adult cat was hierarchically reviewed from passive subthreshold to active whole-cell behaviour (Fig. 1-1). The electrical properties identified in each hierarchical level were used to develop the realistic neuron modeling framework. The cat α -MNs are the first mammalian neurons that have been extensively studied using sharp microelectrode to the soma for their

activation properties and manners targeting the various types of skeletal muscle fibres (Brock et al., 1952; Eccles et al., 1957).

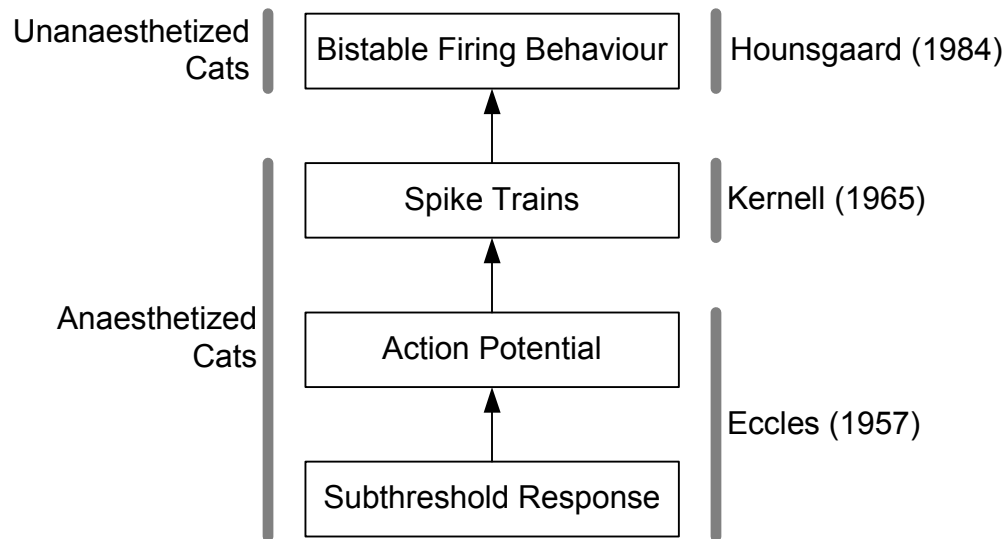


Figure 1-1. Hierarchy of experimental observations on electrical properties of cat MNs. Note that the whole-cell behaviour (i.e. bistable firing behaviour) was observed in the unanaesthetized preparations where the active membrane mechanisms in the dendrites were intact.

1.3.1 *Passive properties: Subthreshold response*

The onset of action potentials in the soma is determined by the subthreshold response of membrane potential to the current input below the rheobase (i.e. current threshold for triggering a single action potential, I_{rh}). Under little synaptic activities in anaesthetized adult cat preparations, the membrane potential at the soma of MNs tends to rest at around -70 mV (Eccles et al., 1957). When a long stimulating step of current with a low intensity (e.g. 1 nA) is injected to the soma, the membrane potential starts to rapidly depolarize and gradually approach to the steady-state value. This time course of voltage response in the subthreshold region has been characterized with the system time constant (τ_m) representing the rate of changes in membrane potential, and the input resistance (R_N) indicating the membrane excitability *i.e.* the higher R_N , the less current is needed for depolarizing the cell to the threshold for spike discharge. τ_m is determined by membrane resistance (R_m) multiplied by membrane capacitance (C_m), whereas R_N is determined as a function of R_m and cytoplasmic resistance (R_i) along with dendritic geometry. It is important to note that the properties (τ_m and R_N) of the subthreshold transient response have been also suggested to be tightly related to MN types (Zengel et al., 1985).

The appearance of the transient membrane potential in the subthreshold region is mainly mediated by two passive membrane currents, leak (I_L) and capacitive current (I_C) (Hodgkin and Huxley, 1952). However it should be noted that other types of active membrane mechanisms (e.g. hyperpolarization-activated non-selective cation currents (I_h), inward rectified K^+ currents (I_{Kir}), background synaptic activities or electrogenic pump) may influence the subthreshold membrane dynamics (Destexhe and Pare, 1999; Ito and Oshima, 1965).

1.3.2 *Active properties: Action potential*

When the intensity of the depolarizing current step is large enough for membrane potential to exceed the threshold for a spike or action potential (i.e. I_{th}), the cat MNs generate a positive voltage overshoot with an amplitude of around 80–90 mV during 1–2 ms, followed by a negative voltage undershoot with an amplitude of around 3–4.9 mV during 65–160 ms that ultimately returns to the resting membrane potential. In general, a single action potential consists of four different states in a cycle: resting, rising, falling, afterhyperpolarizing (AHP) and back to the initial resting state (refer to Fig. 1-2).

When analyzed using voltage clamp recording technique, each state during an action potential is governed by the balance between inward and outward ionic currents that are typically time- and voltage-dependent. The rapid rising state is mainly mediated by inward fast Na^+ currents ($I_{Na,f}$) whose conductance is progressively increased by the positive feedback mechanism (i.e. activation of voltage gated Na^+ channels by the depolarization caused by the influx of $I_{Na,f}$). During the falling state, outward delayed rectified K^+ currents ($I_{K,Dr}$) with slow kinetics pull down the depolarized membrane potential even below the resting voltage level along with the inactivation of $I_{Na,f}$. Finally K^+ currents ($I_{K(Ca)}$) activated by Ca^{2+} influx through high voltage activated Ca^{2+} channels ($I_{Ca,N}$) shapes the time course of membrane potential during AHP state. It is noted that other types of active membrane mechanisms are also likely to be involved to modulate the shape of an action potential (Hornby et al., 2002).

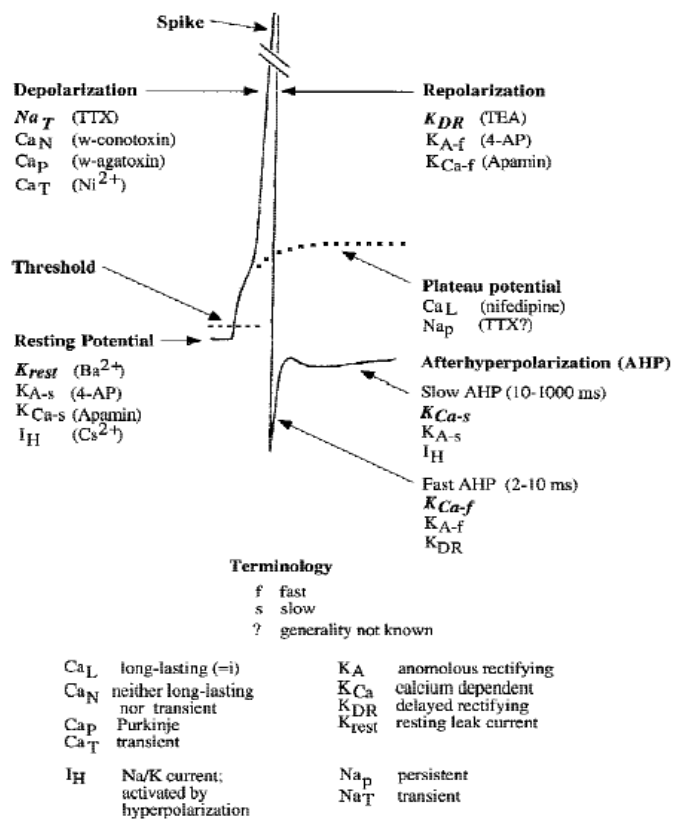


Figure 1-2. Schematic diagram of a single action potential and underlying conductances in generic adult motor neurons. The major conductance responsible for each state of the spike cycle is shown in bold italics. Plateau potential mediated by Ca^{2+} and Na^{+} currents is indicated with a dotted line (Adopted from Hornby et al., 2002).

1.3.3 *Active properties: Spike train*

The MNs can fire spikes tonically (i.e. spike train) when stimulated with a step of suprathreshold current that is typically higher than what is needed to evoke a single action potential by about 1.5 fold. The temporal pattern of the spike train has been characterized measuring variations of instantaneous firing frequency in response to a wide range of long lasting suprathreshold current steps (Granit et al., 1963; Kernell, 1965b). These studies have showed that the firing rates of MNs gradually decrease as a function of time (i.e. spike-frequency adaptation) with constant current intensity and the repeated spiking may disappear at a current stimulation which is strong enough to diminish the spike size.

The relationship between output firing rates (f) and steady current intensity (I) has been characterized with two straight lines: a shallow slope line over a lower frequency range (called primary range) and a steep slope line over a higher-frequency (called secondary range) (Kernell, 1965a). The frequency range higher than the secondary range has sometimes been referred to as a tertiary range with the line slope that has been suggested to be typically flatter than in the secondary range (Schwindt, 1973). The f - I relation below the primary range (called subprimary) may also be functionally important in rats (Manuel et al., 2009).

Possible electrophysiological mechanism underlying the secondary range was first suggested to be correlated to the actual manner of AHP conductance summation (called saturating summation) (Baldissera et al., 1978). Although the realistic AHP model could reproduce the f - I relationship of MNs including secondary range firing, the more extensive voltage clamp analysis revealed the presence of the voltage-dependant persistent inward currents (PICs) that are likely to be involved in the steep f - I relation over the higher frequency range (Schwindt and Crill, 1982). Even for the MNs in anaesthetized cats, PICs were observed to be already activated at subthreshold potentials and gradually activated as the membrane potential gets more depolarized (Schwindt and Crill, 1980a; Schwindt

and Crill, 1977; Schwindt and Crill, 1980c). Thereafter it has been suggested that PIC channels may provide an intrinsic source of depolarizing currents during the secondary range in the f-I relationship.

1.3.4 *Active properties: Bistable firing behaviour*

The experimental observations of the PICs by Schwindt and Crill have brought researchers' attention to the nonlinearities in the firing behaviour of the spinal MNs. The consequence of the fully activated PICs responsible for generating plateau potentials has been shown to be related to the sustained firing of cat MNs in the absence of external driving current (Hounsgaard et al., 1984). Thus the MNs can stay in either two stable states that can be switched by brief excitatory and inhibitory current pulses. For example, the MNs with PICs may initiate and sustain spikes by brief excitatory input, and turn back to the resting state by brief inhibitory input. This phenomenon has been referred as *bistable firing behaviour*.

Typically using the triangular current stimulation to the soma, the bistable firing behaviour of MNs has been characterized in terms of two features: 1) counter-clockwise frequency hysteresis in the f-I relationship (Lee and Heckman, 1998a; Lee and Heckman, 1998b), and 2) sustained firing during the descending phase of current stimulation below the current threshold for the spiking during the ascending phase (Bennett et al., 2001). The first feature of the counter-clockwise f-I curve also implies that during fully bistable firing action potentials may propagate into the dendrites and influence on the activation of the PICs mediated by L-type Ca^{2+} channels (Carlin et al., 2000a; Hounsgaard and Mintz, 1988; Li and Bennett, 2003; Schwindt and Crill, 1980b). Based on above two features of f-I relationship, four types of firing behaviour in spinal motor neurons have been classified in the rat MNs (Bennett et al., 2001): Type I (no frequency hysteresis and sustained firing), Type II (clockwise frequency hysteresis and no sustained firing) Type III (no frequency hysteresis but sustained firing) and Type IV (counter-clockwise frequency hysteresis and sustained firing). Type IV firing is

comparable to the fully bistable firing that has been observed mainly in large input resistance MNs (Lee and Heckman, 1998b).

The spatial distribution of the PIC channels responsible for the nonlinear (i.e. bistable) firing of MNs have been investigated both experimentally and computationally, showing that the PIC channels are concentrated on the dendritic branches physically distal to the soma i.e. 300-500 μm (Ballou et al., 2006; Carlin et al., 2000b; Elbasiouny et al., 2005; Grande et al., 2007; Heckman et al., 2003). Another indirect evidence for the dendritic localization of PIC channels is that a sequence of excitatory synaptic inputs to the dendrites gave rise to progressively lower the voltage threshold for generating plateau potential by ‘warming up’ the PIC channels (Bennett et al., 1998; Svirskis and Hounsgaard, 1997).

The voltage sensitivity of PIC channels in the dendrites is also modulated by metabotropic receptors activated by various neurotransmitters, including monoamines (e.g. norepinephrine and serotonin) deriving from descending tracts originating in the brainstem. Recently, it has become clear that neuromodulatory control of voltage gated channels in motor neuron dendrites is essential in specifying both electrical properties and nonlinear dynamics of MNs (Lee and Heckman, 2000).

1.4 THEORETICAL FOUNDATIONS OF NEURONAL ACTIVITY

Having reviewed the relevant motoneuron physiology, it became obvious that to better understand the bistable firing behaviour of MNs, not only active membrane mechanisms responsible for spiking at the soma and plateau potential in the dendrites but also dendritic signaling properties determining the interaction between those physically separated conductances should be taken into account in a unified modeling framework. It was not surprising that the biophysically plausible models have been derived to figure out the mechanisms underlying

experimental observations on neuronal activities in different levels (Fig. 1-1), followed by the abstract models to further use the powerful mathematical tools. One of the important theoretical strategies to study neuronal excitability has been the usage of the dynamical systems theory, by which many fundamental insights into the generation of action potentials has been suggested. In particular, the reduced modeling framework has been extensively used due to its favor to mathematical analysis (Mainen and Sejnowski, 1996; Sejnowski et al., 1988).

1.4.1 *Passive properties: Subthreshold response*

The resting transmembrane potential (or voltage, V_m) of a neuron is determined by ion movement (or ionic current, I_i) flowing through various types of proteins (i.e. ion channels and pumps) across the lipid bilayer membrane. The unbalanced concentration of individual ions inside and outside the cell gives rise to electrochemical gradient across the membrane, which in turn provides the intrinsic driving force exerting ions to move passively. This biological battery has been quantified by measuring membrane potential (called equilibrium or reversal potential, E_{rev}) at which I_i is zero. For a particular ion species (i), E_{rev} can be calculated by the following Nernst equation.

$$E_{rev} = V_m (I_i = 0) = \frac{RT}{zF} \ln \frac{[C]_{out}}{[C]_{in}} \quad (1-1)$$

where R is the gas constant (1.98 cal/°K-mol); T is absolute temperature (°K); z is the valence of the ion (dimensionless); F is Faraday's constant (96,480 C/mol); $[C]$ is the ion concentration.

To describe the dynamic response of V_m to various types of I_i and current stimulation in the perfectly voltage-clamped membrane, the electrical circuit model equivalent to the biological membrane was first proposed by Hodgkin & Huxley (1952) that consists of a membrane capacitance (C_m) per unit area (corresponding to lipid bilayer membrane) and various types of membrane

conductances (G_m) per unit area (corresponding to ionic channels) in parallel. Applying Kirchhoff's current law to the equivalent circuit, the total ionic current flowing across a patch of membrane (I_m) becomes the sum of the capacitive (I_C) and various types of ionic currents (I_i for a specific type) governed by Ohm's law,

$$I_m = I_C + \sum I_i = C_m \frac{dV_m}{dt} + \sum G_{m,i} (V_m - E_{rev,i}) \quad (1-2)$$

where the difference between V_m and $E_{rev,i}$ represents the electromotive force for the specific ion, i .

G_m can be either linear or nonlinear. A linear conductance exhibits a linear relation between I_i and V_m (I-V relation is always straight line), whereas a nonlinear conductance varies depending on both membrane potential and time. At the resting state, voltage- and time-dependent membrane conductances are typically assumed to be zero thus the resting potential (V_r) are determined by various types of leaky ion channels (e.g. Na^+ , K^+ and Cl^-). Thus the resting potential is determined by the linear conductances applying Thévenin's theorem¹ to the equivalent circuit membrane,

$$V_r = \frac{G_{K,Leak} E_K + G_{Na,Leak} E_{Na} + G_{Cl,Leak} E_{Cl}}{G_{K,Leak} + G_{Na,Leak} + G_{Cl,Leak}} \quad (1-3)$$

The resting potential may be also estimated in terms of ion permeability in accordance with Goldman-Hodgkin-Katz (GHK) equation,

$$V_r = \frac{RT}{F} \ln \frac{P_K [K^+]_{out} + P_{Na} [Na^+]_{out} + P_{Cl} [Cl^-]_{in}}{P_K [K^+]_{in} + P_{Na} [Na^+]_{in} + P_{Cl} [Cl^-]_{out}} \quad (1-4)$$

where P is the permeability of individual ion species.

¹ Reduction method of linear circuit networks consisting of voltage and current sources and resistors with two terminals to an equivalent circuit consisting of a single voltage source and resistor in series (Thévenin 1883).

In the equivalent circuit model of passive membrane, the input resistance (R_N) is identical to the sum of all individual membrane resistances (i.e. $G_{K,Leak} + G_{Na,Leak} + G_{Cl,Leak}$). The system time constant (τ_m) is determined by multiplying R_N with C_m . Thus the subthreshold dynamics of V_m is governed by a single exponential function with τ_m in the equivalent circuit.

1.4.2 Active properties: Action potential

One of the most important models for the action potential is the Hodgkin & Huxley (1952) (H-H) formulation (Eq. 1-5). They successfully reproduced action potentials of the squid giant axon based on the equivalent circuit modeling (Eq. 1-2), pharmacologically identifying types and densities of time- and voltage-gated ion currents (i.e. fast Na^+ for generating action potentials and delayed rectified K^+ with leak channels for recovering membrane resting potential) and then mathematically describing their kinetics with gating variables (i.e. m and h for activation and inactivation of Na^+ currents, and n for activation of K^+ currents). It should be noted that the equations governing kinetics of active ion channels in Eq. 1-5 were empirically determined to match the experimental data.

$$C_m \dot{V}_m = -G_{Na} m^3 h (V_m - E_{Na}) - G_K n^4 (V_m - E_K) - G_{Leak} (V_m - E_{Leak}) + I_{app} \quad (1-5)$$

$$\dot{m} = \frac{m_\infty(V_m) - m}{\tau_m(V_m)}, \dot{h} = \frac{h_\infty(V_m) - h}{\tau_h(V_m)}, \dot{n} = \frac{n_\infty(V_m) - n}{\tau_n(V_m)}$$

where G_{Na} , G_K and G_{Leak} are maximum conductance densities for Na^+ , K^+ and leak ionic currents respectively. E_{Na} , E_K and E_{Leak} are equilibrium potentials Na^+ , K^+ and leak ionic currents respectively. τ_m , τ_h and τ_n are time constants representing the rates at which m , h and n approach their steady-state values of m_∞ , h_∞ and n_∞ respectively. I_{app} is the current intensity applied to the axon.

The additional features of H-H type of membrane excitability were further analyzed by FitzHugh (1961), expanding the van der Pol oscillator model² to lower the four-dimensional H-H equations (called FitzHugh-Nagumo model) into two-dimensional system (Eq. 1-6). The simplicity of his abstract model allowed the useful mathematical analysis of the H-H membrane excitability using phase-plane methods (refer to Fig. 1-3). It turned out that there was no explicit voltage threshold for action potential in H-H model, showing the absence of all or none spikes. In addition, the action potential could be initiated by even hyperpolarizing current pulse (called anodal break excitation). Thereafter the phase-plane analysis has been extensively used to characterize the model excitability.

$$\begin{aligned}\dot{V} &= V - \frac{V^3}{3} - w + I_{app} \\ \dot{w} &= 0.08(V + 0.7 - 0.8w)\end{aligned}\tag{1-6}$$

where w is the recovery variable similar to the gating variable, n , in H-H model (Eq. 1-5).

Morris-Lecar model (1981) has been one of the popular excitable membrane models in computational neuroscience because it is based on only two types of active conductances (Ca^{2+} for inward and K^+ for outward currents in Eq. 1-7) with Ohmic leak channels and two-dimensional so that the model excitability could be fully analyzed and readily manipulated using phase-plane methods. The main assumption in using this model is that the real higher-order system can be mapped onto a two-dimensional phase space without altering the topological properties of the phase profile. This assumption has been suggested to be true for the four-dimensional H-H system, showing that all excitation phenomena can be

² The concept of limit cycle occurred in nonlinear dynamical systems was originally introduced by the physicist Balthasar van der Pol (van der Pol and van der Mark, 1927). He demonstrated stable oscillations (i.e. limit cycle) in the electrical circuits governed by the second-order differential equation,

$$\ddot{x} - \varepsilon(1 - x^2)\dot{x} + x = 0$$

duplicated with minimal number of active currents in the two-dimensional Morris-Lecar model.

$$\begin{aligned}
 C_m \dot{V}_m &= -G_{Ca} m_\infty(V_m)(V_m - E_{Ca}) - G_K w(V_m - E_K) - G_{Leak}(V_m - E_{Leak}) + I_{app} \\
 \dot{w} &= \frac{w_\infty(V_m) - w}{\tau_n(V_m)}
 \end{aligned} \tag{1-7}$$

where G_{Ca} is the maximum conductance density for Ca^{2+} ion current.

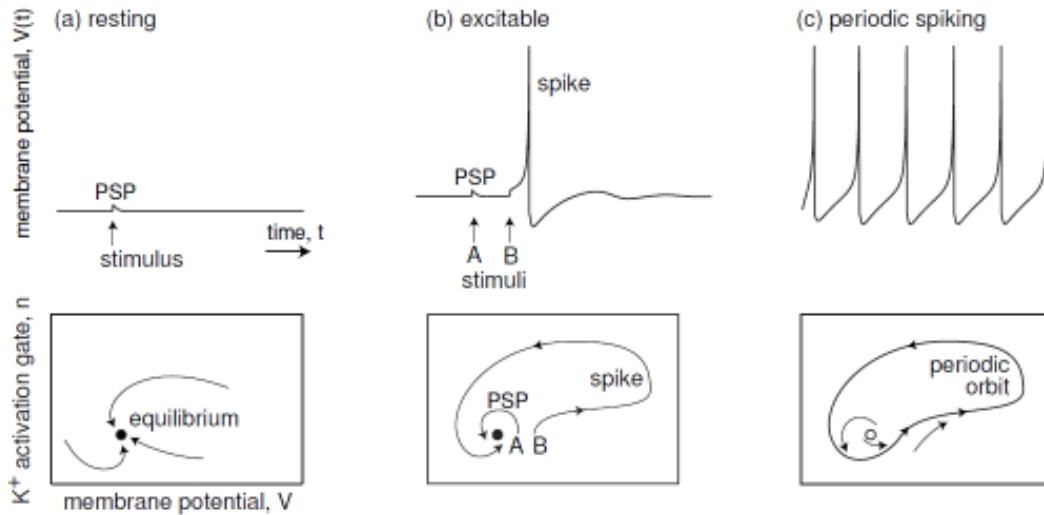


Figure 1-3. Graphical representation of membrane potential (V) response over time (t) (top) onto the phase plane consisting of V & recovery variable (n) (bottom). Resting membrane potential corresponds to filled (attractive) or blank (repelling) circles in the phase plane. The response of membrane potential (V) to the current stimulation is represented by a curve (or solution trajectory) with directional arrows. (a) Subthreshold membrane potential response: all solution trajectories starting with different default values of V come back to stable resting state. (b) Action potential: a large solution trajectory corresponds to a single spike. (c) Sustained firing activity: all solution trajectories are attracted into one periodic orbit curve. Note the qualitative change in the stability of equilibrium point and resulting periodic spiking behaviour, indicating the occurrence of bifurcation. All figures were adopted from (Izhikevich, 2007).

1.4.3 Active properties: Spike train

Hodgkin (1948) identified three phenomenologically different classes of firing responses to current pulses with various amplitudes in the squid axon (i.e. frequency (F)-current (I) relationship). In the first class (i.e. Class I) of the F-I relation, the firing frequency were initially low and gradually increased with increasing strength of the applied current. In the second class (i.e. Class II), the firing frequency was initially jumped to and sustained in a certain frequency band that is relatively insensitive to variations of the applied current intensity. In the third class (i.e. Class III), only a single action potential was evoked in response to a pulse of current. Sustained spiking activity could be observed only for extremely strong current intensity or not at all.

Given the fact that there are limited types of ion channels in the squid axon, it has been pointed out that the different classes of spiking responses may be generated due to the difference in the bifurcation³ mechanisms (refer to Fig. 1-4) underlying the cellular excitability, instead of the variety of ion channels (Rinzel and Ermentrout, 1989). Thereafter the possible bifurcation mechanisms have been extensively investigated using the nonlinear dynamical systems theory (Izhikevich, 2007), to describe and understand the mechanisms underlying fluctuation phenomenon (e.g. firing) observed in various membrane systems: axons (Fitzhugh, 1961), muscle fibers (Morris and Lecar, 1981), neurons (Izhikevich, 2007) and endocrine cells (Sherman et al., 1988).

From the dynamical systems point of view (Strogatz, 2000), the neuron can be considered as a highly nonlinear dynamical system (Glass, 2001). Unlike the linear systems, the neurons with the ability to generate action potentials (top panels in Fig. 1-3) typically have following characteristics in the phase plane (bottom panels in Fig. 1-3): 1) multiple equilibrium points (indicated by circles)

³ The bifurcation indicates the sudden transition of output behaviour of dynamical systems to the qualitatively different state as system parameters of interest (called bifurcation parameters) change.

representing resting states that can be either stable (filled circle) or unstable (blank circle), 2) qualitative transition in system dynamics (called bifurcation) by changes in numbers of equilibria or their stability while varying parameters, 3) periodic oscillations (called limit-cycle or periodic orbit) and 4) deterministic but unpredictable dynamics (called chaos).

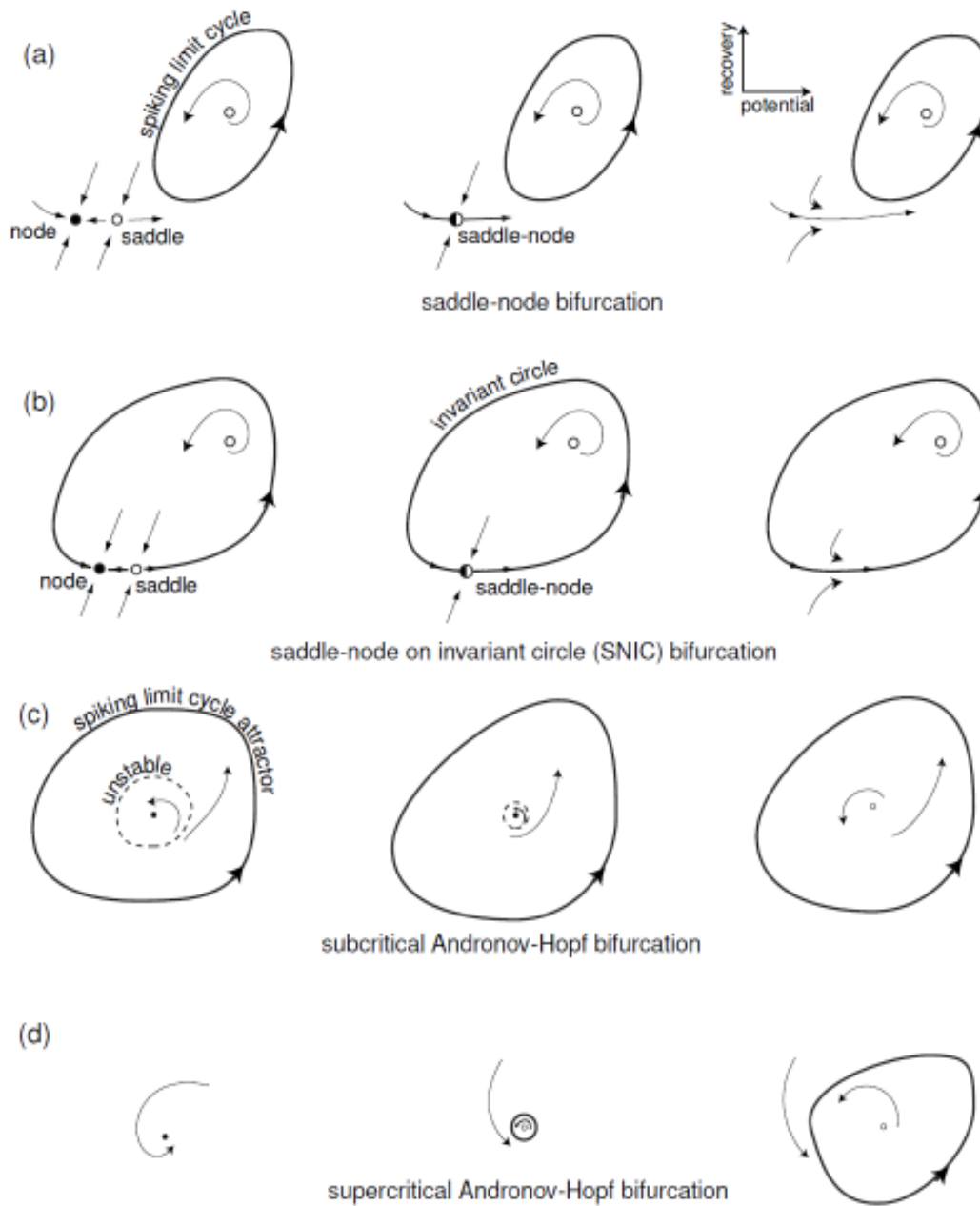


Figure 1-4. Four bifurcation mechanisms underlying the transition from the resting to sustained spiking activity as the intensity of the injected current increases. (a) Saddle-node bifurcation. At rest, there are two stable states: resting state and spiking limit cycle. The transition to the sustained spiking state occurs through the coalescence and annihilation of two equilibrium points (marked by node and saddle). (b) Saddle-node on invariant circle bifurcation. At rest, there is only one stable state: resting state (node). Similar to the saddle-node bifurcation,

the transition to the sustained spiking state occurs through the coalescence and annihilation of two equilibrium points (marked by node and saddle) except the existence of invariant circle at the bifurcation moment. (c). Subcritical Andronof-Hopf bifurcation. At rest, there are two stable states: resting state (node) and a large spiking limit cycle. The transition to the sustained spiking state occurs through the loss of the stability in the stable equilibrium point with shrinking unstable limit cycle. (d). Supercritical Andronof-Hopf bifurcation. At rest, there is only one stable state (node): resting state. A small stable limit cycle is generated followed by the loss of stability in the stable equilibrium point. The amplitude of the limit cycle increases to a full-size spiking limit cycle with increasing current intensity. All figures were adopted from (Izhikevich, 2007).

The neurons have been thought to be highly excitable since they typically rest near the transition point to generate spikes. Thus, the transition feature (i.e. bifurcation mechanism) from the resting state (i.e. stable equilibrium point) to the sustained spiking activity (i.e. limit-cycle) has been reported to be a critical factor to determine firing responses to the current stimulation (Prescott et al., 2008). In general, only four bifurcation mechanisms shown in Fig. 1-4 are sufficient to describe many different electrophysiological mechanisms of neuronal excitability (Izhikevich, 2007): Saddle-node, Saddle-node on invariant circle bifurcation, Subcritical Andronov-Hopf, and Supercritical Andronov-Hopf bifurcation. The Hodgkin's classification of F-I relations have been fully explained using different bifurcation mechanisms. The Class I excitability occurs via the saddle-node bifurcation on an invariant circle (Fig. 1-4 (b)), whereas the other three bifurcations (Fig. 1-4 (a), (c) and (d)) result in the Class II excitability. The experimental study on the third class of excitability has been neglected at least partially due to the assumption that a single spiking neuron might be unhealthy. However, Prescott and his colleagues have shown that the third class of excitability could be generated in healthy spinal sensory neurons and explained by the distinct dynamical mechanism of initiating spikes (called separatrix-crossing). They have also demonstrated that the two-dimensional Morris-Lecar like models could generate all types of firing responses (i.e. Class I, II and III) by varying the coefficient value to control the steady-state activation curve (i.e. w_∞ in Eq. 1-7) of the slow outward current. This study has indicated that the details of transmembrane currents might not be necessarily needed to set up, by matching the bifurcation mechanism for the initiation of spiking between the target and model neuron.

1.4.4 Passive properties: Functional significance of branching dendrites

If a single neuron with the dendritic trees were assumed to be something like a sphere with a uniform distribution of membrane potential, it would be possible to fully characterize neuronal dynamics based on the equivalent circuit modeling framework. However this isopotential neuron model turned out to mislead experimentalists in interpreting the measurement of the membrane time constant, since the time course of subthreshold membrane potential in the dendritic neuron model follows the error function⁴ that is quite different from a single exponential function that has been estimated in the isopotential neuron model (Rall, 1957). The roles of the dendrites attached to the soma in the electrical properties of neurons began to get attention late 1950s by Rall's series of theoretical papers.

Core conductor theory: The first neuron model considering the passive dendrites was suggested by Wilfrid Rall, based on the resemblance of the cylinder-like dendritic branches to an electrical cable or core conductor whose property was first analyzed by Lord Kelvin in 1855. Applying Ohm's law to a cylinder of infinite length with uniform passive nerve membrane, the spatio-temporal distribution of membrane potential is governed by a partial differential equation expression known as the cable equation,

$$\lambda^2 \frac{\partial^2 V}{\partial x^2} = \tau \frac{\partial V}{\partial t} + V \quad (1-8)$$

where V is the deviation from the resting membrane potential, $\lambda = \sqrt{(R_m \cdot d)/(R_i \cdot 4)}$ is the space constant, $\tau = C_m \cdot R_m$ is the time constant, R_m is the specific membrane resistivity [$\Omega \cdot \text{cm}^2$], R_i is the cytoplasmic or core resistivity [$\Omega \cdot \text{cm}$], d is the cable diameter [cm], C_m is the specific membrane capacitance [F/cm^2], x and t are the physical distance [cm] and time [ms].

⁴ In the error function, the membrane potential changes more rapidly in the early state than in the exponential function. Thus applying the traditional time constant defined in the exponential function makes significant error in obtaining the membrane time constant of neurons with the dendrites.

Based on the core conductor theory, Rall established several key concepts on the signal propagation of the dendrites particularly utilizing λ that was derived from the infinite cable model with steady-state condition. λ is the physical distance from the site of current injection at which the membrane potential at the current injection site decays to 37 % of the initial value. Functionally λ indicates the ability of the dendrites to transfer the steady membrane potential i.e. the larger λ the less membrane potential attenuation when propagating along the path of the dendrites. The electrotonic structure of the branching dendritic trees in the cable modeling approach was represented by one system parameter of the electrotonic length (L) that is the cable length (l) relative to its space constant (λ). The longer L indicates the more signal attenuation at the other end of the cable.

One of Rall's important contributions was to develop the theoretical framework to deal with the complex dendritic trees. He showed that the dendrites may be collapsed into a single cable model with some appropriate assumptions: spatial uniformity of membrane properties, voltage independent R_m , the 3/2 power rule for branch points, and all dendrites terminating with the same electrotonic length (L). The Rall model (i.e. finite length cable with a somatic compartment) has been applied to the quantitative investigation of how local synaptic effects (i.e. excitatory or inhibitory postsynaptic potential at synaptic site) are distorted when transmitted to the soma from the synaptic sites over the passive dendrites. The synaptic inputs to the terminal of the dendrites turned out to make a significant contribution to depolarizing the membrane for the initiation of an action potential at the soma, which strongly implies that the influence of dendrites should be considered in investigating electrical properties of neurons. However, it should be realized that the extent of dendrites in terms of space constant (i.e. electrotonic distance, $X=x/\lambda$ where x is the physical distance from the origin of the cable) in the cable modeling framework is an electrical parameter which does not provide any information about how many millimeters the dendrites actually reach from the soma. It should be also noted that a synaptic input to the single point over the

cable model corresponds to the synaptic inputs to all points over the dendrites that are equally away from the soma by the same electrotonic distance (X).

The analysis of the neuron model with ideally branching dendrites have shown more details of signal propagation properties (Rall and Rinzel, 1973; Rinzel and Rall, 1974). The degree of the signal attenuation over the dendrites was different according to the propagation direction, which has been called direction-dependant voltage attenuation (DDVA) phenomenon. For example, the membrane potential (or voltage) attenuates more severely when transmitted centrally into the soma than peripherally out to the dendrites.

Two-port theory: The Rall's cable model of the complex dendrites requires assumptions among which the termination of all dendrites at the same L , invariable diameter of individual branches and $3/2$ power rule at all branching points are particularly restrictive assumptions that are likely to be true only for a few types of neurons. For the same purpose for analyzing dendritic signaling of synaptic inputs, an alternative approach (Fig 1-5) was suggested based on two-port theory⁵ in the early 1980s (Carnevale and Johnston, 1982). Analyzing the two-port network representing single dendritic neurons, the DDVA property was generalized in the more simplified form of equations compared to the cable model. Two more signal propagation properties between the soma and dendrites were identified: 1) the current attenuation (e.g. I_2/I_1 only with I_1) was identical to the voltage attenuation (e.g. V_1/V_2 only with I_2) in the opposite direction of current propagation and 2) the transfer resistance⁶ (i.e. V_2/I_1 only with I_1 and V_1/I_2 only with I_2) was same for both directions between the soma and dendrites. Another interesting property induced from the two-port theory is that the logarithm of voltage attenuation (V_2/V_1 with I_1 or V_1/V_2 with I_2) corresponds to the

⁵ Any passive electric circuit with two pairs of terminals (or ports) can be transformed into a simple two-port network consisting of three characteristic parameters, simplifying analysis.

⁶ The transfer resistance in the two-port network is defined as the ratio of the voltage evoked at one port to the current intensity injected at the other port.

electrotonic distance (X) in an infinite cable model (Zador et al., 1995). This property further allowed to transform the morphology of the passive dendrites into electrotonic domain (Carnevale and Johnston, 1982; Carnevale et al., 1995; Carnevale et al., 1997). The resulting morphoelectrotonic structure of the dendrites turned out to be significantly varied according to the input signal type (i.e. DC or AC) and propagation directions (i.e. soma-to-dendrite or vice versa). In particular, the two-port theory allowed us to develop the novel reduced modeling framework without any restrictive assumptions to handle with the branching dendritic trees while retaining essential dendritic signaling properties that have been identified.

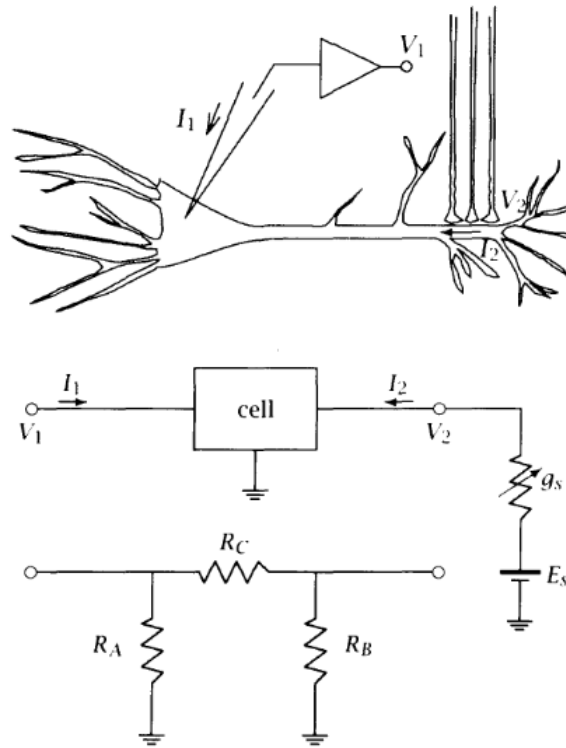


Figure 1-5. Schematic reduction of a neuron with synaptic inputs into a two-port network. In the typical recording situation (top figure) where one electrode is placed at the soma to measure the synaptic effects originated from the dendrites, the soma and synaptic sites can be considered as electrical ports. Applying two-port theory, the cell (middle figure) between two ports can be represented by a three-resistor network (bottom figure) without any assumptions except for the passive dendrites. All figures were adopted from Canavale and Johnston 1982.

1.4.5 *Active properties: Bistable firing behaviour*

The bifurcation mechanisms underlying the MN bistability became more complex when considering the interaction between spiking behaviour at the soma and plateau potentials at the dendrites. Booth and Rinzel (1995) have fully characterized the dynamics of MNs with the bistable dendrites using bifurcation analysis of a conductance based two-compartment model⁷ (refer to Fig. 1-6), where Morris-Lecar membrane excitability was used to produce sustained spiking behaviour (i.e. Class II excitability) via Hopf bifurcation at the soma-like compartment and plateau potentials via saddle-node bifurcation at the dendrite-like compartment. Varying the electrical conductance coupling two compartments, they demonstrated the systematic changes in the bifurcation structure describing the bistable firing patterns of the reduced model. However the manipulation of a single coupling conductance might not be sufficient to represent the physiological signal propagation properties (i.e. signal direction and type dependent voltage attenuations) of the complex dendritic systems. The bifurcation analysis was conducted for the new reduced neuron model developed in this thesis to investigate whether the bifurcation mechanisms for generating the MN bistability were conserved as the dendritic signaling properties changes.

1.5 COMPUTATIONAL MODELS FOR MOTOR NEURONS

Various types of modeling approaches shown in Fig. 1-6 have been used to investigate firing behaviour of neurons. The one-compartment modeling is one of the simplest approaches, which is comparable with electrical circuit model (i.e. Eq. 1-2) equivalent to the biological membrane patch. Electrically coupling the additional compartment representing the dendrites to the one-compartment model, the two-compartment modeling has been employed to particularly show the

⁷ The two-compartment model consists of two soma- and dendrite-like compartments coupled by electrical conductance. Dynamics of each homogeneous compartment can be formulated using equivalent circuit of biological membrane patch.

general roles of complex dendritic systems. Because of the simplifying assumption in the two-compartment model that all dendritic branches are collapsed into one homogeneous compartment, the multi-compartment models retaining only key morphological properties of the dendrites and axon have been used in considering the spatial distribution of active membrane properties or synaptic inputs. In all reduced neuron models reflecting the dendritic influence, the electrical coupling between the soma and dendrites has been represented by mathematical parameters or electrotonic distance. To improve the link between the neuron model and real neuron, the anatomically-reconstructed compartmental models have been used mainly for the studies where the individual dendritic branches are of particular interest.

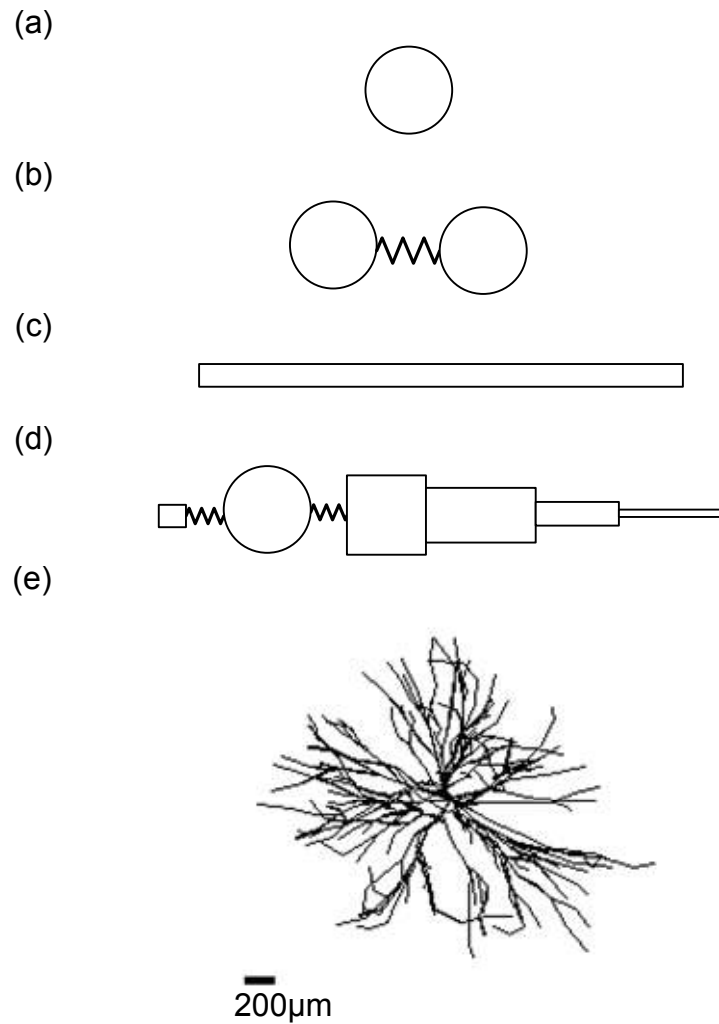


Figure 1-6. Computational neuron modeling frameworks. (a). One-compartment model (Baldissera and Gustafsson, 1974; Matthews, 1996; Powers, 1993; Prinz et al., 2003). (b). Two-compartment model (Booth and Rinzel, 1995; Booth et al., 1997; Mainen and Sejnowski, 1996; Pinsky and Rinzel, 1994). (c). Continuous cable model (Gutman, 1991). (d). Multi-compartment model (Dai et al., 1998; Dodge and Cooley, 1973; Jones and Bawa, 1997; Traub, 1977). (e). Anatomically reconstructed model (Carlin et al., 2000b; Elbasiouny et al., 2005; Grande et al., 2007).

For mammalian MNs, combining Rall's dendrites modeling with Hodgkin-Huxley excitability, action potentials have been quantitatively investigated considering both the geometry and distribution of voltage-gated ion channel densities in the dendritic, somatic and axonal regions (Dodge and Cooley, 1973; Traub, 1977). However, these MN models have not reflected any active membrane mechanisms (i.e. PIC channels) in the dendrites that are responsible for generating bistable firing behaviour of the MNs in vivo. After the experimental identification of the PICs, several types of modeling approaches have been developed to investigate the associated bistable firing behaviour of the MNs. The ideal cable model was the first bistable MN model that have used to emphasize the dendritic localization of the active current sources that give rise to the hysteretic current-voltage relationship measured at the soma (Gutman, 1991). The one-compartment modeling approach has been suggested showing that the bistable firing behaviour of MNs might also be induced only by the combinations of different types of active membrane conductances (Powers, 1993). For the systematic analysis of the influence of spatially distributed PIC channels, two-compartment modeling framework have been suggested in which the bifurcation mechanisms underlying the bistable firing behaviour were identified and furthermore the overall variations of firing output behaviour were first demonstrated while varying the electric coupling relation between the soma and PIC channels over the dendrites (Booth and Rinzel, 1995). Although Booth and Rinzel model has been accepted as a minimal model to generate bistable firing patterns, the signal propagations between the soma and dendrites including PIC channels were manipulated by varying the abstract model parameters which can not give any physical distance information. The physical distribution of PIC channels for the bistable firing behaviour of MNs have been studied particularly using anatomically reconstructed models of cat spinal motor neurons (Bui et al., 2006; Carlin et al., 2000b; Elbasiouny et al., 2005). In their studies, however, the distribution of PIC channels was investigated over only a few types of dendritic geometry which does not seem to be sufficient to extract the general insights into the influence of complex dendritic systems.

Modeling approaches that use anatomically reconstructed dendrites implicitly include physiological dendritic signaling properties. However, to determine the implications of dendritic signaling properties (i.e. signal direction and type dependent propagations) for bistability and establish mathematical generalizations using analysis, the dendritic signaling parameters must be amenable to the explicit manipulation that is typical of reduced modeling approaches. Two-compartment modeling approaches have discovered many fundamental insights about the dynamical behaviour of neurons and the influence of coupling parameters between the soma and dendrites. These models however, did not explicitly derive their coupling parameters from the anatomy and biophysical properties of reconstructed dendrites, instead choosing specific mathematical parameters from their system equations that could best represent physiological coupling properties.

Probably due to the lack of a suitable theoretical framework to deal with the complex geometry of the dendrites along with the cable properties (Cullheim et al., 1987a; Cullheim et al., 1987b; Donohue and Ascoli, 2008), little has been known how the physiological signal propagation properties of the dendrites impact the generation of bistable firing patterns in MNs.

1.6 THESIS OUTLINES

In order to derive general principles describing the roles of dendrites in the MN bistability, the biophysically realistic, physiologically plausible reduced modeling framework is developed that satisfies the following three system requirements:

- 1) The dendritic signaling properties should be parameterized within the modeling framework as a function of the physical distance. In other words, the model parameter values must analytically be determined to retain all electric properties of the MNs that are essential to produce the physiological bistable firing behaviour.

- 2) The reduction procedure should not include any restrictive assumptions to handle with the complex morphology of the dendrites.
- 3) The dimension of the system equations should be low enough not only to apply theoretical analysis (i.e. dynamical systems theory) for the mechanistic investigation of model behaviour, but also to be used as a ‘building-block’ for the population simulation of the MN pool.

Anatomically reconstructed models are typically hard to satisfy the first and second requirement due to too many geometric parameters representing the complex dendritic trees, whereas the reduced modeling such as cable and two-compartment modeling has not explicitly considered the physiological signal propagation properties of the dendrites. Developing the new reduced modeling framework satisfying above three requirements, I identify the essential biophysical properties for the nonlinear dynamics of the MNs and show how those properties affect the bistability of a single MN.

1.6.1 Chapter 2: Formulation of a new reduced model for single MNs

The goal of this chapter is to derive a reduced model that matches steady-state DC signal propagation of the complex dendritic systems. I begin with characterizing asymmetric coupling between the dendrites and soma measuring the voltage attenuation properties in six anatomically reconstructed and type-identified cat spinal motor neurons. This characterization shows that the voltage attenuation at any distance from the soma depends on the propagation direction of input signal (called direction-dependent voltage attenuation, DDVA) and may be described as a function of the input resistance at the soma. The first analytical solution for the lumped cable parameters in a two-compartment model is derived based on this finding.

1.6.2 Chapter 3: Roles of asymmetric dendritic signaling in the bistability of MN models

This chapter is dedicated to verify that the explicit representation of DDVA in two-compartment model is beneficial to capture dynamical properties of a single MN. Using the new two-compartment modeling framework (Chapter 2), the passive input-output relationship of the asymmetrically coupled model with DDVA is analytically compared to the symmetrically coupled case without DDVA. Predictions based on the analytic comparison were tested using numerical simulations. The simulations evaluate the nonlinear dynamics of the models as a function of coupling parameters. It is proposed that the physiological property of asymmetric coupling plays an important role in generating and stabilizing the bistability of motor neurons by interacting with the excitability of dendritic branches.

1.6.3 Chapter 4: Influence of back-propagating APs on model bistability

In this chapter, I investigate how the propagation of alternating signals (i.e. AC), like action potentials, into the dendrites influence bistable firing behaviour of a two-compartment model. The frequency response of the passive dendrites is first characterized along the path of dendritic trees in anatomically reconstructed type-identified motor neuron models. Then the previous reduced modeling approach is expanded to retain the AC signal propagation property of the dendrites in the anatomical models. The nonlinear dynamics of the expanded reduced model are numerically evaluated while varying the degree of the AC signal attenuation. The simulations show a positive correlation between AC signal attenuation and dendritic excitability indicated by changes in current threshold for activation of the plateau potential. This result suggests that the attenuation of back-propagating action potentials, determined by the geometry of the dendrites along with the cable properties, might be crucial to determine the bistable firing behaviour of motor neurons in vivo.

1.6.4 Chapter 5

In this chapter, the modeling procedure for a single neuron with the dendrites is summarized and results from the mathematical analysis and computer simulations are discussed. The future works for modeling the MN population are also presented based on our findings.

1.7 BIBLIOGRAPHY FOR CHAPTER 1

Baldissera, F., and Gustafsson, B. (1974). Firing behaviour of a neurone model based on the afterhyperpolarization conductance time course. First interval firing. *Acta Physiol Scand* *91*, 528-544.

Baldissera, F., Gustafsson, B., and Parmiggiani, F. (1978). Saturating summation of the afterhyperpolarization conductance in spinal motoneurons: a mechanism for 'secondary range' repetitive firing. *Brain Res* *146*, 69-82.

Ballou, E. W., Smith, W. B., Anelli, R., and Heckman, C. J. (2006). Measuring dendritic distribution of membrane proteins. *J Neurosci Methods* *156*, 257-266.

Bennett, D. J., Hultborn, H., Fedirchuk, B., and Gorassini, M. (1998). Synaptic activation of plateaus in hindlimb motoneurons of decerebrate cats. *J Neurophysiol* *80*, 2023-2037.

Bennett, D. J., Li, Y., and Siu, M. (2001). Plateau potentials in sacrocaudal motoneurons of chronic spinal rats, recorded in vitro. *J Neurophysiol* *86*, 1955-1971.

Booth, V., and Rinzel, J. (1995). A minimal, compartmental model for a dendritic origin of bistability of motoneuron firing patterns. *J Comput Neurosci* *2*, 299-312.

Booth, V., Rinzel, J., and Kiehn, O. (1997). Compartmental model of vertebrate motoneurons for Ca²⁺-dependent spiking and plateau potentials under pharmacological treatment. *J Neurophysiol* *78*, 3371-3385.

- Brock, L. G., Coombs, J. S., and Eccles, J. C. (1952). The recording of potentials from motoneurons with an intracellular electrode. *J Physiol* 117, 431-460.
- Bui, T. V., Ter-Mikaelian, M., Bedrossian, D., and Rose, P. K. (2006). Computational estimation of the distribution of L-type Ca(2+) channels in motoneurons based on variable threshold of activation of persistent inward currents. *J Neurophysiol* 95, 225-241.
- Burke, R. E., Levine, D. N., Tsairis, P., and Zajac, F. E., 3rd (1973). Physiological types and histochemical profiles in motor units of the cat gastrocnemius. *J Physiol* 234, 723-748.
- Carlin, K. P., Jiang, Z., and Brownstone, R. M. (2000a). Characterization of calcium currents in functionally mature mouse spinal motoneurons. *Eur J Neurosci* 12, 1624-1634.
- Carlin, K. P., Jones, K. E., Jiang, Z., Jordan, L. M., and Brownstone, R. M. (2000b). Dendritic L-type calcium currents in mouse spinal motoneurons: implications for bistability. *Eur J Neurosci* 12, 1635-1646.
- Carnevale, N. T., and Johnston, D. (1982). Electrophysiological characterization of remote chemical synapses. *J Neurophysiol* 47, 606-621.
- Carnevale, N. T., Tsai, K. Y., Claiborne, B. J., and Brown, T. H. (1995). The electronic transformation: a tool for relating neuronal form and function. *Advances in Neural Information Processing* 7, 69 - 76.
- Carnevale, N. T., Tsai, K. Y., Claiborne, B. J., and Brown, T. H. (1997). Comparative electrotonic analysis of three classes of rat hippocampal neurons. *J Neurophysiol* 78, 703-720.
- Cullheim, S., Fleshman, J. W., Glenn, L. L., and Burke, R. E. (1987a). Membrane area and dendritic structure in type-identified triceps surae alpha motoneurons. *J Comp Neurol* 255, 68-81.

Cullheim, S., Fleshman, J. W., Glenn, L. L., and Burke, R. E. (1987b). Three-dimensional architecture of dendritic trees in type-identified alpha-motoneurons. *J Comp Neurol* 255, 82-96.

Dai, Y., Jones, K. E., Fedirchuk, B., Krawitz, S., and Jordan, L. M. (1998). Modeling the lowering of motoneuron voltage threshold during fictive locomotion. *Ann N Y Acad Sci* 860, 492-495.

Destexhe, A., and Pare, D. (1999). Impact of network activity on the integrative properties of neocortical pyramidal neurons in vivo. *J Neurophysiol* 81, 1531-1547.

Dodge, F., and Cooley, J. (1973). Action potential of the motor neuron. *IBM J Res Dev* 17, 219-229.

Donohue, D. E., and Ascoli, G. A. (2008). A comparative computer simulation of dendritic morphology. *PLoS Comput Biol* 4, e1000089.

Eccles, J. C., Eccles, R. M., and Lundberg, A. (1957). The convergence of monosynaptic excitatory afferents on to many different species of alpha motoneurons. *J Physiol* 137, 22-50.

Elbasiouny, S. M., Bennett, D. J., and Mushahwar, V. K. (2005). Simulation of dendritic CaV1.3 channels in cat lumbar motoneurons: spatial distribution. *J Neurophysiol* 94, 3961-3974.

Fitzhugh, R. (1961). Impulses and Physiological States in Theoretical Models of Nerve Membrane. *Biophys J* 1, 445-466.

Fuglevand, A. J., Winter, D. A., and Patla, A. E. (1993). Models of recruitment and rate coding organization in motor-unit pools. *J Neurophysiol* 70, 2470-2488.

Glass, L. (2001). Synchronization and rhythmic processes in physiology. *Nature* 410, 277-284.

- Grande, G., Bui, T. V., and Rose, P. K. (2007). Estimates of the location of L-type Ca²⁺ channels in motoneurons of different size: a computational study. *J Neurophysiol* 97, 4023-4035.
- Granit, R., Kernell, D., and Shortess, G. K. (1963). The Behaviour of Mammalian Motoneurons During Long-Lasting Orthodromic, Antidromic and Trans-Membrane Stimulation. *J Physiol* 169, 743-754.
- Gutman, A. (1991). Bistability of dendrites. *Int J Neural Syst* 1, 291-304.
- Heckman, C. J., Lee, R. H., and Brownstone, R. M. (2003). Hyperexcitable dendrites in motoneurons and their neuromodulatory control during motor behavior. *Trends Neurosci* 26, 688-695.
- Hodgkin, A. L. (1948). The local electric changes associated with repetitive action in a non-medullated axon. *J Physiol* 107, 165-181.
- Hodgkin, A. L., and Huxley, A. F. (1952). A quantitative description of membrane current and its application to conduction and excitation in nerve. *J Physiol* 117, 500-544.
- Hooper, S. L. (2000). Central pattern generators. *Curr Biol* 10, R176.
- Hornby, T. G., McDonagh, J. C., Reinking, R. M., and Stuart, D. G. (2002). Motoneurons: A preferred firing range across vertebrate species? *Muscle Nerve* 25, 632-648.
- Hounsgaard, J., Hultborn, H., Jespersen, B., and Kiehn, O. (1984). Intrinsic membrane properties causing a bistable behaviour of alpha-motoneurons. *Exp Brain Res* 55, 391-394.
- Hounsgaard, J., and Mintz, I. (1988). Calcium conductance and firing properties of spinal motoneurons in the turtle. *J Physiol* 398, 591-603.

- Ito, M., and Oshima, T. (1965). Electrical behaviour of the motoneurone membrane during intracellularly applied current steps. *J Physiol* 180, 607-635.
- Izhikevich, E. M. (2007). *Dynamical systems in neuroscience : the geometry of excitability and bursting* (Cambridge, Mass.: MIT Press).
- Jones, K. E., and Bawa, P. (1997). Computer simulation of the responses of human motoneurons to composite 1A EPSPs: effects of background firing rate. *J Neurophysiol* 77, 405-420.
- Kernell, D. (1965a). High-frequency repetitive firing of cat lumbosacral motoneurons stimulated by long-lasting injected currents. *Acta Physiol Scand* 65, 74-86.
- Kernell, D. (1965b). Synaptic Influence on the Repetitive Activity Elicited in Cat Lumbosacral Motoneurons by Long-Lasting Injected Currents. *Acta Physiol Scand* 63, 409-410.
- Lee, R. H., and Heckman, C. J. (1998a). Bistability in spinal motoneurons in vivo: systematic variations in persistent inward currents. *J Neurophysiol* 80, 583-593.
- Lee, R. H., and Heckman, C. J. (1998b). Bistability in spinal motoneurons in vivo: systematic variations in rhythmic firing patterns. *J Neurophysiol* 80, 572-582.
- Lee, R. H., and Heckman, C. J. (2000). Adjustable amplification of synaptic input in the dendrites of spinal motoneurons in vivo. *J Neurosci* 20, 6734-6740.
- Li, Y., and Bennett, D. J. (2003). Persistent sodium and calcium currents cause plateau potentials in motoneurons of chronic spinal rats. *J Neurophysiol* 90, 857-869.
- Mainen, Z. F., and Sejnowski, T. J. (1996). Influence of dendritic structure on firing pattern in model neocortical neurons. *Nature* 382, 363-366.

- Manuel, M., Iglesias, C., Donnet, M., Leroy, F., Heckman, C. J., and Zytnicki, D. (2009). Fast kinetics, high-frequency oscillations, and subprimary firing range in adult mouse spinal motoneurons. *J Neurosci* 29, 11246-11256.
- Matthews, P. B. (1996). Relationship of firing intervals of human motor units to the trajectory of post-spike after-hyperpolarization and synaptic noise. *J Physiol* 492 (Pt 2), 597-628.
- Morris, C., and Lecar, H. (1981). Voltage oscillations in the barnacle giant muscle fiber. *Biophys J* 35, 193-213.
- Pinsky, P. F., and Rinzel, J. (1994). Intrinsic and network rhythmogenesis in a reduced Traub model for CA3 neurons. *J Comput Neurosci* 1, 39-60.
- Powers, R. K. (1993). A variable-threshold motoneuron model that incorporates time- and voltage-dependent potassium and calcium conductances. *J Neurophysiol* 70, 246-262.
- Prescott, S. A., De Koninck, Y., and Sejnowski, T. J. (2008). Biophysical basis for three distinct dynamical mechanisms of action potential initiation. *PLoS Comput Biol* 4, e1000198.
- Prinz, A. A., Billimoria, C. P., and Marder, E. (2003). Alternative to hand-tuning conductance-based models: construction and analysis of databases of model neurons. *J Neurophysiol* 90, 3998-4015.
- Rall, W. (1957). Membrane time constant of motoneurons. *Science* 126, 454.
- Rall, W., and Rinzel, J. (1973). Branch input resistance and steady attenuation for input to one branch of a dendritic neuron model. *Biophys J* 13, 648-687.
- Rall, W., Segev, I., Rinzel, J., and Shepherd, G. M. (1995). The theoretical foundation of dendritic function : selected papers of Wilfrid Rall with commentaries (Cambridge, Mass. ; London: MIT Press).

- Ramón y Cajal, S. (1933). *Histology, Rev. / edn* (Baltimore: W. Wood).
- Rinzel, J., and Ermentrout, B. (1989). *Analysis of neural excitability and oscillations. Methods in Neuronal Modeling*, Cambridge, Mass: MIT Press
- Rinzel, J., and Rall, W. (1974). Transient response in a dendritic neuron model for current injected at one branch. *Biophys J* 14, 759-790.
- Schwindt, P., and Crill, W. (1980a). Role of a persistent inward current in motoneuron bursting during spinal seizures. *J Neurophysiol* 43, 1296-1318.
- Schwindt, P., and Crill, W. E. (1977). A persistent negative resistance in cat lumbar motoneurons. *Brain Res* 120, 173-178.
- Schwindt, P. C. (1973). Membrane-potential trajectories underlying motoneuron rhythmic firing at high rates. *J Neurophysiol* 36, 434-439.
- Schwindt, P. C., and Crill, W. E. (1980b). Effects of barium on cat spinal motoneurons studied by voltage clamp. *J Neurophysiol* 44, 827-846.
- Schwindt, P. C., and Crill, W. E. (1980c). Properties of a persistent inward current in normal and TEA-injected motoneurons. *J Neurophysiol* 43, 1700-1724.
- Schwindt, P. C., and Crill, W. E. (1982). Factors influencing motoneuron rhythmic firing: results from a voltage-clamp study. *J Neurophysiol* 48, 875-890.
- Sejnowski, T. J., Koch, C., and Churchland, P. S. (1988). Computational neuroscience. *Science* 241, 1299-1306.
- Sherman, A., Rinzel, J., and Keizer, J. (1988). Emergence of organized bursting in clusters of pancreatic beta-cells by channel sharing. *Biophys J* 54, 411-425.
- Sherrington, C. S. S. (1906). *Integrative action of the nervous system* (New Haven: Yale U.P.).

- Strogatz, S. H. (2000). *Nonlinear dynamics and chaos : with applications to physics, biology, chemistry, and engineering*, 1st pbk. print. edn (Cambridge, MA: Westview Press).
- Stuart, G., Spruston, N., and Häusser, M. (1999). *Dendrites* (Oxford, New York: Oxford University Press).
- Svirskis, G., and Hounsgaard, J. (1997). Depolarization-induced facilitation of a plateau-generating current in ventral horn neurons in the turtle spinal cord. *J Neurophysiol* 78, 1740-1742.
- Traub, R. D. (1977). Motoneurons of different geometry and the size principle. *Biol Cybern* 25, 163-176.
- van der Pol, B and van der Mark, J (1927). Frequency demultiplication. *Nature* 120, 363-364.
- Zador, A. M., Agmon-Snir, H., and Segev, I. (1995). The morphoelectrotonic transform: a graphical approach to dendritic function. *J Neurosci* 15, 1669-1682.
- Zengel, J. E., Reid, S. A., Sypert, G. W., and Munson, J. B. (1985). Membrane electrical properties and prediction of motor-unit type of medial gastrocnemius motoneurons in the cat. *J Neurophysiol* 53, 1323-1344.

CHAPTER 2: Derivation of cable parameters for a reduced model that retains asymmetric voltage attenuation of reconstructed spinal motor neuron dendrites §

Abbreviations and symbols

| | |
|-------------------------------|-----------------------------------------------------------------------------------------------------------------------------------|
| R_N | input resistance at soma (M Ω) |
| $A_{SD}(D) = V_D/V_S$ | voltage attenuation factor from soma to dendrites at distance, D, from soma |
| $A_{DS}(D) = V_S/V_D$ | voltage attenuation factor from dendrites to soma at distance, D, from soma |
| η_{SD} | decay constant for voltage attenuation in the soma to dendrites direction (μm) |
| η_{DS} | decay constant for voltage attenuation in the dendrites to soma direction (μm) |
| $P(D) = SA_{soma}/SA_{total}$ | morphological factor for two-compartment model; the ratio of somatic surface area to total surface area at distance, D, from soma |
| $V_S = V_{m,S} - E_{leak}$ | deviation of somatic membrane potential from reversal potential of leak ion channel in soma of two-compartment models (mV) |

§ *A version of this chapter has been published.*

Kim H, Major LA and Jones KE, *J Comput Neurosci* 27: 321-336, 2009.

| | |
|----------------------------|----------------------------------------------------------------------------------------------------------------------------------------|
| $V_D = V_{m,D} - E_{leak}$ | deviation of dendritic membrane potential from reversal potential of leak ion channels in dendrite of two-compartment models (mV) |
| I_S | injected current density at soma in two-compartment models, normalized by somatic surface area ($\mu\text{A}/\text{cm}^2$) |
| I_D | injected current density at dendrite in two-compartment models, normalized by dendritic surface area ($\mu\text{A}/\text{cm}^2$) |
| $G_{C,S}$ | direction-dependent passive coupling conductance from soma to dendrite in explicit two-compartment model ($\mu\text{S}/\text{cm}^2$) |
| $G_{C,D}$ | direction-dependent passive coupling conductance from dendrite to soma in explicit two-compartment model ($\mu\text{S}/\text{cm}^2$) |
| G_m | uniform passive membrane conductance in explicit two-compartment model ($\mu\text{S}/\text{cm}^2$) |
| G_C | directionless passive coupling conductance in implicit two-compartment model ($\mu\text{S}/\text{cm}^2$) |
| $G_{m,S}$ | passive membrane conductance of soma in implicit two-compartment model ($\mu\text{S}/\text{cm}^2$) |
| $G_{m,D}$ | passive membrane conductance of dendrite in implicit two-compartment model ($\mu\text{S}/\text{cm}^2$) |
| C_m | uniform passive membrane capacitance for two-compartment models ($\mu\text{F}/\text{cm}^2$) |
| $\tau_0 = \tau_m$ | passive membrane time constant for all models (ms) |
| τ_l | equalizing time constant for all models (ms) |
| C_0, C_1 | coefficients used to form linearly independent combination of exponential decays (mV) |

| | |
|----------------------------------------------|---------------------------------------------------------------------------------------------------------------------------------------------|
| $r_{N,implicit}, r_{N,explicit}$ | input resistance at somatic part in implicit and explicit models respectively, normalized by somatic surface area ($M\Omega\text{-cm}^2$) |
| $A_{SD,implicit}^V(D), A_{SD,explicit}^V(D)$ | voltage attenuation factor for soma to dendrite direction at distance, D, from soma; used in implicit and explicit models |
| $A_{DS,implicit}^V(D), A_{DS,explicit}^V(D)$ | voltage attenuation factor for dendrite to soma direction at distance, D, from soma; used in implicit and explicit models |
| R_{eff} | effective membrane resistivity for calculating passive membrane time constant in two-compartment models ($M\Omega\text{-cm}^2$) |
| $A_{SD,implicit}^I(D), A_{SD,explicit}^I(D)$ | current attenuation factor for soma to dendrite direction at distance, D, from soma; used in implicit and explicit models |
| $A_{DS,implicit}^I(D), A_{DS,explicit}^I(D)$ | current attenuation factor for dendrite to soma direction at distance, D, from soma; used in implicit and explicit models |

2.1 INTRODUCTION

Motor neurons of the adult cat spinal cord were among the first central mammalian neurons to be studied with intracellular stimulating and recording electrodes (Coombs et al., 1955; Frank and Fuortes, 1955). Motor neurons were also the first to be analyzed by the rigorous mathematical and biophysical approach of Wilfrid Rall (Rall, 1957). Rall's analytical solutions of the passive cable equation and his development of the equivalent cylinder reduction of dendritic trees, demonstrated that significant biophysical insights could be learned using reduced models (Rall et al., 1995). In addition to the approximation of

dendritic geometry with reduced models, Rall together with Rinzel showed that the geometry of the dendrites had a significant impact on the electrotonic properties (Rall and Rinzel, 1973; Rinzel and Rall, 1974). Of particular relevance to this study, they showed that the voltage attenuation depended on the direction of propagation; there is a steep attenuation when potentials propagate centrally (from the dendrites to the soma) and a more gradual attenuation in the opposite direction. We will refer to this phenomenon as direction dependent voltage attenuation (DDVA).

Until the mid-1980s neurophysiologists were confident that motor neuron dendrites were passive. However, it is now known that in the presence of monoamines, motor neuron dendrites have persistent inward currents (PICs) that generate plateau potentials and amplify synaptic inputs (Carlin et al., 2000a; Heckmann et al., 2005; Hounsgaard et al., 1984; Lee and Heckman, 1996; Lee and Heckman, 1998a; Lee and Heckman, 1998b; Lee and Heckman, 1999a). One channel that contributes to the PICs is the CaV1.3, an L-type calcium channel (Carlin et al., 2000b). The full details of the location of these channels on the dendrites is unknown because there are no recordings from motor neuron dendrites and definitive immunohistochemical data is still being generated (Ballou et al., 2006). However, experimental data and mathematical modelling results agree on a number of important points: the PIC channels are not distributed uniformly over the dendrites, the PIC channels tend to occur in restricted regions with high density (i.e. clusters), and these clusters of PIC channels are physically separated from the soma by distances of at least 300 - 500 microns (Ballou et al., 2006; Heckman et al., 2003). The most recent modelling studies have used anatomically reconstructed motor neurons and varied the location of the PIC channels to reproduce electrophysiological data recorded from the soma (Bui et al., 2006; Carlin et al., 2000b; Elbasiouny et al., 2005; Grande et al., 2007). In these anatomically detailed models the DDVA phenomenon is implicit, a result of the geometry and passive properties of the reconstructed dendrites. One intriguing prediction from these studies is that the clusters of PIC

channels are located further from the soma in neurons with a large dendritic tree (Grande et al., 2007). Since the size of the dendritic tree is often interpreted as an indicator of motor neuron type, fast motor neurons with smaller input resistance relative to slow motor neurons tend to have larger dendritic trees, this prediction suggests that PIC channels will be located in a restricted region related to their motor neuron type. The combination of type-specific localization of PIC channels with the DDVA phenomena could have a significant impact on the nonlinear dynamical behaviour of motor neurons. However, to date there has been no explicit analysis of the effect of DDVA on nonlinear phenomena related to bistability in type-identified motor neurons.

One reason for the lack of analysis of DDVA on motor neuron input-output is that anatomically complex models preclude meaningful mathematical analysis. As elegantly shown by Rall, analysis requires using reduced models and assumptions in order to find closed form solutions. One popular reduction for single neuron models is the two-compartment model (Booth and Rinzel, 1995; Booth et al., 1997; Jones KE, 2000; Mainen and Sejnowski, 1996; Pinsky and Rinzel, 1994). The two-compartment approach is well suited to the case where ion channels for spiking are physically separated from ion channels that generate plateau potentials. A simplified two-compartment model could be used to explore the question: does DDVA in complex, biophysically realistic motor neuron models influence the nonlinear phenomena related to bistability? A prerequisite to resolving that question is the development of a method for directly deriving the lumped cable parameters for a reduced model from the geometrical and passive electrical properties of realistic motor neurons. This is the fundamental goal of the present manuscript. We first characterize the DDVA phenomena in anatomically reconstructed motor neuron models. Then determine if DDVA is related to the type of motor neuron (fast – slow). Finally, we develop two analytical methods for directly deriving the lumped cable parameters and demonstrate the superior results obtained with one of the methods. We show that an analytical solution

exists for the full range of passive membrane values of the heterogeneous cat spinal motor neuron pool.

2.2 METHODS

2.2.1 *Preparation of motor neuron anatomy*

The morphologies of six adult cat spinal cord α -motor neurons (MNs), contributed by Robert Burke's lab, were downloaded from <http://NeuroMorpho.Org> (Ascoli, 2006). Among the data formats available in NeuroMorpho.org, the standardized files (*.CNG.SWC) were selected. All six MNs were type-identified using mechanical criteria as FF, FR, or S (Burke et al., 1973) and have been the subject of extensive anatomical investigation (Cullheim et al., 1987a; Cullheim et al., 1987b). The anatomical data of the individual MNs were translated into the NEURON simulation environment v 5.9.9 (Carnevale and Hines, 2005) using the Import3D tool. The size of the soma was corrected after importing the anatomical data to correspond to the dimensions previously reported.

2.2.2 *Assignment of passive membrane properties*

The electrotonic properties for five of the six MNs were previously published and used in computer simulations (Fleshman et al., 1988; Segev et al., 1990). In these simulations, the cable parameters were determined by matching the response of computer models to intracellular voltage from the same cells during measurements of input resistance, time constant (τ_0) and electrotonic length (L_{peel}). The value of specific membrane resistivity (R_m) that matched the experimental measurements was determined assuming a cytoplasmic resistivity (R_a) of $70 \Omega \cdot \text{cm}$ and a specific membrane capacitance (C_m) of $1 \mu\text{F}/\text{cm}^2$. The values for R_m of the five models are given in Table 2-1 along with the names of the cells as they

appear in NeuroMorpho.org and in previous publications. The sixth MN downloaded from NeuroMorpho.org, V5, is an S-type soleus MN (M36/1 in (Cullheim et al., 1987a; Cullheim et al., 1987b)) that was not part of the electrotonic study (Fleshman et al., 1988).

Table 2-1. Passive membrane properties and electrotonic properties

| Cells | | R_m | | Electrotonic property | | | | |
|-------------------|------|-------|----------|-----------------------|------------|------------|-------------|-------------|
| Motor Neuron (MN) | Type | soma | dendrite | τ_0 | L_{peel} | R_N | η_{SD} | η_{DS} |
| V1 (36/4) | S | 455 | 15,500 | 10.4 (9.9) | 1.3 (1.3) | 1.9 (2.0) | 2680.6 | 224.2 |
| V2 (38/2) | FF | 66 | 17,000 | 6.9 (7.1) | 1.6 (1.6) | 0.7 (0.7) | 3059.5 | 144.7 |
| V3 (41/2) | FF | 70 | 20,000 | 7.0 (6.9) | 1.7 (1.6) | 0.8 (0.7) | 2758 | 119.5 |
| V4 (42/4) | FR | 120 | 17,000 | 7.7 (8.2) | 1.5 (1.6) | 0.97 (1.1) | 1941 | 143.9 |
| V6 (43/5) | FR | 225 | 11,000 | 7.1 (6.8) | 1.6 (1.7) | 1.25 (1.4) | 2145.8 | 190.8 |

Cell numbers in the first column matched with those in Fleshman et al, 1988; R_m , was non-uniform with lower value in the soma compared to dendrites; Simulated values (experimental estimate values) of electrotonic properties, τ_0 [ms], L_{peel} fitted at 10-15 ms, R_N [M Ω], η_{SD} and η_{DS} [μ m] of voltage decay constants measured for both directions in Fig. 2-1.

We assigned the same values for the specific cable parameters as previously reported and simulated the original electrophysiological experiments to estimate R_N , τ_0 , and L_{peel} . The last three columns of Table 2-1 give the values for our simulations and the original experimental values in parentheses. The discrepancies were within measurement error; therefore we considered our models to be valid electrotonic models of Burke's type-identified MNs.

Our initial simulations with the anatomically reconstructed models used non-uniform specific membrane resistivity that included a significantly smaller resistivity in the soma compared to the dendrites, i.e. a somatic shunt. The somatic shunt is an artifact resulting from the use of sharp electrodes (Holmes and Rall, 1992a; Major et al., 1993; Thurbon et al., 1998). To approximate the presumed non-impaired *in vivo* condition, in later simulations we used a uniform R_m chosen to give a desired value of input resistance.

2.2.3 *Generation of attenuation curves and voltage decay constant*

The steady-state voltage attenuation factor ($V_{measure}/V_{inject}$) in the passive models was calculated between the soma and all sites on the dendrites for current moving both toward (central) and away from (peripheral) the soma. The direction dependent voltage attenuation (DDVA) was calculated using the Impedance class tools in NEURON. This analysis is based on two-port reciprocal network theory (Carnevale and Johnston, 1982). First, the input impedances at the two locations of interest are determined (Z_{Ns} , soma and Z_{Nd} dendrite) and then the transfer impedance (Z_T) between the two locations is measured. The voltage attenuation factor in the central direction is

$$\frac{V_{soma}}{V_{dendrite}} = \frac{Z_T}{Z_{Nd}} \quad (2-1)$$

and in the peripheral direction is

$$\frac{V_{dendrite}}{V_{soma}} = \frac{Z_T}{Z_{Ns}} \quad (2-2)$$

The branching and geometry of dendrites generates large input impedance. This results in a central attenuation factor that is less than the peripheral attenuation factor, i.e. voltage attenuates more in the central direction.

The voltage attenuation was plotted as a function of distance from the soma. To quantify the rate of attenuation with distance, the data were fit to a single exponential function.

$$\frac{V_{measure}}{V_{inject}}(x) = e^{-x/\eta} \quad (2-3)$$

The voltage decay constant (η) was determined using a least square estimation algorithm in MATLAB. A double exponential fit was also tried but did not produce significantly better fits to the data. A decay constant was determined for both the dendrite-to-soma (η_{DS}) and the soma-to-dendrite directions (η_{SD}).

We compared the measured voltage attenuation to idealized cable models of the same cells (Fleshman et al., 1988; Jack et al., 1975; Rall, 1959). The analytical expression of the voltage attenuation factor derived from finite cable model with sealed end conditions was used (Carnevale and Johnston, 1982). The voltage attenuation in the central direction is,

$$\frac{V_{soma}}{V_{dendrite}} = \frac{1}{\cosh X + \frac{\tanh L \cdot \sinh X}{\rho}} \quad (2-4)$$

and in the peripheral direction is

$$\frac{V_{dendrite}}{V_{soma}} = \frac{\cosh(L - X)}{\cosh L} \quad (2-5)$$

Where X is the electrotonic distance ($X=x/\lambda$, x is a physical distance from the soma and λ is space constant), L is the electrotonic length, and ρ is the ratio of the dendritic-to somatic conductance of the cable.

2.3 RESULTS

We investigated the phenomena of direction-dependent voltage attenuation (DDVA) in type-identified cat spinal motor neurons. Our initial results of DDVA built on previous electrotonic studies of these cells using a non-uniform membrane resistivity (R_m), where R_m is different for the somatic and dendritic membrane. The question asked in these simulations was whether geometrical differences in the dendritic branching patterns of type-identified motor neurons resulted in qualitatively different DDVA? DDVA was strongly correlated with input resistance with little or no correlation to type-specific geometry of motor neuron dendrites. We then derived an analytic solution for the lumped cable parameters of alternative two-compartment models using the DDVA results from the anatomically realistic models.

2.3.1 Voltage attenuation in realistic motor neuron models

To investigate whether the dendritic geometry and passive parameters for type-identified motor neurons resulted in type-specific differences in DDVA, we calculated voltage attenuation factors in the central and peripheral direction as a function of distance from the soma. Figure 2-1 shows the anatomy of the five reconstructed motor neurons and the voltage attenuation factors. The grey dots represent the attenuation factor calculated for each dendritic segment. As predicted, there was a steep decline in attenuation with distance from the soma for the central direction and a modest decline for the peripheral direction. There were

no qualitative differences in DDVA between the different motor neuron types. The attenuation data was fit with a single exponential (solid line) to quantitatively estimate the voltage decay constant (η). There was no obvious difference in the voltage decay constants for the different types of motor neurons. The dashed lines illustrate the voltage attenuation predicted by finite cable models (with sealed end conditions) of the same cells using Equation (2-4) and (2-5). It is clear that the continuous cable models are a poor fit to the DDVA data.

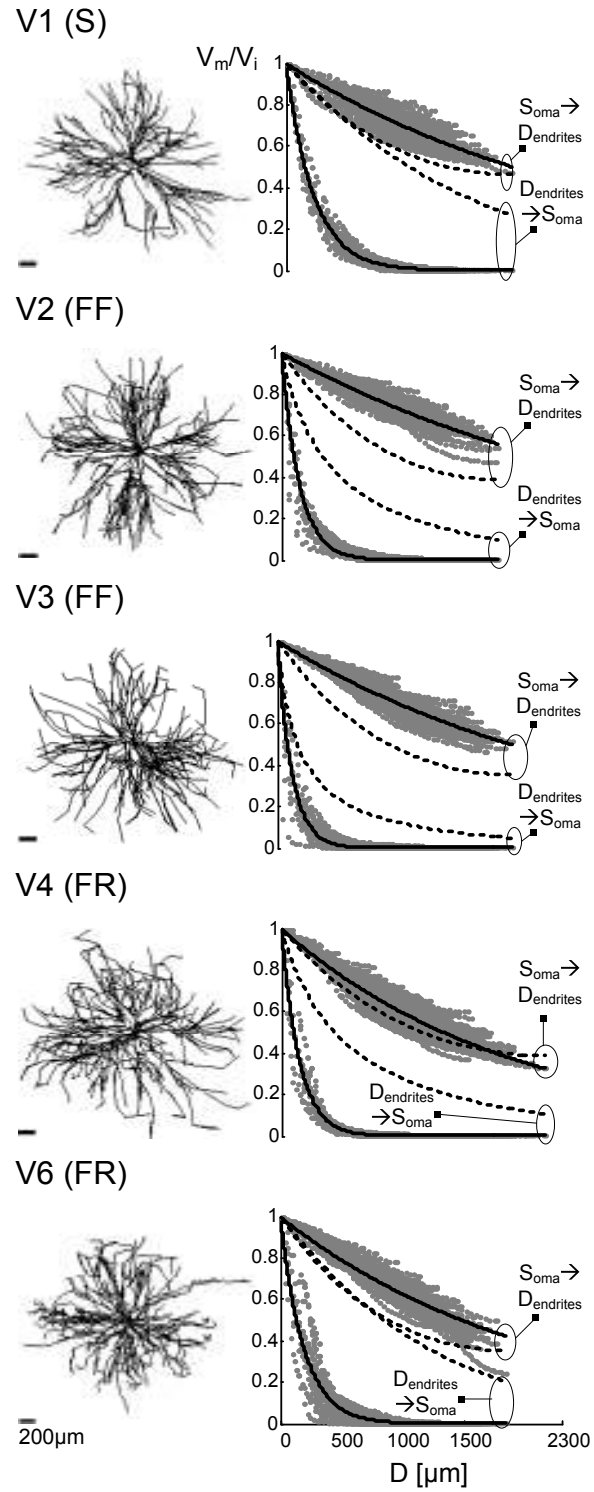


Figure 2-1. Morphology of MNs and DDVA with curve fitting . The voltage attenuation data between current injection site (V_i) and measurement site (V_m) on

the morphology of MNs for both directions from soma to dendrites and from dendrites to soma were plotted in gray along the path length (D), fitting with single exponential function (solid lines). The results from continuous cable model were displayed as dashed lines. η_{SD} from soma to dendrite and η_{DS} from dendrite to soma were determined at D where attenuation is 0.37 (e^{-1}) for each direction.

2.3.2 Voltage attenuation, motor neuron type and input resistance

While we found no obvious differences in DDVA for different motor neuron types in Fig. 2-1, a possible confounding factor was that the cells had different values of input resistance. To examine the influence of R_N we changed the specific membrane resistivity so that the anatomical models all had the same R_N and recalculated the voltage decay constant (η). This allowed comparison of different type-identified motor neuron morphologies at the same R_N . An example of the influence of R_N on the DDVA curves for the V1 motor neuron is shown in Fig. 2-2.

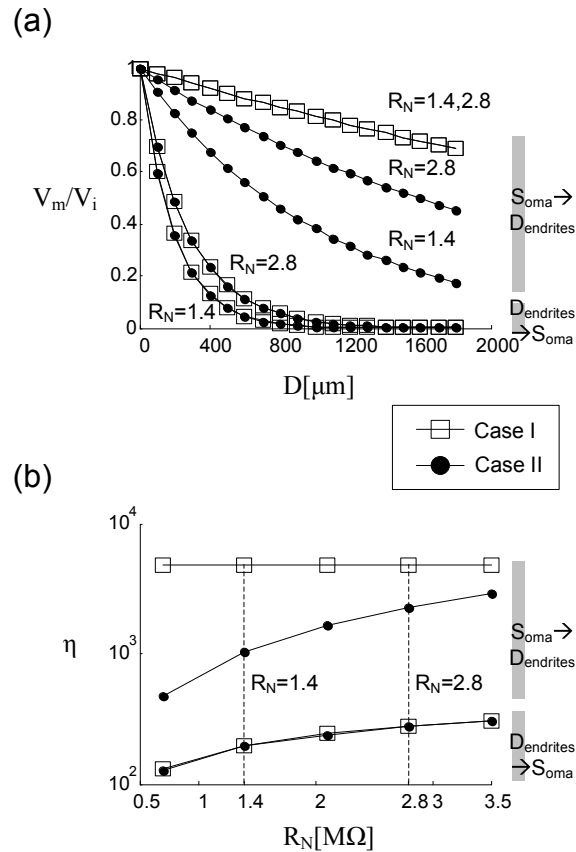


Figure 2-2. Relationship between η and R_N for V1 (Case I and II). (a) DDVA along the path of dendrites for $R_N = 1.4$ and 2.8 M Ω . (b) η in log scale computed based on (a) was plotted on R_N values ranged from 0.7 to 3.5 M Ω .

Two cases were considered: I) *Non-uniform* R_m , constant in the dendrites ($30 \text{ k}\Omega\text{-cm}^2$) and less than or equal to this value at the soma; and II) *Uniform* R_m across soma and dendrites. Case I is similar to the non-uniform membrane resistivity originally examined (Fleshman et al., 1988) and reproduced in the models of Fig. 2-1. In the non-uniform condition there was no change of the voltage decay constant in the peripheral direction when the input resistance was doubled from 1.4 to 2.8 $\text{M}\Omega$. This is shown by the overlap of the two lines in Fig. 2-2A (\square , soma \rightarrow dendrites). In the central direction, the voltage decay constant was increased from 194.6 to 278.6 μm .

In case II, uniform R_m , the voltage decay constant in the central direction was the same as case I. However, the voltage decay constant in the peripheral direction increased from 1299 to 3881 μm when R_N was increased from 1.4 to 2.8 $\text{M}\Omega$. DDVA in the V1 motor neuron was calculated for five values of R_N between 0.7 – 3.5 $\text{M}\Omega$ using both uniform and non-uniform R_m (Fig. 2-2B). There was a monotonic relationship between R_N and the voltage decay constant (η) in the central direction for the two R_m conditions. However in the peripheral direction the voltage decay constant was independent of R_N for the non-uniform case, and increased monotonically with R_N for the uniform case. These results confirm that a reduced R_m at the soma (somatic shunt) has a significant effect on the attenuation of somatic voltage back into the dendrites.

To determine if the morphology of type-identified motor neurons influenced the relationship between DDVA and R_N , we calculated the voltage decay constant (η) for six reconstructed motor neurons over a range of 0.4 – 4.0 $\text{M}\Omega$ (Fig. 2-3 (a)). These calculations were done with a uniform R_m .

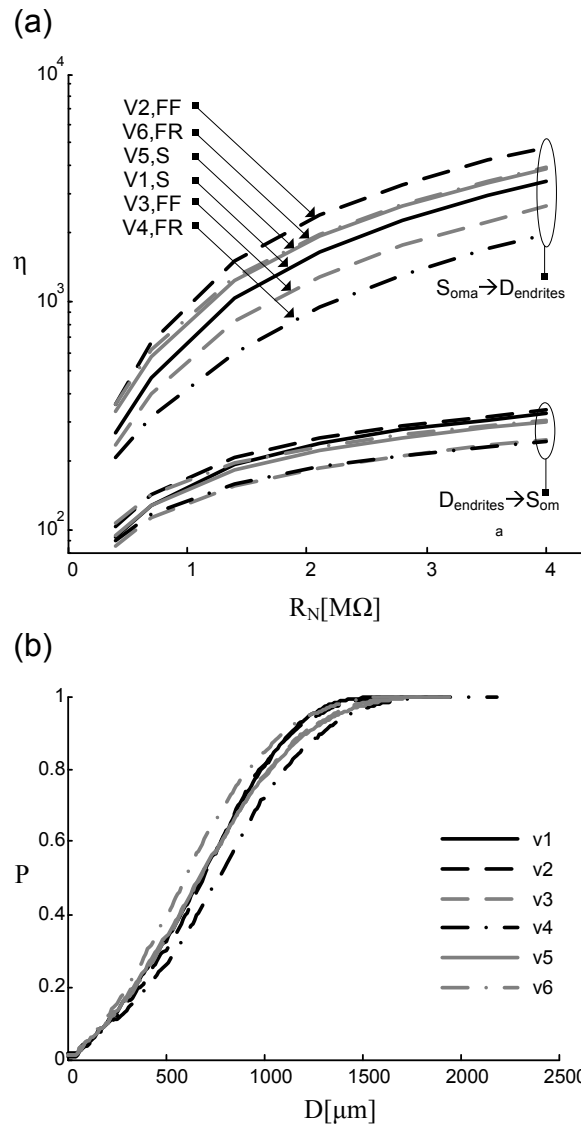


Figure 2-3. Relationship between η and R_N , and between P and D for all six models. (a) η was plotted on R_N values ranged from 0.4 to 4.0 M Ω for both directions. The different order of arrows for both current flow directions indicates the different pattern of voltage attenuation and no clustering by MN types. (b) P was plotted on D values along the dendrite from soma. P is the ratio of the surface area of soma to the total surface area.

All six motor neuron morphologies had similar relationships between R_N and η . At the same value of R_N motor neuron dendrites of different types had a range of η values; there was no evidence for a systematic difference in η for type-specific motor neuron morphology. From the limited data available, we conclude that DDVA varies as a function of R_N and the morphological characteristics of motor neuron dendrites, that give rise to asymmetric voltage attenuation, are a generic feature, not type-specific. Therefore, we decided to use the traces of $\eta = f(R_N)$ in Figure 2-3a to characterise all motor neurons in our reduced models.

2.3.3 *Development of two-compartment motor neuron models*

Having characterized DDVA, we derived the lumped cable parameters for a two-compartment model using the passive properties of the anatomically complex models. Five parameters were defined from the complex anatomical models: input resistance (R_N), membrane time constant (τ_m), central and peripheral attenuation factors (A_{DS} and A_{SD}) and the ratio between the somatic membrane area and the area of the whole neuron, $P(D)$. The attenuation factors and membrane ratio were calculated after choosing a physical distance, D , to separate the somatic from dendritic membrane areas. Values for the free parameter D can be chosen from the open interval $(0, \text{total dendrite length})$. Since this value is free, i.e. not definitively or precisely determined, the derivation holds for all possible values of D . In the specific application of the two-compartment model to spinal motor neurons we will show that the interval of appropriate values for D may be constrained with additional experimental data. The calculation of $P(D)$ was empirically derived from the anatomical data and is shown in Figure 2-3b. The ratio P as a function of distance between the soma and dendritic site overlapped for fast and slow motor neurons. Therefore, after choosing a value of D , a value for P was determined by random selection from the range of values determined by the empirical data.

The two-compartment models consisted of a somatic and dendritic part with four unknown cable parameters as shown in the equivalent circuits of Figure 2-4. Both implicit and explicit approaches were considered. The rationale for including two approaches was to determine if numerical simulations of the passive properties of the two models, following analytical derivation, would be equivalent. The explicit approach has been used before (MacGregor, 1987), however to our knowledge, this is the first use of the implicit approach for two-compartment neural models. The electrotonic properties of the implicit model included different passive membrane conductances in each compartment ($G_{m,S}$ and $G_{m,D}$), with spatially uniform membrane capacitance and coupling conductance. The explicit model used two coupling conductances ($G_{C,S}$ and $G_{C,D}$) and uniform membrane conductance and capacitance.

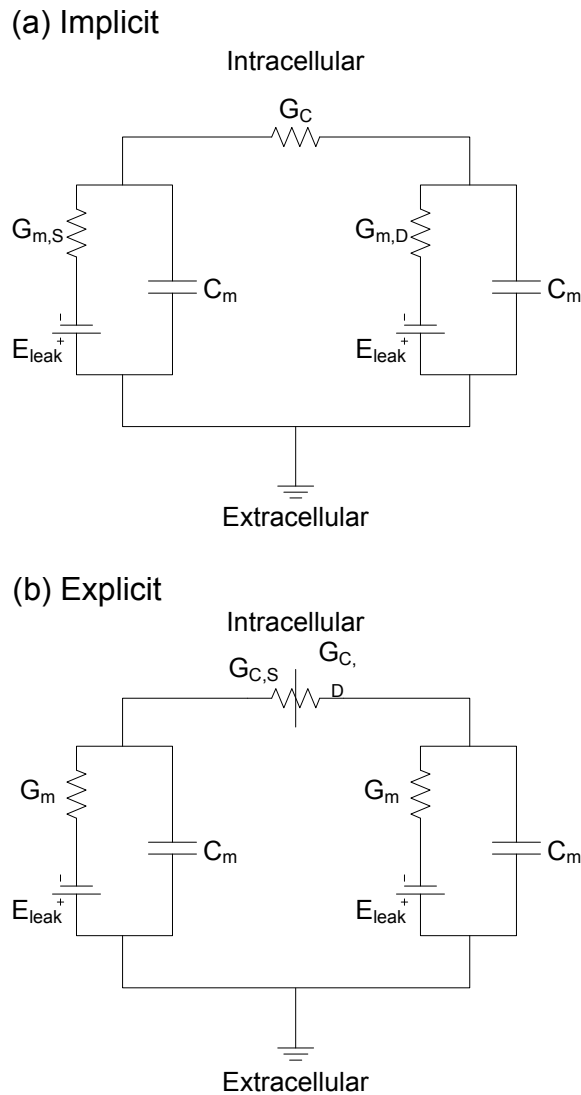


Figure 2-4. Implicit and explicit models. (a) G_C : specific coupling conductance, $G_{m,S}$: specific passive membrane conductance at soma part, C_m : specific passive membrane capacitance, $G_{m,D}$: specific passive membrane conductance of dendrite part. (b) $G_{C,S}$ and $G_{C,D}$: specific coupling conductance between two compartments, G_m : specific passive membrane conductance, C_m : specific passive membrane capacitance. E_{leak} : reversal potential for ionic leak channels. The surface area of each part can be adjusted through calculating surface area within (soma part) and outside (dendrites part) a certain distance along the dendrites.

The two models in Figure 2-4 have different system equations governing the electrotonic characteristics. The system equations for each model were derived and analyzed using two forms of current normalization: I) injected current is normalized by the surface area of each compartment (Booth and Rinzel, 1995) and II) injected current is normalized by the entire surface area of cell (Pinsky and Rinzel, 1994). We describe all equations needed for the implicit and explicit models in condition I, and attach complementary equations for condition II in the Appendix. The outline for the following section is to first develop the forward equations for the four biophysical input parameters that are defined from the complex anatomical models: R_N , A_{DS} , A_{SD} and τ_m . We then use these four equations to solve the inverse equations for the four unknown parameters in the two-compartment models: G_C , $G_{m,S}$, $G_{m,D}$ and C_m in the implicit models, and G_{CS} , G_{CD} , G_m and C_m in the explicit models. We will adopt the convention of adding the letter (a) to equations for the implicit approach and letter (b) for the explicit approach.

To derive the electrotonic properties we start with an algebraic expression for Ohm's law in steady-state conditions that states the current in the circuit is proportional to the voltage multiplied by an admittance matrix,

$$\mathbf{I} = \mathbf{B}\mathbf{V} \quad (2-6)$$

where \mathbf{I} is the vector $\begin{bmatrix} I_S \\ I_D \end{bmatrix}$ and \mathbf{V} the vector $\begin{bmatrix} V_S \\ V_D \end{bmatrix}$ whose rows represent the soma and dendritic compartments. The admittance matrix \mathbf{B} for the implicit and explicit models is,

$$\mathbf{B}_{\text{implicit}} = \begin{bmatrix} \frac{G_C}{P} + G_{m,S} + j\omega C_m & -\frac{G_C}{P} \\ -\frac{G_C}{1-P} & \frac{G_C}{1-P} + G_{m,D} + j\omega C_m \end{bmatrix} \quad (2-7)a$$

$$\mathbf{B}_{\text{explicit}} = \begin{bmatrix} \frac{G_{C,S}}{P} + G_m + j\omega C_m & -\frac{G_{C,S}}{P} \\ -\frac{G_{C,D}}{1-P} & \frac{G_{C,D}}{1-P} + G_m + j\omega C_m \end{bmatrix} \quad (2-7)\text{b}$$

where ω is the angular frequency of injected current (radians per second) and j is the square-root of -1. As an example, by carrying through the matrix multiplication for current in the soma compartment in the implicit case we get,

$$I_{S,\text{implicit}} = V_S G_{m,S} + V_S j\omega C_m + \frac{G_C}{P} (V_S - V_D)$$

that shows the somatic current is simply the sum of current across the membrane, the current resulting from the susceptance of the capacitive element and the current through the coupling conductance driven by the voltage difference between the soma and dendrite. In cases where we solve for DC input, $\omega = 0$, the current from the capacitive element drops out of the equation leaving just the real components.

The next step is to rearrange the basic matrix equation so that we can write an expression for the four parameters defined by the complex anatomical models. We start by deriving the forward equations for the three steady-state parameters: R_N , A_{SD} and A_{DS} . Firstly rearranging Equation (2-6),

$$\mathbf{V} = \mathbf{B}^{-1}\mathbf{I} \quad (2-8)$$

and setting $I_D = 0$ in Equation (2-8), we can write the expression for input resistance as,

$$r_{N,\text{implicit}} = \frac{V_S}{I_S} = \frac{P}{G_C} \cdot \left(\frac{G_{m,S}}{G_C} \cdot P + \frac{G_{m,D} \cdot (1-P)}{G_C + G_{m,D} \cdot (1-P)} \right)^{-1} \quad (2-9)\text{a}$$

$$r_{N,\text{explicit}} = \frac{V_S}{I_S} = \frac{P}{G_{C,S}} \cdot \left(\frac{G_m}{G_{C,S}} \cdot P + \frac{G_m \cdot (1-P)}{G_{C,D} + G_m \cdot (1-P)} \right)^{-1} \quad (2-9)\text{b}$$

To solve for voltage attenuation in the soma to dendrite direction with DC input, we set $I_D = 0$ and rearrange the equation to get,

$$A_{SD,implicit}^V = \frac{V_D}{V_S} = \frac{G_C}{G_C + G_{m,D} \cdot (1-P)} \quad (2-10)a$$

$$A_{SD,explicit}^V = \frac{V_D}{V_S} = \frac{G_{C,D}}{G_{C,D} + G_m \cdot (1-P)} \quad (2-10)b$$

In a similar fashion, we set $I_S = 0$ and rearrange the equation to derive an expression for the voltage attenuation from dendrites to soma with DC input,

$$A_{DS,implicit}^V = \frac{V_S}{V_D} = \frac{G_C}{G_C + G_{m,S} \cdot P} \quad (2-11)a$$

$$A_{DS,explicit}^V = \frac{V_S}{V_D} = \frac{G_{C,S}}{G_{C,S} + G_m \cdot P} \quad (2-11)b$$

Thus, we have written the forward equations for the three steady-state parameters that are determined by the complex anatomical models. The final parameter to derive an expression for is the membrane time constant that was also established by the complex models. The time constant was derived from the system equations for the equivalent circuits shown in Figure 2-4 by applying Kirchhoff's current law to each compartment to get,

$$\dot{\mathbf{V}} = \mathbf{A}\mathbf{V} + \mathbf{I} \quad (2-12)$$

$$\mathbf{V}_{implicit} = \begin{bmatrix} V_S \\ V_D \end{bmatrix}, \mathbf{I}_{implicit} = \frac{1}{C_m} \cdot \begin{bmatrix} I_S \\ I_D \end{bmatrix}, \mathbf{A}_{implicit} = \frac{1}{C_m} \cdot \begin{bmatrix} -\frac{G_C}{P} - G_{m,S} & \frac{G_C}{P} \\ \frac{G_C}{1-P} & -\frac{G_C}{1-P} - G_{m,D} \end{bmatrix}$$

$$\mathbf{V}_{\text{explicit}} = \begin{bmatrix} V_S \\ V_D \end{bmatrix}, \mathbf{I}_{\text{explicit}} = \frac{1}{C_m} \cdot \begin{bmatrix} I_S \\ I_D \end{bmatrix}, \mathbf{A}_{\text{explicit}} = \frac{1}{C_m} \cdot \begin{bmatrix} -\frac{G_{C,S}}{P} - G_m & \frac{G_{C,S}}{P} \\ \frac{G_{C,D}}{1-P} & -\frac{G_{C,D}}{1-P} - G_m \end{bmatrix}$$

where I_S and I_D are current density injected at soma and dendrite, V_S and V_D are potential differences from resting membrane potential and P is the ratio of soma area to total surface area. In two-compartment models, there are two passive membrane time constants which can be calculated analytically by finding the eigenvalues of the system matrix \mathbf{A} , and confirmed by the peeling technique (Rall, 1969). The passive voltage transient at the soma can be expressed as a sum of two exponential decays,

$$V_S(t) = C_0 e^{-t/\tau_0} + C_1 e^{-t/\tau_1} \quad (2-13)$$

and the membrane time constant is,

$$\tau_m \equiv \tau_0 = R_{\text{eff}} C_m \quad (2-14)$$

where τ_0 represents the passive membrane time constant (τ_m) and τ_1 is an equalizing time constant, less than τ_0 ; τ_0 is the reciprocal of the smaller eigenvalue for \mathbf{A} in Equation (2-12). R_{eff} , which combines the membrane resistance of the soma and dendrites, is the equivalent membrane resistance needed to calculate τ_m and can be derived through solving the characteristic equation from \mathbf{A} for all conditions. Equation (2-13) and (2-14) have the same form for the implicit and explicit models.

The left-hand sides of Equations (2-9), (2-10), (2-11) & (2-14) are known from motor neuron electrophysiology and our complex anatomical models. Since we have four equations whose LHS are known, and four unknown parameters in the two-compartment models: we can solve for the unknowns by inverting these equations. The analytical solutions for G_C , $G_{m,S}$ and $G_{m,D}$ in the implicit models are first derived from Equations (2-9) – (2-11),

$$G_C = \frac{P \cdot A_{DS,implicit}^V}{r_{N,implicit} \cdot (1 - A_{SD,implicit}^V \cdot A_{DS,implicit}^V)} \quad (2-15)a$$

$$G_{m,S} = \frac{1 - A_{DS,implicit}^V}{r_{N,implicit} \cdot (1 - A_{SD,implicit}^V \cdot A_{DS,implicit}^V)} \quad (2-15)b$$

$$G_{m,D} = \frac{P \cdot A_{DS,implicit}^V \cdot (1 - A_{SD,implicit}^V)}{(1 - P) \cdot r_{N,implicit} \cdot A_{SD,implicit}^V \cdot (1 - A_{SD,implicit}^V \cdot A_{DS,implicit}^V)} \quad (2-15)c$$

Then the C_m can be obtained from Equation (2-14) using the conductances in Equations (2-15)a-c,

$$C_m = \tau_m / R_{eff,implicit} \quad (2-15)d$$

where the effective resistance of the implicit model is given by,

$$R_{eff,implicit} = \frac{2P(P-1)}{\sqrt{G_C^2 + 2(G_{m,S} - G_{m,D}) \cdot (I-2P) \cdot (I-P)PG_C + (G_{m,S}^2 + G_{m,D}^2 - 2G_{m,S}G_{m,D}) \cdot (I-P)^2 P^2 + P(P-1)(G_{m,S} + G_{m,D}) - G_C}} \quad (2-15)e$$

In the same way the analytic solutions of the cable parameters in the explicit model are,

$$G_{C,S} = \frac{P \cdot A_{DS,explicit}^V}{r_{N,explicit} \cdot (1 - A_{SD,explicit}^V \cdot A_{DS,explicit}^V)} \quad (2-16)a$$

$$G_{C,D} = \frac{(1-P) \cdot A_{SD,explicit}^V \cdot (1 - A_{DS,explicit}^V)}{r_{N,explicit} \cdot (1 - A_{SD,explicit}^V \cdot A_{DS,explicit}^V) \cdot (1 - A_{SD,explicit}^V)} \quad (2-16)b$$

$$G_m = \frac{1 - A_{DS,explicit}^V}{r_{N,explicit} \cdot (1 - A_{SD,explicit}^V \cdot A_{DS,explicit}^V)} \quad (2-16)c$$

The C_m in the explicit models is solved using Equation (2-14) and uses the conductances in Equations (2-16)a-c,

$$C_m = \tau_m / R_{\text{eff,explicit}} \quad (2-16)\text{d}$$

where the effective resistance of the explicit model is given by,

$$R_{\text{eff,explicit}} = \frac{1}{G_m} \quad (2-16)\text{e}$$

This completes the derivation of the lumped cable parameters for our two-compartment reduction using the passive properties of the anatomically complex models. Equations (2-15) a-e can be used to solve for all the cable parameters of the implicit model and equations (2-16) a-e for the parameters of the explicit model starting from well-defined biophysical input parameters of spinal motor neurons and choosing a distance for separating the soma and dendritic compartments. The value for the separation distance is not free because experimental and theoretical results provide evidence that the plateau generating channels are localized in a cluster on restricted regions of the dendrites (Ballou et al., 2006; Bui et al., 2006; Carlin et al., 2000b; Elbasiouny et al., 2005; Grande et al., 2007). We remind the reader that these inverse equations are for the condition where injected current is normalized by the surface area of each compartment (Booth and Rinzel, 1995). The complimentary equations for the condition where injected current is normalized to the total surface area (Pinsky and Rinzel, 1994) are in the Appendix.

The analytical derivation of the two sets of equations for the implicit and explicit approaches did not reveal any strengths or weaknesses that would favour using one approach over the other. To determine which approach is better, we evaluated the equations on three measures: 1) do they analytically satisfy the requirement of direction-dependent current attenuation; 2) do they exhibit differences in global sensitivity of their four output parameters; and 3) do simulations with the implicit and explicit equations accurately predict changes in local dendritic input resistance as a function of distance from the soma?

2.3.4 Direction-dependent current attenuation

In order to determine if the current attenuation satisfied established biophysical principles, we derived the direction-dependent current attenuation (DDCA) using the voltage clamp method suggested by (Carnevale and Johnston, 1982).

Clamping the soma at resting potential, V_S is set to 0 mV in Equation (2-6).

Multiplying the current density in each compartment by the surface area of each compartment, the steady-state current attenuation from soma to dendrites is

$$A_{SD,implicit}^I = \frac{I_D \cdot SA_{Dendrite}}{I_S \cdot SA_{Soma}} = \frac{G_C}{G_C + G_{m,S} \cdot P} \quad (2-17a)$$

$$A_{SD,explicit}^I = \frac{I_D \cdot SA_{Dendrite}}{I_S \cdot SA_{Soma}} = \frac{G_{C,D}}{G_{C,S} + G_m \cdot P} \quad (2-17b)$$

Clamping the dendrite compartment at resting potential, V_D is set to 0 mV in Equation (2-6). Multiplying the current density in each compartment by the surface area of each compartment, the steady-state current attenuation from dendrite to soma is

$$A_{DS,implicit}^I = \frac{I_S \cdot SA_{Soma}}{I_D \cdot SA_{Dendrite}} = \frac{G_C}{G_C + G_{m,D} \cdot (1 - P)} \quad (2-18a)$$

$$A_{DS,explicit}^I = \frac{I_S \cdot SA_{Soma}}{I_D \cdot SA_{Dendrite}} = \frac{G_{C,S}}{G_{C,D} + G_m \cdot (1 - P)} \quad (2-18b)$$

where SA_{Soma} and $SA_{Dendrite}$ are the surface area of the soma and dendrite compartments.

One of the conclusions of two-port analysis applied to dendritic neurons is that voltage attenuation in one direction is equal to current attenuation in the opposite direction (Carnevale and Johnston, 1982). The derivations above show that this equality is true only for the implicit case: Eq 2-10(a) = Eq 2-18(a) & Eq 2-11(a) =

Eq 2-17(a). For the explicit model the direction specific coupling conductances create an inequality: Eq 2-10(b) \neq Eq 2-18(b) & Eq 2-11(b) \neq Eq 2-17(b). The outcome of this test showed that the implicit was better than the explicit approach.

2.3.5 *Global sensitivity analysis*

Another way to evaluate the implicit and explicit modelling approaches was to determine the range and variation of the four output parameters in Equations (2-15)a-d and (2-16)a-d to the full breadth of input parameters: R_N , D and τ_m . This type of study is also known as global sensitivity analysis (Saltelli, 2004). We assumed the three input parameters were independent and chose values for the input parameters from the literature (R_N values 0.4 – 4.0 M Ω , τ_m values 3 – 15 ms (Zengel et al., 1985)) and the anatomy of the reconstructed cells (D values 58 – 1750 μm). The values for the A_{DS} and A_{SD} inputs to the models were determined from the analysis in Figure 2-3a, and so were dependent on the value of R_N . Figure 2-5 illustrates this analysis for a membrane time constant of 7.1 ms. The key result of this analysis was evidence that the two-compartment reductions could be solved for all combinations of input parameters tested. No differences between the implicit and explicit approaches were found to prefer one approach to the other.

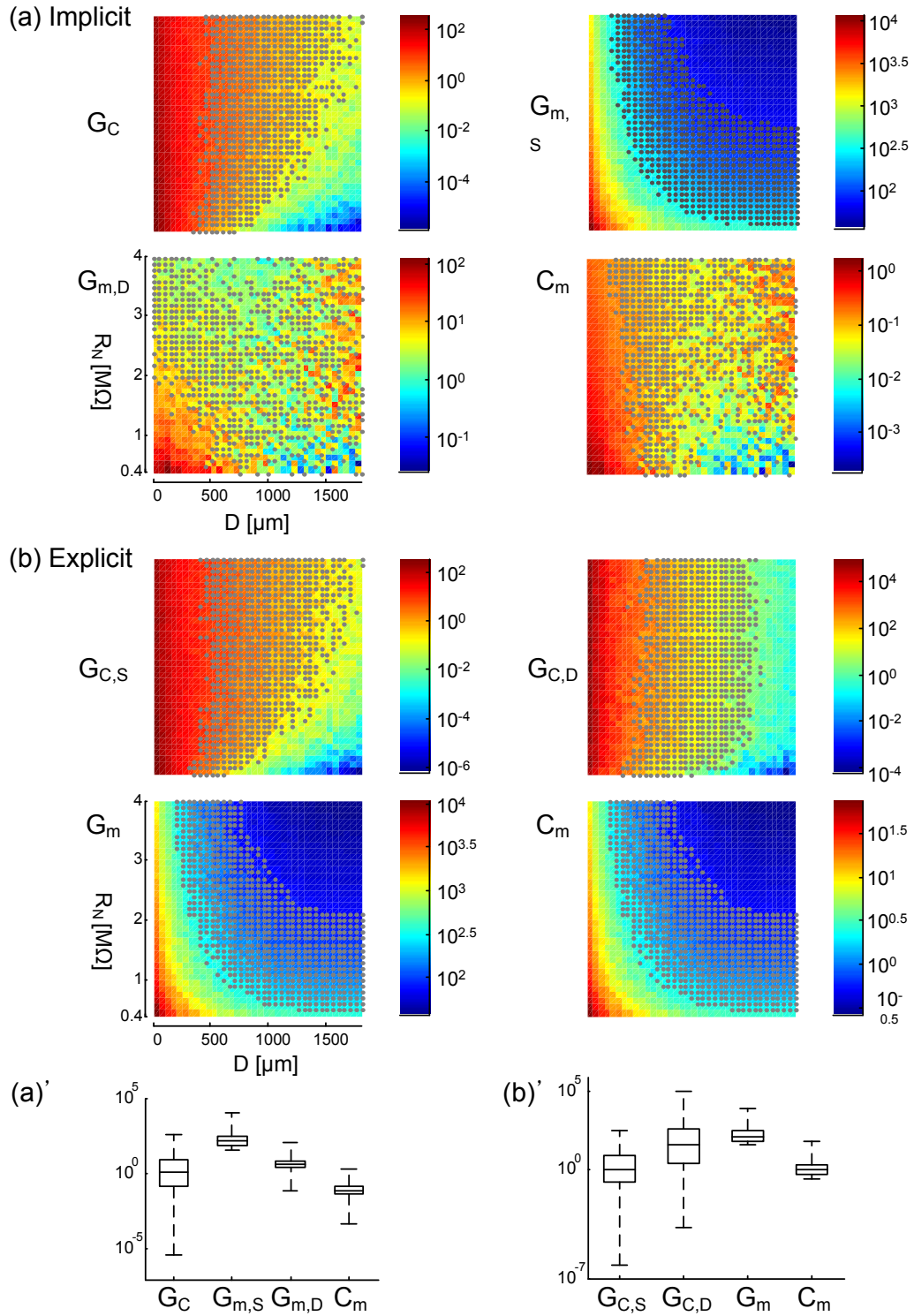


Figure 2-5. Distribution of passive membrane parameters according to R_N and D with $\tau_m = 7.1$ ms. The sampling grid was uniformly spaced between $R_N = 0.4 - 4.0$ M Ω with a resolution of 0.1 M Ω and $D = 58 - 1750$ μ m with a resolution of

47 μm . The colour bar in each graph indicates the value of each passive membrane property in logarithmic scale. Gray dots are overlaid on the colour plot where the value of the passive parameter falls within the interquartile range for that parameter. (a) For implicit model I: 1) G_C [$\mu\text{S}/\text{cm}^2$], 2) $G_{m,S}$ [$\mu\text{S}/\text{cm}^2$], 3) $G_{m,D}$ [$\mu\text{S}/\text{cm}^2$], 4) C_m [$\mu\text{F}/\text{cm}^2$] and (a)' Box and whisker plots of all parameter values. The interquartile range of each parameter: $0.14 < G_C < 8.75 \mu\text{S}/\text{cm}^2$, $69.9 < G_{m,S} < 321.5 [\mu\text{S}/\text{cm}^2]$, $2.24 < G_{m,D} < 6.82 [\mu\text{S}/\text{cm}^2]$, $0.04 < C_m < 0.14 \mu\text{F}/\text{cm}^2$. (b) For explicit model I: 1) $G_{C,S}$ [$\mu\text{S}/\text{cm}^2$], 2) $G_{C,D}$ [$\mu\text{S}/\text{cm}^2$], 3) G_m [$\mu\text{S}/\text{cm}^2$], 4) C_m [$\mu\text{F}/\text{cm}^2$] and (b)' Box and whisker plots of all parameter values. The interquartile range of each parameter: $0.15 < G_{C,S} < 8.85 \mu\text{S}/\text{cm}^2$, $2.54 < G_{C,D} < 451.5 \mu\text{S}/\text{cm}^2$, $70.6 < G_m < 324.5 [\mu\text{S}/\text{cm}^2]$, $0.49 < C_m < 2.27 \mu\text{F}/\text{cm}^2$.

The colour gradient in Figure 2-5 represents the logarithm of the value for a particular cable parameter output. The grey dots overlaid on the gradient indicate parameter values within the interquartile range. The coupling conductance (G_C) of the implicit model had a median value of $1.1 \mu\text{S}/\text{cm}^2$ and was more sensitive to changes in D than R_N . This is shown by the orientation of the colour gradient that changed primarily along the horizontal axis (Fig. 2-5(a) Implicit, G_C). In contrast, the membrane conductance of the soma varied as a function of both D and R_N , i.e. the colour gradient changed along a diagonal of the plot (Fig. 2-5(a) Implicit, $G_{m,S}$). The correlation of $G_{m,S}$ with D and R_N is also apparent in the non-linear distribution of the interquartile range. The solutions for the implicit model resulted in much higher conductance per unit area for the soma, median value 135.4 , compared to $3.9 \mu\text{S}/\text{cm}^2$ in the dendrite ($G_{m,D}$). Membrane conductance of the dendrite as a function of D and R_N was qualitatively different from the soma. The interquartile range of the solutions (grey dots) was more diffuse compared to the soma and the colour gradient had two regions of high values, bottom left and along the far right edge. Perhaps most surprising was the low median values of specific membrane capacitance in the implicit model, $0.07 \mu\text{F}/\text{cm}^2$. C_m in the implicit model was more sensitive to D with highest levels at short and long distances from the soma.

The distribution of values for the two coupling conductances in the explicit model were similar to coupling conductance in the implicit model, being more sensitive to changes in D compared to R_N (Fig. 2-5(b) Explicit, $G_{C,S}$ & $G_{C,D}$). The median value for $G_{C,S}$ was the same as G_C , $1.1 \mu\text{S}/\text{cm}^2$, while the median value for $G_{C,D}$ was much greater, $38.3 \mu\text{S}/\text{cm}^2$. The uniform membrane conductance of the explicit model had a similar distribution and median value ($135.8 \mu\text{S}/\text{cm}^2$) compared to $G_{m,S}$ in the implicit model. The median value of C_m was $0.9 \mu\text{F}/\text{cm}^2$ and had a nonlinear sensitivity to both R_N and D (Fig. 2-5(b) Explicit, C_m).

Overall Figure 2-5 illustrates that by using experimental measurements of R_N , τ_m and distance from the soma at which to segregate the compartments, the lumped

cable parameters of the two-compartment models can be solved. Since the main coupling parameters: G_C , $G_{C,S}$, $G_{C,D}$ and P are constrained by the anatomy and passive electrical properties of reconstructed spinal motor neurons, these models provide a biologically realistic reduction compared to models that do not constrain the coupling parameters. This analysis provided no evidence to choose between the implicit and explicit as the better approach.

2.3.6 Input resistance in the dendritic compartment

The last evaluation of the implicit versus explicit modelling approaches calculated the input resistance of the dendritic compartment and compared that with results from the anatomically complex models. The results of comparison with anatomical model V1 are shown in Figure 2-6. The local input resistance in the anatomical model increased with distance from the soma as expected. The input resistance calculated using the implicit approach was a good representation of the data calculated from the anatomically complex model. The explicit model failed at predicting the input resistance of the anatomically complex model at distances less than about 1500 microns. The closest distance to the soma that was evaluated was 50 μm . At this distance the implicit model had a value of 2.3 $\text{M}\Omega$ (just slightly higher than the value of 1.9 $\text{M}\Omega$ in the adjacent soma compartment); the value for the explicit model was 0.004 $\text{M}\Omega$ (drastically reduced from the value of 1.9 $\text{M}\Omega$ in the adjacent soma compartment). The outcome of this test showed that the implicit was better than the explicit approach.

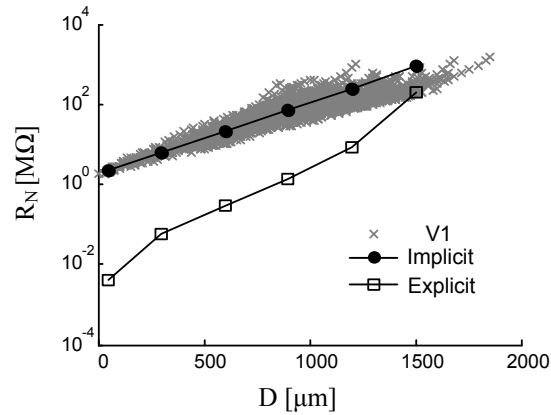


Figure 2-6. Input resistance of two-compartment models. The local input resistance (R_N) of the realistic model was measured on the V1 in Table 2-1 and plotted along the distance (D) from the soma (grey cross). The input resistance of V1 was fit by a single exponential function (black dashed line). The input resistance of the implicit model (black filled circle) was well fit to that of V1, but the explicit model showed unrealistically lower values at the dendritic compartment than those of V1, especially as $D \rightarrow 0$.

2.4 DISCUSSION

Our results support the hypothesis that the major determinants of DDVA in motor neurons are R_m and a generic dendritic morphology. There was no evidence for a type-specific dendrite morphological effect on DDVA. DDVA in a motor neuron could be captured by two single-exponential functions with separate voltage decay constants for the central and peripheral directions: η_{SD} and η_{DS} . We then showed that this result could be used to derive the parameters for electrotonic coupling in lumped two-compartment approximations of motor neurons. The unique contribution of this result was that we directly derived values for the lumped cable parameters from the known passive parameters and anatomy of our realistic models. We showed that solutions for the cable parameters in the lumped two-compartment models exist over the full range of passive properties that characterise the heterogeneous spinal motor neuron pool. We then determined, using a variety of measures, that the implicit two-compartment reduction was superior to the explicit approach.

2.4.1 Critical assessment of the models and results

The conclusion that the morphological features of dendrites that contribute to DDVA are generic, rather than unique for slow (S) and fast (FR, FF) motor neurons, must be qualified as tentative given the small data set. The six motor neurons used in this study are the only type-identified reconstructions that are publicly available. The anatomy for an additional eight alpha motor neurons innervating the hindlimb muscles of the cat have been deposited to the NeuroMorpho.org database by the Fyffe laboratory (Alvarez et al., 1998). These motor neurons were type-identified on the basis of electrophysiology, however there are no identifiers in the NeuroMorpho.org database or published literature that permitted linking anatomy to measured electrophysiology and motor neuron type. Additional data that includes anatomy and electrophysiology from the same

type-identified motor neurons is needed to determine if the lack of evidence for type-specific morphological effects on DDVA is a consistent finding.

Our results are not general for all mammalian motor neurons or even all cat motor neurons. The six motor neurons in our study innervated the calf muscles that are located in a certain column of the ventral horn in the lumbar spinal cord (Yakovenko et al., 2002). The dendritic organization of motor neurons changes with location of the cell bodies and local space limitations (Schoenen, 1982). For example researchers studying electrotonic properties of motor neurons innervating the neck and eye muscles have found evidence for functional subunits (Bras et al., 1993; Korogod et al., 1994; Rose and Cushing, 2004). If there were evidence for functional subunits in our DDVA analysis, we were prepared to lump the reduced models into more than two-compartments. For example, had there been two clusters of peripheral voltage attenuation data in Figure 2-1, we could have treated each cluster as a separate compartment and proceeded to derive a three-compartment reduction. This solution may be needed for motor neurons that have dendrites that are preferentially oriented along different axes such as neck (Rose and Cushing, 2004), vagal (Nitzan et al., 1990) or phrenic motor neurons (Cameron et al., 1991). We suggest that where adequate anatomy and electrophysiology from the same neurons exist, an analysis of the DDVA features be used to determine if a two-compartment reduction is appropriate.

By choosing to lump the soma and proximal dendritic membrane into one compartment and the remaining dendritic membrane into another we are making some implicit assumptions about the phenomenon of interest and scope of the model. For example, the detailed distribution of synaptic inputs to the dendritic tree is lost. This sacrifice in detail was made because the ultimate goal for the two-compartment model was to understand how the non-uniform distribution of spiking and plateau potential currents, interact in a structure that has asymmetric coupling. The type of analysis needed to determine the effect of asymmetric coupling on the dynamical behaviour is best pursued using reduced models

(Rinzel and Ermentrout, 1998). The reduced model will also facilitate the construction and analysis of a pool of motor neurons that include a realistic distribution of passive and active parameters.

The other limitation of our derivation is that the DDVA analysis used to derive the cable parameters has been limited to DC. This decision was made because the phenomenon of interest was the coupling of plateau potential currents in the dendritic region that are relatively low frequency. Were we interested in back propagation of action potentials, it would have been appropriate to derive the cable parameters for the lumped two-compartment models using AC impedance analysis of DDVA. Though not shown we did compare the voltage attenuation at 250 Hz for the realistic, explicit and implicit reduced models. This frequency was chosen because the average spike width for these motor neurons is about 2 ms and assuming the spike represents half a period of a sinusoidal input, i.e. 4 ms period is equivalent to 250 Hz. For the realistic models, voltage attenuation at 250 Hz in the peripheral direction was greater than at DC, yet there remained a strong asymmetry when compared to central DC attenuation. This asymmetry in comparing peripheral DDVA at 250 Hz and central DDVA at DC should be examined in more detail.

The derivation of the implicit and explicit two-compartment reductions included input resistance at the soma however; input resistance in the dendritic compartment was not part of the analytical derivation. When the implicit and explicit approaches were compared on this measure, the implicit model fit the data from the anatomically complex model but the explicit model did not. The reason the explicit model did not predict realistic dendritic input resistance was the relative difference in the two coupling conductances ($G_{CS} \ll G_{CD}$). Therefore the implicit model is the best approach for analysis of coupling at low frequencies since it satisfied direction dependant voltage attenuation, direction dependant current attenuation, and input resistance in both compartments over the full range of distances between the soma and dendrites.

2.4.2 *Comparison with other studies*

The impetus for this study was the use of two-compartment models to capture the output firing patterns of a wide range of neurons, including turtle motor neurons (Booth and Rinzel, 1995; Booth et al., 1997; Mainen and Sejnowski, 1996; Pinsky and Rinzel, 1994). These previous models treated the electrotonic coupling parameters: coupling conductance g_c and relative surface area p , as independent and free parameters that could be adjusted to produce different output firing patterns. We chose to remove the independence of these two parameters and make them dependent on the anatomy and passive electrotonic properties of the neurons of interest. By specifying a separation distance in micrometers for the soma and dendritic compartments and assigning a realistic R_N and τ_m , the electrotonic coupling parameters are constrained to the neurons of interest. We think that this constraint and retaining the asymmetry in voltage attenuation could be important for realistic analysis of excitable dendrites in motor neurons.

For example, it is well accepted that persistent inward currents exist on motor neuron dendrites and these currents can generate plateau potentials and persistent firing (Heckman and Lee, 1999a; Heckman and Lee, 1999b; Heckmann et al., 2005). How far does a dendritic plateau potential propagate? Is there a relationship between location of the persistent inward currents and measurements such as input resistance that varies widely across a pool of motor neurons? Since the distribution and kinetics of the ion channels underlying the plateau potentials remain unknown and voltage clamp protocols at the soma preclude definitive experimental measurement of these channels (Williams and Mitchell, 2008), modelling could help answer these questions. Asymmetry of passive electrotonic spread in dendrites is inherent to these questions; therefore we sought to develop a reduced model that retained this feature. In previous reduced models of motor neurons the DC coupling between the soma and dendrite was either symmetric (Booth and Rinzel, 1995) or asymmetric but in the opposite direction (Booth et al., 1997). Our early results suggest that the parameter space exhibiting stable

dynamic features such as bistability, are strongly affected by the asymmetric coupling of two-compartment models (Kim et al., 2008).

2.5 CONCLUSION

Fundamental insights about single neuron computation have emerged from simplified two-compartment models. We have provided an analytical solution for the lumped cable parameters in two-compartment models of motor neurons with asymmetric coupling between dendrites and soma. Studies are now needed to determine the effect of this asymmetry on the nonlinear dynamics of two-compartment models. These future studies should use the implicit modelling approach developed here instead of the explicit approach that has been used in the past.

2.6 APPENDIX FOR CHAPTER 2

Equations for implicit and explicit models in the case II

The system equations for the case II with inject current normalized by the entire surface area of cell can be derived by replacing current density injected at soma and dendrite in Equations (2-6) and (2-12) with

$$\begin{bmatrix} I_S \\ I_D \end{bmatrix} \rightarrow \begin{bmatrix} I_S / P \\ I_D / (1 - P) \end{bmatrix} \quad (2-A1)$$

To obtain an expression for the electrotonic properties for case II, we need to multiply the matrix \mathbf{B} in Equation (2-6) by P and apply $I_D=0$ to Equation (2-8) derived for the case II under steady-state conditions: the specific input resistance is,

$$r_{N,implicit} = \frac{1}{G_C} \cdot \left(\frac{G_{m,S} \cdot P}{G_C} + \frac{G_{m,D} \cdot (1-P)}{G_C + G_{m,D} \cdot (1-P)} \right)^{-1} \quad (2-A2)a$$

$$r_{N,explicit} = \frac{1}{G_{C,S}} \cdot \left(\frac{G_m \cdot P}{G_{C,S}} + \frac{G_m \cdot (1-P)}{G_{C,D} + G_m \cdot (1-P)} \right)^{-1} \quad (2-A2)b$$

the voltage attenuation for both directions with DC input is,

$$A_{SD,implicit}^V = \frac{G_C}{G_C + G_{m,D} \cdot (1-P)}, \quad A_{DS,implicit}^V = \frac{G_C}{G_C + G_{m,S} \cdot P} \quad (2-A3)a$$

$$A_{SD,explicit}^V = \frac{G_{C,D}}{G_{C,D} + G_m \cdot (1-P)}, \quad A_{DS,explicit}^V = \frac{G_{C,S}}{G_{C,S} + G_m \cdot P} \quad (2-A3)b$$

The passive membrane time constant for implicit and explicit models is consistent with Equations (2-13) and (2-14) in the case I because the system matrix \mathbf{A} in Equation (2-12) is not affected by the replacement with Equation (2-A1), thereby R_{eff} of case II is identical to those of case I.

$$\tau_{m,implicit} = R_{eff,implicit} \cdot C_m \quad (2-A4)a$$

$$\tau_{m,explicit} = R_{eff,explicit} \cdot C_m \quad (2-A4)b$$

All passive membrane parameters can be derived analytically as in the case I: G_C , $G_{m,S}$, $G_{m,D}$ in implicit models and $G_{C,S}$, $G_{C,D}$, G_m in explicit models from Equations (2-A2) and (2-A3) are

$$G_C = \frac{A_{DS,implicit}^V}{r_{N,implicit} \cdot (1 - A_{SD,implicit}^V \cdot A_{DS,implicit}^V)} \quad (2-A5)a$$

$$G_{m,S} = \frac{1 - A_{DS}^V}{P \cdot r_{N,implicit} \cdot (1 - A_{SD,implicit}^V \cdot A_{DS,implicit}^V)} \quad (2-A5)b$$

$$G_{m,D} = \frac{A_{DS,implicit}^V \cdot (1 - A_{SD,implicit}^V)}{(1 - P) \cdot r_{N,implicit} \cdot A_{SD,implicit}^V \cdot (1 - A_{SD,implicit}^V \cdot A_{DS,implicit}^V)} \quad (2-A5)c$$

$$G_{C,S} = \frac{A_{DS,explicit}^V}{r_{N,explicit} \cdot (1 - A_{SD}^V \cdot A_{DS}^V)} \quad (2-A6)a$$

$$G_{C,D} = \frac{(1 - P) \cdot A_{SD,explicit}^V \cdot (1 - A_{DS,explicit}^V)}{P \cdot r_{N,explicit} \cdot (1 - A_{SD,explicit}^V \cdot A_{DS,explicit}^V) \cdot (1 - A_{SD,explicit}^V)} \quad (2-A6)b$$

$$G_m = \frac{1 - A_{DS,explicit}^V}{P \cdot r_{N,explicit} \cdot (1 - A_{SD,explicit}^V \cdot A_{DS,explicit}^V)} \quad (2-A6)c$$

Then C_m in implicit and explicit models from Equation (2-A4) based on previously determined parameter values are

$$C_m = \tau_m / R_{\text{eff},\text{implicit}} \quad (2-A5)d$$

$$C_m = \tau_m / R_{\text{eff},\text{explicit}} \quad (2-A6)d$$

2.7 BIBLIOGRAPHY FOR CHAPTER 2

Alvarez, F. J., Pearson, J. C., Harrington, D., Dewey, D., Torbeck, L., and Fyffe, R. E. (1998). Distribution of 5-hydroxytryptamine-immunoreactive boutons on alpha-motoneurons in the lumbar spinal cord of adult cats. *J Comp Neurol* 393, 69-83.

Ascoli, G. A. (2006). Mobilizing the base of neuroscience data: the case of neuronal morphologies. *Nat Rev Neurosci* 7, 318-324.

Ballou, E. W., Smith, W. B., Anelli, R., and Heckman, C. J. (2006). Measuring dendritic distribution of membrane proteins. *J Neurosci Methods* 156, 257-266.

Booth, V., and Rinzel, J. (1995). A minimal, compartmental model for a dendritic origin of bistability of motoneuron firing patterns. *J Comput Neurosci* 2, 299-312.

- Booth, V., Rinzel, J., and Kiehn, O. (1997). Compartmental model of vertebrate motoneurons for Ca²⁺-dependent spiking and plateau potentials under pharmacological treatment. *J Neurophysiol* 78, 3371-3385.
- Bras, H., Korogod, S., Driencourt, Y., Gogan, P., and Tyc-Dumont, S. (1993). Stochastic geometry and electronic architecture of dendritic arborization of brain stem motoneuron. *Eur J Neurosci* 5, 1485-1493.
- Bui, T. V., Ter-Mikaelian, M., Bedrossian, D., and Rose, P. K. (2006). Computational estimation of the distribution of L-type Ca(2+) channels in motoneurons based on variable threshold of activation of persistent inward currents. *J Neurophysiol* 95, 225-241.
- Burke, R. E., Levine, D. N., Tsairis, P., and Zajac, F. E., 3rd (1973). Physiological types and histochemical profiles in motor units of the cat gastrocnemius. *J Physiol* 234, 723-748.
- Cameron, W. E., He, F., Kalipatnapu, P., Jodkowski, J. S., and Guthrie, R. D. (1991). Morphometric analysis of phrenic motoneurons in the cat during postnatal development. *J Comp Neurol* 314, 763-776.
- Carlin, K. P., Jiang, Z., and Brownstone, R. M. (2000a). Characterization of calcium currents in functionally mature mouse spinal motoneurons. *Eur J Neurosci* 12, 1624-1634.
- Carlin, K. P., Jones, K. E., Jiang, Z., Jordan, L. M., and Brownstone, R. M. (2000b). Dendritic L-type calcium currents in mouse spinal motoneurons: implications for bistability. *Eur J Neurosci* 12, 1635-1646.
- Carnevale, N. T., and Hines, M. L. (2005). *The NEURON book* (Cambridge ; New York: Cambridge University Press).
- Carnevale, N. T., and Johnston, D. (1982). Electrophysiological characterization of remote chemical synapses. *J Neurophysiol* 47, 606-621.

- Coombs, J. S., Eccles, J. C., and Fatt, P. (1955). The electrical properties of the motoneurone membrane. *J Physiol* *130*, 291-325.
- Cullheim, S., Fleshman, J. W., Glenn, L. L., and Burke, R. E. (1987a). Membrane area and dendritic structure in type-identified triceps surae alpha motoneurons. *J Comp Neurol* *255*, 68-81.
- Cullheim, S., Fleshman, J. W., Glenn, L. L., and Burke, R. E. (1987b). Three-dimensional architecture of dendritic trees in type-identified alpha-motoneurons. *J Comp Neurol* *255*, 82-96.
- Elbasiouny, S. M., Bennett, D. J., and Mushahwar, V. K. (2005). Simulation of dendritic CaV1.3 channels in cat lumbar motoneurons: spatial distribution. *J Neurophysiol* *94*, 3961-3974.
- Fleshman, J. W., Segev, I., and Burke, R. B. (1988). Electrotonic architecture of type-identified alpha-motoneurons in the cat spinal cord. *J Neurophysiol* *60*, 60-85.
- Frank, K., and Fuortes, M. G. (1955). Potentials recorded from the spinal cord with microelectrodes. *J Physiol* *130*, 625-654.
- Grande, G., Bui, T. V., and Rose, P. K. (2007). Estimates of the location of L-type Ca²⁺ channels in motoneurons of different size: a computational study. *J Neurophysiol* *97*, 4023-4035.
- Heckman, C. J., and Lee, R. H. (1999a). The role of voltage-sensitive dendritic conductances in generating bistable firing patterns in motoneurons. *J Physiol Paris* *93*, 97-100.
- Heckman, C. J., and Lee, R. H. (1999b). Synaptic integration in bistable motoneurons. *Prog Brain Res* *123*, 49-56.

- Heckman, C. J., Lee, R. H., and Brownstone, R. M. (2003). Hyperexcitable dendrites in motoneurons and their neuromodulatory control during motor behavior. *Trends Neurosci* 26, 688-695.
- Heckmann, C. J., Gorassini, M. A., and Bennett, D. J. (2005). Persistent inward currents in motoneuron dendrites: implications for motor output. *Muscle Nerve* 31, 135-156.
- Holmes, W. R., and Rall, W. (1992). Electrotonic length estimates in neurons with dendritic tapering or somatic shunt. *J Neurophysiol* 68, 1421-1437.
- Hounsgaard, J., Hultborn, H., Jespersen, B., and Kiehn, O. (1984). Intrinsic membrane properties causing a bistable behaviour of alpha-motoneurons. *Exp Brain Res* 55, 391-394.
- Jack, J. J. B., Noble, D., and Tsien, R. W. (1975). *Electric current flow in excitable cells* (Oxford: Clarendon Press).
- Jones KE, C. K., J. R., et al. (2000). Simulation techniques for localising and identifying the kinetics of calcium channels in dendritic neurons. *Neurocomputing* 32, 173-180.
- Kim, H., Major, L. A., and Jones, K. E. (2008). Voltage attenuation in reconstructed type-identified motor neurons as a constraint for reduced models. *BMC Neuroscience* 9(Suppl 1), P55.
- Korogod, S., Bras, H., Sarana, V. N., Gogan, P., and Tyc-Dumont, S. (1994). Electrotonic clusters in the dendritic arborization of abducens motoneurons of the rat. *Eur J Neurosci* 6, 1517-1527.
- Lee, R. H., and Heckman, C. J. (1996). Influence of voltage-sensitive dendritic conductances on bistable firing and effective synaptic current in cat spinal motoneurons in vivo. *J Neurophysiol* 76, 2107-2110.

- Lee, R. H., and Heckman, C. J. (1998a). Bistability in spinal motoneurons in vivo: systematic variations in persistent inward currents. *J Neurophysiol* 80, 583-593.
- Lee, R. H., and Heckman, C. J. (1998b). Bistability in spinal motoneurons in vivo: systematic variations in rhythmic firing patterns. *J Neurophysiol* 80, 572-582.
- Lee, R. H., and Heckman, C. J. (1999). Enhancement of bistability in spinal motoneurons in vivo by the noradrenergic alpha 1 agonist methoxamine. *J Neurophysiol* 81, 2164-2174.
- MacGregor, R. J. (1987). *Neural and brain modeling* (San Diego, Calif.: Academic Press).
- Mainen, Z. F., and Sejnowski, T. J. (1996). Influence of dendritic structure on firing pattern in model neocortical neurons. *Nature* 382, 363-366.
- Major, G., Evans, J. D., and Jack, J. J. (1993). Solutions for transients in arbitrarily branching cables: I. Voltage recording with a somatic shunt. *Biophys J* 65, 423-449.
- Nitzan, R., Segev, I., and Yarom, Y. (1990). Voltage behavior along the irregular dendritic structure of morphologically and physiologically characterized vagal motoneurons in the guinea pig. *J Neurophysiol* 63, 333-346.
- Pinsky, P. F., and Rinzel, J. (1994). Intrinsic and network rhythmogenesis in a reduced Traub model for CA3 neurons. *J Comput Neurosci* 1, 39-60.
- Rall, W. (1957). Membrane time constant of motoneurons. *Science* 126, 454.
- Rall, W. (1959). Branching dendritic trees and motoneuron membrane resistivity. *Exp Neurol* 1, 491-527.
- Rall, W. (1969). Time constants and electrotonic length of membrane cylinders and neurons. *Biophys J* 9, 1483-1508.

Rall, W., and Rinzel, J. (1973). Branch input resistance and steady attenuation for input to one branch of a dendritic neuron model. *Biophys J* 13, 648-687.

Rall, W., Segev, I., Rinzel, J., and Shepherd, G. M. (1995). The theoretical foundation of dendritic function : selected papers of Wilfrid Rall with commentaries (Cambridge, Mass. ; London: MIT Press).

Rinzel, J., and Ermentrout, B. (1998). Analysis of neural excitability and oscillations, In *Methods in neuronal modeling : from ions to networks*, C. Koch, and I. Segev, eds. (Cambridge, Mass.: MIT Press), pp. 251-291.

Rinzel, J., and Rall, W. (1974). Transient response in a dendritic neuron model for current injected at one branch. *Biophys J* 14, 759-790.

Rose, P. K., and Cushing, S. (2004). Relationship between morphoelectrotonic properties of motoneuron dendrites and their trajectory. *J Comp Neurol* 473, 562-581.

Saltelli, A. (2004). *Sensitivity analysis in practice : a guide to assessing scientific models* (Hoboken, NJ: Wiley).

Schoenen, J. (1982). Dendritic organization of the human spinal cord: the motoneurons. *J Comp Neurol* 211, 226-247.

Segev, I., Fleshman, J. W., Jr., and Burke, R. E. (1990). Computer simulation of group Ia EPSPs using morphologically realistic models of cat alpha-motoneurons. *J Neurophysiol* 64, 648-660.

Thurbon, D., Luscher, H. R., Hofstetter, T., and Redman, S. J. (1998). Passive electrical properties of ventral horn neurons in rat spinal cord slices. *J Neurophysiol* 80, 2485-2502.

Williams, S. R., and Mitchell, S. J. (2008). Direct measurement of somatic voltage clamp errors in central neurons. *Nat Neurosci* 11, 790-798.

Yakovenko, S., Mushahwar, V., VanderHorst, V., Holstege, G., and Prochazka, A. (2002). Spatiotemporal activation of lumbosacral motoneurons in the locomotor step cycle. *J Neurophysiol* 87, 1542-1553.

Zengel, J. E., Reid, S. A., Sypert, G. W., and Munson, J. B. (1985). Membrane electrical properties and prediction of motor-unit type of medial gastrocnemius motoneurons in the cat. *J Neurophysiol* 53, 1323-1344.

CHAPTER 3: Asymmetric electrotonic coupling between the soma and dendrites alters the bistable firing behaviour of reduced models[§]

Glossary

| | |
|-----------------|---------------------------------------------------|
| DDVA | Direction Dependant Voltage Attenuation |
| A _{SD} | voltage Attenuation factor from Soma to Dendrites |
| A _{DS} | voltage Attenuation factor from Dendrites to Soma |
| PIC | Persistent Inward Current |
| CI | Characteristic Index |
| TTP | Time To onset of Plateau potential |
| TES | Time to End of Somatic spiking |
| DSF | Difference in Spiking Frequency |

3.1 INTRODUCTION

The coexistence of two stable states for a given stimulus (*i.e.* bistable behaviour) has been described in many areas of the central nervous system as a fundamental neuronal process for sustaining persistent activity or phasic rhythmic firing (Brunel, 2003; Egorov et al., 2002; Hounsgaard and Kiehn, 1989; Li et al., 2006; Llinas and Sugimori, 1980; Steriade, 1999). For example, in motor neurons bistable behaviour has been implicated in control of posture (Eken and Kiehn,

[§] *A version of this chapter has been published online.*
Kim H and Jones KE, *J Comput Neurosci* DOI 10.1007/s10827-10010-10284-x, 2010.

1989; Kiehn and Eken, 1997), gain control of firing rate (Kiehn, 1991; Lee and Heckman, 2000), and involuntary muscle contraction after spinal cord injury (Bennett et al., 2001; Li and Bennett, 2003). The bistable firing pattern has been identified in various species using ascending and descending ramp (also called triangular) current stimulation and measuring: 1) the counter-clockwise hysteresis in the frequency-current relationship and 2) sustained spiking below the current threshold on the downward-phase of the stimulus waveform (Bennett et al., 2001; Hounsgaard et al., 1988a; Lee and Heckman, 1998a; Lee and Heckman, 1998b). Using these criteria, several different types of firing patterns have been observed in sacral (Type I-IV in Bennett et al., 2001) and lumbar spinal motor neurons (partially and fully bistable in Lee and Heckman, 1998b).

These firing patterns of motor neurons depend on the density, type and location of voltage-gated ion channels that generate persistent inward current (PIC) (Lee and Heckman, 1996; Li and Bennett, 2003; Schwindt and Crill, 1980c). Although the full details of the location of PIC channels are still emerging (Ballou et al., 2006), it has been suggested that the calcium conducting channels are non-uniformly distributed and concentrated in the dendrites. The evidence for this assertion includes experimental (Ballou et al., 2006; Bennett et al., 1998; Carlin et al., 2000a; Hounsgaard and Kiehn, 1993; Lee and Heckman, 1996; Simon et al., 2003), and computational studies (Booth and Rinzel, 1995; Booth et al., 1997; Carlin et al., 2000b; Elbasiouny et al., 2005; Grande et al., 2007; Gutman, 1991; Jones KE, 2000).

To understand how the calcium dependent PICs interact with the firing behaviour in a complex dendritic system, it is first necessary to characterize signal propagation properties between the soma and the dendrites (Rall and Rinzel, 1973; Rinzel and Rall, 1974). After this characterization is complete, the influence of signal propagation on neuronal output behaviour can be evaluated. We recently investigated the first issue using anatomically reconstructed motor neuron models (Kim et al., 2009). In that study, we characterized steady-state

electrotonic coupling between the soma and a specific dendritic location using the empirically determined direction-dependant voltage attenuation (DDVA). We derived an analytical solution using DDVA to create reduced models that retained signal propagation properties of the anatomically reconstructed models. We hypothesized that the asymmetric coupling responsible for DDVA would change the bistable firing dynamics of reduced models that separate PIC channels for generating plateau potentials in the dendrite from ion channels for spiking in the soma.

The second issue, the influence of asymmetric coupling (*i.e.* DDVA) on motor neuron bistability, has not been explicitly investigated, probably due to the lack of a suitable theoretical framework to deal with the complex geometry of the dendrites along with the cable properties (Cullheim et al., 1987a; Cullheim et al., 1987b; Donohue and Ascoli, 2008). Modeling approaches that use anatomically reconstructed dendrites implicitly include physiological asymmetric coupling properties (Bui et al., 2006; Elbasiouny et al., 2005; Mainen and Sejnowski, 1996). However, to determine the implications of asymmetric coupling for bistability and establish mathematical generalizations using analysis, the coupling parameters must be amenable to the explicit manipulation that is typical of reduced modeling approaches. Current reduced modeling approaches have discovered many fundamental insights about the dynamical behaviour of neurons and the influence of coupling parameters (Booth and Rinzel, 1995; Doiron et al., 2002; Mainen and Sejnowski, 1996; Pinsky and Rinzel, 1994). These models however, did not explicitly derive their coupling parameters from the anatomy and biophysical properties of reconstructed dendrites, instead choosing specific mathematical parameters from their system equations that could best represent physiological coupling properties.

In this study, we evaluated the influence of asymmetric coupling using our new reduced modeling approach. Active membrane mechanisms were added to our passive reduced model using the Morris-Lecar equations (equation (1-7)) from a

previous two-compartment motor neuron model (Booth and Rinzel, 1995). By comparing our results with asymmetric coupling to the previous model with symmetric coupling we demonstrated the influence of the DDVA parameters on the nonlinear dynamical behaviour. We first used engineering control theory to do input/output analysis of the passive models. This analysis laid the groundwork for insights into the correlation of DDVA properties to dendritic input resistance and predictions for subsequent numerical simulations that explored bistable firing behaviour. We showed how asymmetric coupling of the soma and the dendrites affected key parameters like input resistance that have significant effects on the excitability of the active system. Finally, we assessed how bistable behaviour of the new reduced model compared with physiological DDVA properties of anatomically-reconstructed motor neuron models.

3.2 METHODS

3.2.1 *Symmetric and asymmetric reduced models*

The reduced model used in the study was based on the physiological two-compartment framework that captures direction-dependant voltage attenuation (DDVA) properties and includes the minimum essential biophysical properties of input resistance and time constant in Chapter 2 (Kim et al., 2009). Figure 3-1 shows the schematic diagram of the physiological two-compartment model. Applying Kirchhoff's current law to Figure 3-1 with steady-state conditions, the system equations of the passive two-compartment models are,

$$I_S = G_{m,S} \cdot V_S + \frac{G_C}{p} (V_S - V_D) \quad (3-1)$$

$$I_D = G_{m,D} \cdot V_D + \frac{G_C}{1-p} (V_D - V_S) \quad (3-2)$$

where I_S and I_D are current inputs to somatic and dendritic compartment normalized by the corresponding compartment surface area. V_S and V_D are membrane potential deviations from the resting potential in somatic and dendritic compartment. $G_{m,S}$ and $G_{m,D}$ are specific membrane conductances at the soma and dendrite. G_C is the coupling conductance normalized by the total surface area of the cell. p is the morphological factor defined by the ratio of the somatic surface area to the total surface area at the specific path length from the soma. These parameters are dimensionless.

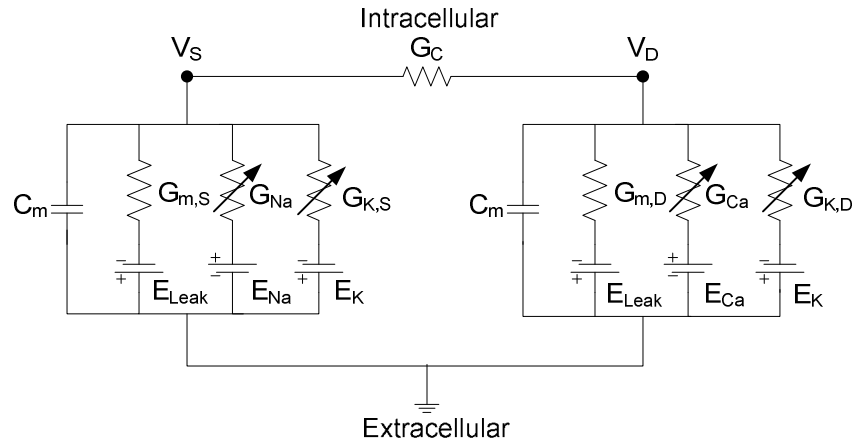


Figure 3-1. Schematic diagram of the asymmetrically coupled models. The somatic (left) and dendritic (right) compartments are connected by a coupling conductance, G_C . A key difference between previous and our model is that G_C is determined analytically and is not a free parameter. Active membrane properties, based on the dimensionless Morris-Lecar equations, are embedded in both compartments. Maximum conductance densities: G_{Na} for sodium current, $G_{K,S}$ for somatic potassium current, G_{Ca} for calcium current and $G_{K,D}$ for dendritic potassium current. Reversal potentials: E_{Na} , E_{Ca} , E_K , and E_{Leak} . Passive membrane properties: C_m specific membrane capacitance, G_C specific coupling conductance, $G_{m,S}$ specific membrane conductance in the soma, and $G_{m,D}$ specific membrane conductance in the dendrite. V_S and V_D are membrane potentials in the somatic and dendritic compartments, respectively.

Electrotonic coupling structure between the soma and dendrites was parameterized with two DDVA properties: voltage attenuation from the soma to a specified location on a dendrite (A_{SD}) and from a specified location on a dendrite to the soma (A_{DS}). Two types of passive reduced model are generated by this two-compartment framework: symmetric ($A_{SD}=A_{DS}$) vs. asymmetric ($A_{SD}\neq A_{DS}$) models.

To generate a symmetric model it is sufficient to specify uniform membrane conductance (*i.e.* $G_m=G_{m,D}=G_{m,S}$) and equal surface area for both compartments (*i.e.* $p=0.5$). This becomes obvious if G_m and p are substituted into the following equations for the DDVA parameters derived from system equations (3-1) and (3-2). Note that coupling symmetry is maintained regardless of G_C .

$$A_{SD} = \frac{V_D}{V_S} = \frac{G_C}{G_C + G_{m,D} \cdot (1 - p)} \quad (3-3)$$

$$A_{DS} = \frac{V_S}{V_D} = \frac{G_C}{G_C + G_{m,S} \cdot p} \quad (3-4)$$

The details of the derivation for equations (3-3) & (3-4) are in Chapter 2 (Kim et al., 2009). The nonlinear dynamics of the symmetric model with Morris-Lecar dynamics has been fully characterized as a function of the coupling parameter (G_C) (Booth and Rinzel, 1995).

To generate an asymmetric model we follow the procedures outlined in Chapter 2 (Kim et al., 2009). First an anatomically reconstructed neuron with measured values of input resistance (R_N) and membrane time constant (τ_m) is chosen. Next, a distance of separation between the soma and a location on the dendrites is chosen, D_{path} . The choice of D_{path} determines the values for A_{SD} , A_{DS} and p for an anatomically reconstructed cat spinal motor neuron. For example, by choosing $D_{path} = 300 \mu\text{m}$ the default values were $A_{SD} = 0.89$, $A_{DS} = 0.26$ and $p = 0.168$. Using these values for A_{SD} , A_{DS} and p together with R_N and τ_m we solve for the unknown cable parameters in equations (3-1) & (3-2), *i.e.* $G_{m,D}$, $G_{m,S}$, and G_C .

Table 3-1 shows the details of biophysical properties and standard parameter values assigned to the default asymmetric model. Note that the resulting non-uniform passive properties in the soma and dendrites should not be interpreted in the same way as the specific resistivity of a patch of membrane in the anatomically reconstructed motor neuron models.

After including Morris-Lecar dynamics in the asymmetric model, the nonlinear dynamics was investigated as a function of the DDVA parameters A_{SD} and A_{DS} . The effects of variations in DDVA parameters were evaluated on the DDVA parameter space ($0.01 \leq A_{SD} \leq 0.99$, $0.01 \leq A_{DS} \leq 0.99$).

Table 3-1. Standard parameter values for the asymmetric model

| Morphology | Electrotonics | Membrane parameters | | |
|-------------|---------------------------------------------------------------------------|----------------------------------------------------------------------------------------|----------------------------------------------------------------------------------------------------------------------------------------------------------------------|----------------------------------------------------------------------------------------------------------------------------------------------------------------|
| | | Passive | Active | |
| | | | Soma | Dendrites |
| $p = 0.168$ | $r_{N,S} = 0.19$ $\tau_m = 10.4$ $A_{SD} = 0.89$ $A_{DS} = 0.26$ | $G_{m,S} = 5.1$ $G_{m,D} = 0.04$ $G_C = 0.3$ $C_m = 3.2$ $E_{Leak} = -0.5$ | $G_{Na} = 11.0$ $E_{Na} = 1.0$ $G_{K,S} = 14.0$ $E_K = -0.7$ $v_{1S} = -0.01$ $v_{2S} = 0.15$ $v_{3S} = -0.04$ $v_{4S} = 0.1$ $\phi_S = 0.2$ | $G_{Ca} = 0.89$ $E_{Ca} = 1.0$ $G_{K,D} = 0.44$ $E_K = -0.7$ $v_{1D} = 0.05$ $v_{2D} = 0.1$ $v_{3D} = 0$ $v_{4D} = 0.1$ $\phi_D = 0.2$ |

Morphological factor, p for the ratio of somatic to total surface area; Electrotonics, $r_{N,S}$ for input resistance normalized with somatic surface area, τ_m for system time constant, A_{SD} and A_{DS} for direction-dependant voltage attenuation properties; Passive membrane parameters, $G_{m,S}$, $G_{m,D}$, G_C and C_m in Fig. 3-1; Active membrane parameters defined based on Morris-Lecar model as in Appendix; p and electrotonics of the asymmetric model was measured from an anatomically reconstructed motor neuron (V1 in Table 2-1 in Chapter 2 (Kim et al., 2009)), in turn passive membrane properties were calculated using inverse equations (Equation (2-15)a-d in Chapter 2 (Kim et al., 2009)).

3.2.2 Active dynamics of models: bistability

Active membrane properties, based on the Morris-Lecar model (Morris and Lecar, 1981), were added to each compartment as in a previous study (Booth and Rinzel, 1995). The default parameters for the Morris-Lecar ion channel models established by Booth and Rinzel did not generate bistable firing behaviour in the default asymmetric model, due to the discrepancy in electrotonical ($r_{N,S}$, τ_m , A_{SD} and A_{DS} in Table 3-1) and morphological (p in Table 3-1) properties. To generate bistable firing behaviour in the asymmetric model, the maximum conductance of all ion channels was changed as well as the parameter related to the slope of the steady-state activation variable of the dendritic calcium channel (V_{2D} in Table 3-1). The changes in the parameters of the Morris-Lecar equations for the asymmetric model were uniquely determined by fitting to the nonlinear phase-nullclines of the symmetric model. This method of fitting results in the same mechanisms underlying the nonlinear dynamics of the symmetric and asymmetric model: a Hopf bifurcation at the onset of somatic spiking and a saddle-node bifurcation at the onset of the dendritic plateau potential. Bifurcation analysis demonstrating these dynamics is presented in Results (see (a1) & (b1) in Figure 3-3).

We used triangular current stimulation to the soma as the bifurcation parameter to determine if bistable firing patterns resulted as the DDVA parameters (A_{SD} and A_{DS}) were changed from the default values. We defined three characteristic indexes (CIs) to determine the presence of bistability:

- Time To onset of Plateau potential (TTP): This index measures the latency between the first somatic action potential and the onset of the dendritic plateau potential. If this value is positive, the onset of the plateau potential follows the first somatic spike. If the value is negative, the plateau potential precedes somatic spiking.
- Time to End of somatic Spiking (TES): This index measures the duration of spiking during the downward phase of current

stimulation relative to the current threshold from the upward phase. If this value is positive, somatic spiking persists past the spiking threshold on the upward phase. If the value is negative, spiking stops before reaching the threshold determined on the upward phase of stimulation.

- **Difference in Spiking Frequency (DSF):** This index measures the difference in instantaneous spiking frequency at the current threshold determined on the upward phase of stimulation. If this value is positive, the firing frequency is greater on the downward phase and indicates counter-clockwise frequency hysteresis. If this value is negative, spiking frequency on the downward phase is less or repetitive spiking has ceased.

All three indexes are illustrated in Figure 3-2. Bistable firing behaviour was operationally defined when all three indexes had positive values. Typically, a positive value of TTP was associated with the concurrent existence of dendritic plateau-off and -on states at a particular steady-state current. This is a criterion used in a previous theoretical study (Booth and Rinzel, 1995). Experimental studies of bistability in vertebrate motor neurons have classified responses during triangular current clamp conditions as fully/partially bistable (Lee and Heckman, 1998b) or as Types I-IV (Cotel et al., 2009; Li and Bennett, 2003). A fully bistable neuron has a positive TES and DSF while a partially bistable neuron has a TES close to zero and a small negative DSF. A Type I neuron would have a TES and DSF close to zero. A Type II neuron exhibits adaptation of firing rate that would result in a negative TES and DSF. A Type III neuron would exhibit a positive TES but minimal DSF. The Type IV neuron, which is equivalent to the fully bistable cell, would have a positive TES and DSF. Therefore our definition of bistable behaviour identified instances of the model where the behaviour was fully bistable or Type IV and the onset of the plateau follows initiation of somatic spiking.

Numerical bifurcation analysis⁸ of the asymmetric model was first conducted for three representative coupling structures: physiological ($A_{SD} \gg A_{DS}$), symmetric ($A_{SD} = A_{DS}$), and non-physiological ($A_{SD} \ll A_{DS}$). Then simulations⁹ were done with the asymmetric model keeping the active properties constant and varying the manipulated parameters (A_{SD} and A_{DS}). We evaluated the three characteristic indexes at each location of the DDVA plane, where the location (x, y) is defined by the value (A_{DS}, A_{SD}) . The values of individual characteristic indexes were calculated to determine areas on the DDVA plane where the values switched signs (*i.e.* from positive to negative) and the magnitude of the values. The solution space for bistability on the DDVA domain was defined as the area of intersection where all three characteristic indexes were positive. This analysis is commonly referred to as the constraints inference method with three constraints ($TTP > 0$, $TES > 0$ and $DSF > 0$) (Dechter, 2003).

3.2.3 Comparison to anatomical models

While the full DDVA domain is of theoretical interest for evaluating the effects of asymmetric coupling between the two compartments, the anatomy of motor neuron dendrites restrict possible values of A_{SD} and A_{DS} to a sub region of the DDVA domain. To determine the anatomically relevant area of the DDVA domain the values of A_{SD} and A_{DS} were calculated at different distances (*i.e.* D_{path}) from the soma as previously reported in Chapter 2 (Kim et al., 2009). The region of the DDVA domain defined by motor neuron anatomy and passive properties was superimposed on the solution space defined by the three characteristic indexes.

3.3 RESULTS

⁸ The bifurcation analysis was conducted using XPPAUTO software (Ermentrout, 2002).

⁹ Gear method was used for solving differential equations governing nonlinear dynamics of reduced models (Appendix for chapter 3).

To determine the effect of DDVA on the nonlinear firing patterns of the reduced models we combined a theoretical approach, with numerical simulations. The goal of the theoretical analysis was to develop analytical equations for indirect measures of excitability, such as input resistance, and the relationship to the passive steady-state attenuation properties A_{SD} and A_{DS} . The analytical predictions were used to interpret the later numerical simulations. The goal of the numerical simulations was to determine how the passive electrotonic nature of DDVA influenced the highly nonlinear properties of the active two-compartment models. The results showed that DDVA has a strong influence on the nonlinear firing behaviour.

3.3.1 Theory: passive input-output properties with respect to DDVA

Input resistances at both compartments, and a multiple current-input and voltage-output relationship were formulated as a function of DDVA for symmetric and asymmetric coupling between points localized on the soma and dendrite. Changes of electrotonic structure by varying DDVA properties lead to significant effects on passive dynamics and thereby changed the excitability of the dendritic compartment. This showed that dendritic excitability was affected by DDVA and therefore might have a significant influence on the activation of the plateau potential in numerical simulations. The major difference between symmetric and asymmetric coupling of the soma and dendrite was that input resistance was the same for both compartments in the symmetric case but could have different values in the asymmetric case.

3.3.1.1 Input resistance at dendrites

It is well known that input resistance in dendrites increases as a function of distance from the soma (Jaffe and Carnevale, 1999; Rall and Rinzel, 1973). We have shown in Chapter 2 that a two-compartment model based on an implicit approach captures changes in dendritic input resistance with distance from the soma when compared to the physiological properties of motor neuron dendrites

(Kim et al., 2009). It is not known how DDVA in general is related to changes in dendritic input resistance and whether dendritic input resistance is different for symmetric versus asymmetric coupled models.

From the governing equations (3-1) & (3-2), the input resistance (V_D/I_D) as a function of the passive cable properties of the model (Figure 3-1) is,

$$r_{N,D} = \frac{V_D}{I_D} = \left(G_{m,D} + \frac{p \cdot G_C \cdot G_{m,S}}{(1-p) \cdot (G_C + p \cdot G_{m,S})} \right)^{-1} \quad (3-5)$$

where $r_{N,D}$ is the input resistance at dendritic compartment normalized by dendritic surface area.

By substituting the inverse equations for cable properties ($G_{m,D}$, $G_{m,S}$ and G_C from Kim et al. 2009) into Equation (3-5), we rearranged the equation to give the ratio between somatic and dendritic input resistance,

$$\frac{r_{N,D}}{r_{N,S}} = \frac{1-p}{p} \cdot \frac{A_{SD}}{A_{DS}} \quad (3-6)$$

where $r_{N,S}$ is the input resistance at somatic compartment normalized by somatic surface area and A_{SD} and A_{DS} are the DDVA properties in peripheral and central directions, respectively.

To get the expression for the absolute value of input resistance in the dendrite as a function of the DDVA properties we divided by the corresponding surface area to get,

$$R_{N,D} = \frac{A_{SD}}{A_{DS}} \cdot R_{N,S} \quad (3-7)$$

where $R_{N,D}$ and $R_{N,S}$ are the absolute values for dendritic and somatic input resistance. Equation (3-7) shows that dendritic input resistance is directly related to DDVA by the ratio of asymmetry in the coupling of the two compartments.

For the special case of symmetric coupling, *i.e.* when voltage attenuation is the same for both directions ($A_{SD}=A_{DS}$), Equation (3-7) simplifies to,

$$R_{N,D} = R_{N,S} \quad (3-8)$$

These results showed that when two compartment models are coupled asymmetrically the dendritic input resistance increases in proportion to A_{SD} and inversely to A_{DS} . In our previous method for calculating a reduced two-compartment model from anatomically reconstructed dendrites, the input resistance of the soma remains constant and the DDVA properties vary as a function of distance from the soma (Kim et al., 2009). We confirmed that $R_{N,D}$ calculated by Equation (3-8), as a function of distance from the soma, matched the physiological values for reconstructed motor neuron dendrites (not shown). The striking difference between asymmetric and symmetric coupling was that in the latter case, $R_{N,D}$ is identical to $R_{N,S}$. Furthermore $R_{N,S}$ in symmetric coupling is not constant but varies according to the degree of voltage attenuation that is manipulated by G_C ; decrease in $R_{N,S}$ as G_C increases (see Equation (2-9) in Chapter 2 (Kim et al., 2009) with standard parameters of symmetric coupling, $G_m=G_{m,S}=G_{m,D}=0.5$ and $p=0.5$). The input resistance of the dendritic compartment is an important determinant of excitability because the greater the resistance the less current needed to activate the voltage-dependent plateau generating channels. This result implies that dendritic excitability in simulations with the active asymmetric model will be strongly affected by the DDVA properties and may have a significant influence on firing behaviour.

3.3.1.2 Multiple inputs and single output relationship

$(I_S + I_D \rightarrow \square \rightarrow V_D)$: To determine the influence of DDVA properties on changes in dendritic membrane potential as a function of both a somatic (I_S) and dendritic (I_D) current source we derived a function for $V/\Sigma I$ from the linear system equations. This analysis approximates the experimental conditions with an electrode in the soma and net dendritic current from intrinsic and/or synaptic sources.

According to the superposition principle, the total deviation of dendritic membrane potential (V_D) from the resting state by two current sources (I_S and I_D) is equal to the sum of the dendritic voltage changes contributed by each I_S and I_D respectively. Using the definitions of DDVA and input resistance, the transfer resistance representing the dendritic voltage change ($V_D(I_S)$) by I_S is first derived,

$$\frac{V_D(I_S)}{I_S} = \frac{V_D(I_S)}{V_S(I_S)} \cdot \frac{V_S(I_S)}{I_S} = A_{SD} \cdot r_{N,S} \quad (3-9)$$

The second relation of the dendritic voltage change ($V_D(I_D)$) to I_D is equal to Equation (3-5),

$$\frac{V_D(I_D)}{I_D} = r_{N,D} \quad (3-10)$$

Dividing Equation (3-9) & (3-10) by the corresponding surface area to convert normalized input resistances ($r_{N,D}$ and $r_{N,S}$) to absolute values and summing, the combined relationship ($I_S + I_D \rightarrow \square \rightarrow V_D$) is,

$$V_D = R_{N,S} \cdot A_{SD} \cdot I_S + R_{N,D} \cdot I_D \quad (3-11)$$

In the symmetric case, the equation can be further simplified because input resistance is the same for both compartments (*i.e.* $R_N = R_{N,S} = R_{N,D}$ in Equation (3-8))

and the voltage attenuation is the same for both directions (*i.e.* $VA=A_{SD}=A_{DS}$). Similar to the asymmetric coupling, potential deviation from resting membrane potential for symmetric coupling case is,

$$V_D = R_N (VA \cdot I_S + I_D) \quad (3-12)$$

where I_D and I_S in Equation (3-11) and (3-12) are absolute current stimulation to the dendritic and somatic compartments.

Since $R_{N,D}$ depends on $R_{N,S}$ and DDVA parameters (Equation (3-7)), Equation (3-11) should be rearranged as a function of independent variables,

$$V_D = R_{N,S} \left(\frac{A_{SD}}{A_{DS}} \cdot I_D + A_{SD} \cdot I_S \right) \quad (3-13)$$

While membrane potential at dendrites (V_D) can be influenced by both DDVA properties for asymmetric coupling, V_D for symmetric coupling in Equation (3-12) varies depending on a single voltage attenuation properties (VA in Equation (3-12)) for both directions as expected.

In the context of experimental conditions for investigating the bistability of motor neurons, the depolarization of dendritic membrane potential is caused by excitatory current stimulation at the soma (I_S) as well as net inward current from membrane mechanisms including voltage- and ligand-dependant conductances in the dendrites (I_D). Equation (3-13) supports our prediction that the larger A_{SD} the faster onset of the plateau potential because V_D depolarization increases in proportion with contributions from both currents (I_S and I_D), whereas the larger A_{DS} the slower onset of the plateau potential by inversely weighting the contribution of only one current (I_D). It is worth noting that the bistable firing behaviour associated with the late onset of plateau potential may be more sensitive to changes in A_{SD} than A_{DS} .

3.3.2 *Bistability of asymmetric model*

To determine if the asymmetric model produced bistable firing similar to the symmetric model we evaluated the response to triangular and current pulse inputs (Figure 3-2). Both current input protocols have been used extensively in experimental and computational studies of motor neuron bistability (Booth and Rinzel, 1995; Hounsgaard et al., 1988a; Hounsgaard and Kiehn, 1989).

Figure 3-2(a) illustrates the response of the asymmetric model to triangular current injection. As the current stimulation increased, V_S transitioned from a depolarized stable state to a regular firing state at the current threshold followed by a jump to a higher firing frequency. The jump to the higher firing frequency coincided with the transition of V_D to a plateau potential. All three characteristic indexes (CIs) used to define bistable firing were measured from the response to triangular current injection. Since somatic spiking preceded the dendritic plateau onset, TTP had a positive value. As the stimulation decreased toward the value of current threshold determined on the upward phase, the firing frequency remained elevated resulting in a positive DSF. As the current stimulation continued to decrease, the model continued to fire well past the current threshold resulting in a positive value for TES. Since all three CIs have positive values, by definition the response was considered bistable. The inset shows the frequency-current (f-I) relationship in response to the triangular current injection. This figure illustrates the hysteresis in firing frequency that characterizes bistable firing in motor neurons.

Figure 3-2(b) shows the switching behavior of the asymmetric model in response to short current pulse inputs to the soma. The model showed two types of bistable behavior: 1) between stable resting and repetitive firing (or stable limit cycle), 2) between two states of repetitive firing of different frequencies. The first bistable behaviour occurs at the points labeled b1-b2-b3. At the same current level (b1 = b3) the model can be switched between two states by short depolarizing (b2) and

hyperpolarizing current pulses. These values of current are superimposed on the f - I relationship from Figure 3-2(a) in the inset to show the correspondence in behaviour with the two current input protocols. The second bistable firing behaviour occurs at the points labeled $b1'$ - $b2'$ - $b3'$.

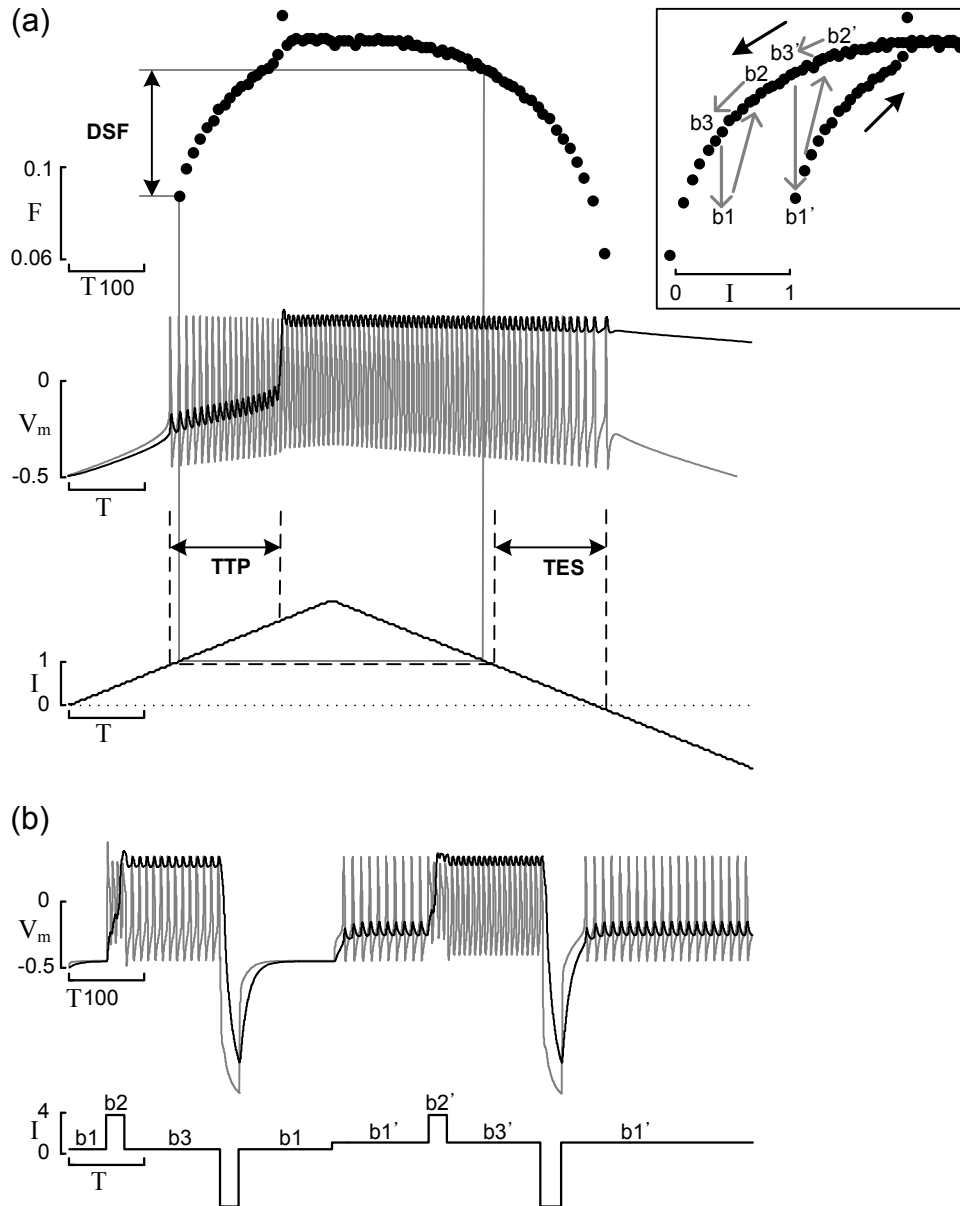


Figure 3-2. Bistable firing patterns of the asymmetric model. (a). Instantaneous firing frequency (F ; top graph), time courses of the somatic (gray) and dendritic (black) membrane potentials (V_m ; middle graph), and triangular current injection (I ; bottom graph) are plotted. F was measured as the reciprocal of somatic interspike interval. The inset shows counter-clockwise frequency hysteresis (F - I curve) indicated by the black arrows. The three characteristic indexes are marked directly on the graph and are as follows: Time To onset of Plateau potential (TTP), Difference in Spiking Frequency (DSF) and Time to End of somatic Spiking

(TES). (b). Time courses of membrane potential at the somatic (gray) and dendritic (black) compartment were plotted over brief depolarizing and hyperpolarizing current stimuli in the bottom. Small letters over the current stimulation profile are mapped to corresponding values in the inset, where transitions in frequency state were indicated by gray arrows. Bistability is present between points (b1, b3) and (b1', b3'). T is simulation time. Note that scale bars for F , V_m , I and T have different ranges.

3.3.3 DDVA dependency of firing patterns and bistability

3.3.3.1 Insights from bifurcation analysis

Figure 3-3 shows bifurcation diagrams of the asymmetric model for three representative coupling structures. Bistable firing of the asymmetric model was not present when physiological coupling ($A_{SD} \gg A_{DS}$) was changed either to the symmetric ($A_{SD} = A_{DS}$) or non-physiological ($A_{SD} \ll A_{DS}$) condition. This can be explained by the relationship between DDVA parameters and dendritic input resistance (Equation (3-7)). Dendritic input resistance can be visually estimated in Figure 3-3 (b1)-(b3) by slope of the stable fixed points starting from $I_{Soma} = -3$. The slope is greatest for the physiologic case (b1) and least for the non-physiologic case (b3). Subthreshold dendritic excitability, estimated by input resistance, of both symmetric and non-physiological cases was too low to activate the saddle-node bifurcations in the dendritic compartment.

In contrast to dendritic input resistance, somatic input resistance and rheobase (I_S at the Hopf bifurcation point in Fig. 3-3 a1-a3) were constant for the different DDVA values. Since somatic input resistance is an input parameter to the equations that solve for the cable parameters of the model, it is expected to be constant. However rheobase is not specified, so its stability indicated that this parameter might be independent of DDVA values. The results of this analysis indicate that the solution space for bistable firing behavior will be constrained to a range of DDVA values that give rise to sufficient input resistance at the dendritic compartment.

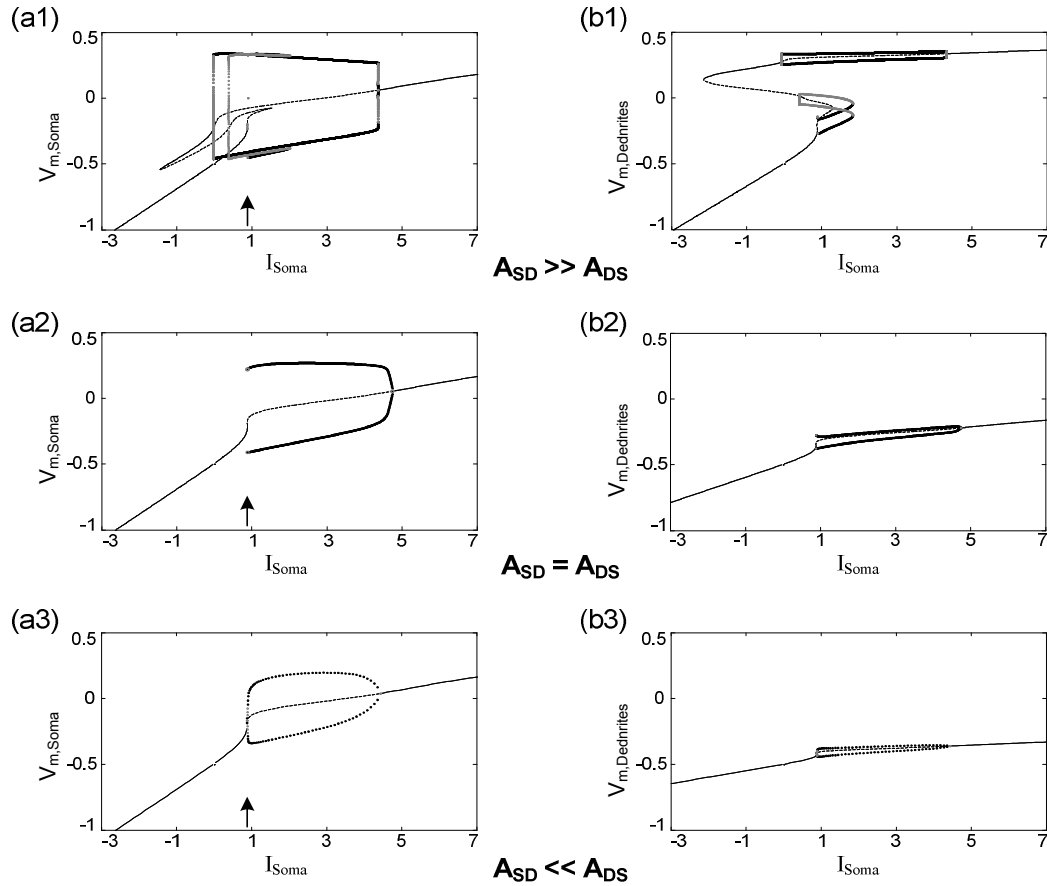


Figure 3-3. Bifurcation diagrams in the asymmetric model with physiological (a1 & b1, $A_{SD}(0.89) \gg A_{DS}(0.26)$), symmetric (a2 & b2, $A_{SD}(0.5) = A_{DS}(0.5)$), and non-physiological (a3 & b3, $A_{SD}(0.26) \ll A_{DS}(0.89)$) coupling. The left and right columns show changes of the membrane potential induced by the somatic current injection (I_{Soma}) in the somatic ($V_{m,Soma}$) and dendritic ($V_{m,Dendrites}$) compartment. For all figures, the stability of fixed points was indicated by black solid line for the stable state and black dashed line for the unstable state. Both stable (black filled circles) and unstable (gray filled circles) limit cycles were outlined with maximum and minimum amplitudes of membrane potential oscillation. Note that somatic spiking (indicated by arrows) was initiated at the same bifurcation point for all coupling structures, and the slope of the $V_{m,Soma} - I_{Soma}$ curve in the subthreshold region was constant, whereas the slope of the $V_{m,Dendrites} - I_{Soma}$ curve was decreased (*i.e.* $b1 > b2 > b3$), leading to the disappearance of saddle-node bifurcations in (b2) and (b3). Active membrane parameters in Table 3-1 were held

constant, but passive membrane parameters were systematically changed according to coupling structures: $G_{mS}=\{5.1, 3.5, 0.8\}$, $G_{mD}=\{0.04, 0.7, 3.5\}$, $C_m=\{3.2, 10.4, 29.7\}$, and $G_C=\{0.3, 0.59, 1.0\}$, where values in curly braces are in the order of physiological, symmetric and non-physiological case.

3.3.3.2 Characteristic index space

Figure 3-2 showed that all three CIs were positive in the asymmetric model at the default DDVA values of $A_{SD} = 0.89$ and $A_{DS} = 0.26$. To determine the relationship between DDVA and the three CIs, we systematically varied the DDVA values of the model. The resulting values for the three CIs across the full DDVA domain are shown in Figure 3-4.

The first row of Figure 3-4 shows the values of the TTP index, *i.e.* Time To onset of Plateau potential. There are distinct areas where TTP had positive values between about 50 and 250 (light areas). Across the full DDVA domain the largest area had TTP values of zero. This result is ambiguous as it could mean no plateau potential was generated or that the plateau potential occurred simultaneously with the onset of somatic spiking. The last column shows a cross section of TTP values along the A_{SD} axis. The cross section was chosen in this direction as it produced the highest gradient of change in TTP. TTP had a value of 0 for small A_{SD} , then abruptly increased to a peak value and then decreased with further increases in A_{SD} . The second row of Figure 3-4 shows the values of DSF, *i.e.* Difference in Spiking Frequency. The model had positive and negative values for DSF and distinct areas of positive values that were close to those associated with positive TTP values. In the case of DSF, the cross section with the largest gradient was along the A_{DS} axis. The third row of Figure 3-4 shows the distribution of values for TES, *i.e.* Time to End of somatic Spiking. The cross section along the highest gradient showed that TES increased linearly for a range of A_{DS} values then quickly decreased back towards zero.

Positive values for the three CIs are associated with bistable firing behaviour but the areas of positive values were different across the DDVA domain. No single CI was sufficient to distinguish the region of bistable solutions. Therefore the solution space for bistability on the DDVA domain was defined as the area of intersection where all three characteristic indexes were positive.

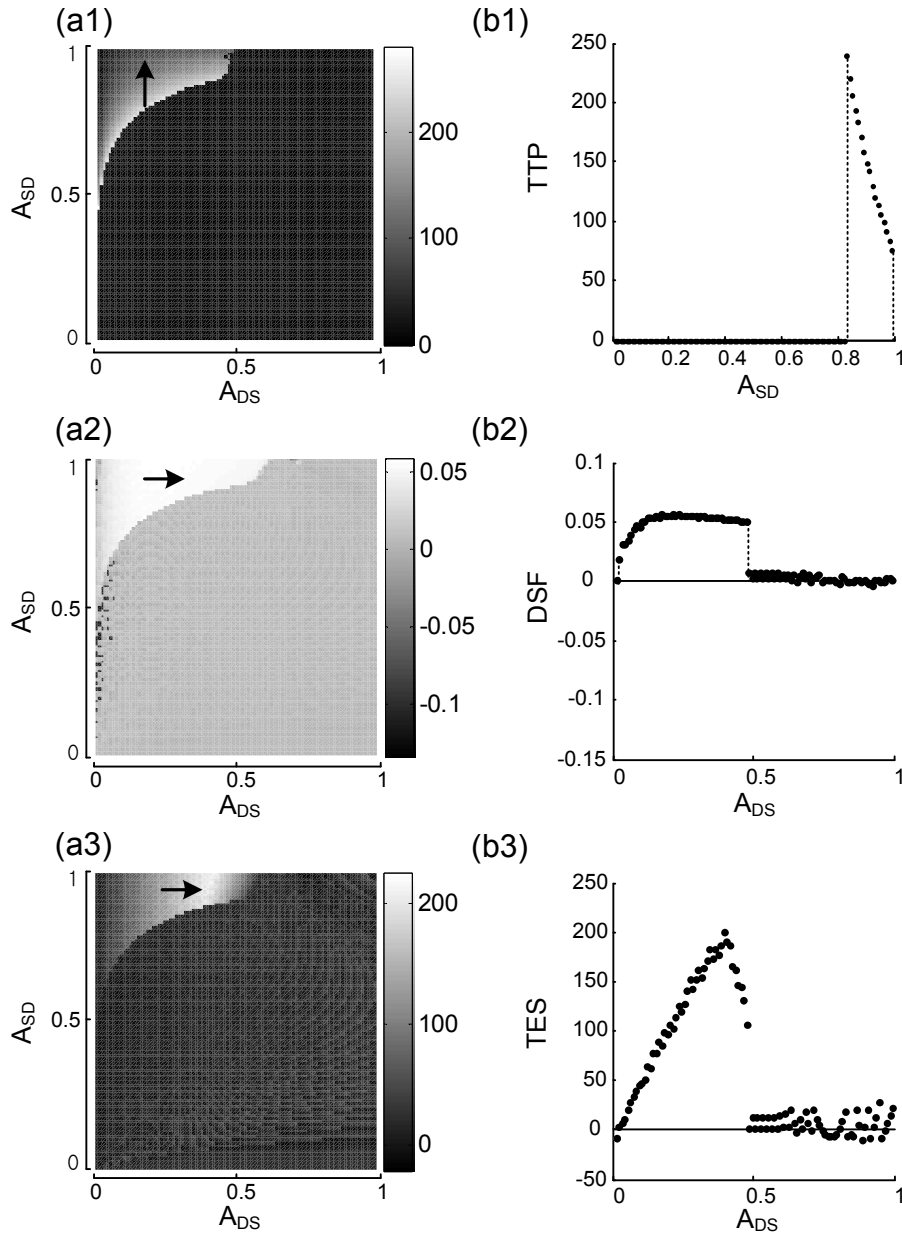


Figure 3-4. Distribution of characteristic indexes (CIs) for the asymmetric model on DDVA domain. (a1), (a2), and (a3) show the distribution of TTP, DSF, and TES respectively in gray scale, where higher values are white and lower values are black. Black arrows indicate the direction of the highest gradient in changes of each CI. (b). Cross section of CI values in column (a) along the gradient arrow passing to default DDVA values in Table 3-1: (b1) shows TTP values along the A_{SD} axis, (b2) shows DSF values along A_{DS} axis, and (b3) shows TES values

along the A_{DS} axis. The range of DDVA values producing positive CI values was indicated by black dashed lines in each panel of (b) column.

3.3.3.3 Firing patterns on DDVA domain

Having determined the changes in the CIs as a function of the DDVA properties we could unequivocally identify the bistable solution space. However, the firing patterns of the asymmetric model showed considerable variability within and outside the bistable solution space defined by the CIs. The differences in firing patterns across the DDVA domain are illustrated in Figures 3-5.

Four types of firing patterns were identified outside the bistable solution space, outlined by black dots at the upper left of the DDVA domain. One region of the DDVA domain was characterized by a lack of a plateau potential (Fig. 3-5 a1). In the model this region occupied the greatest area and extended to A_{SD} values of 0.8 and greater. A second region of the DDVA domain was characterized by plateau potentials that occurred before or simultaneously with the onset of somatic spiking (Fig. 3-5 a4). The borders of the remaining region are outlined in grey in Figure 3-5. This region had a variety of firing patterns including simultaneous spiking oscillations in both the soma and dendritic compartments (Fig. 3-5 a3). Another firing pattern within the grey bounded region showed plateau potentials that ended before somatic spiking stopped (Fig. 3-5 a2).

Firing patterns showed systematic changes within the bistable solutions space. Representative firing patterns along the boundary of the bistable solution space are shown at the bottom of Figure 3-5 (b1-b4). The TTP index increased as A_{SD} decreased between points b1 and b2. This is evident by a later acceleration of spiking frequency to the triangular current injection. Changes along the A_{DS} axis primarily effected frequency hysteresis characterized by DSF. This effect was clear in the model where a change of A_{DS} from 0.03 to 0.46 resulted in a doubling of DSF and greater hysteresis in the F-I curve (points b3 to b4).

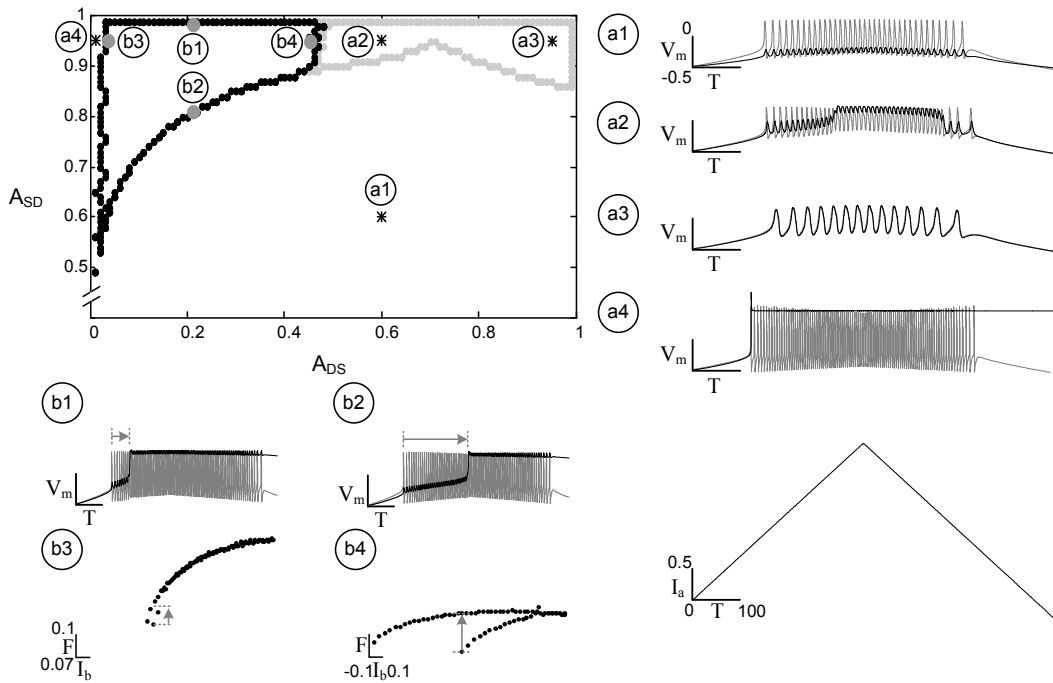


Figure 3-5. Firing patterns of the asymmetric model on DDVA domain. The DDVA plane is divided into four sub-regions for demonstrating the variety of firing patterns. The fully bistable firing patterns (*i.e.* $TTP > 0$, $DSF > 0$, $TES > 0$) occurred in the space outlined with black dots. The different types of non-bistable firing patterns were uncovered in three other sub-regions outside the bistable space: the upper-right space outlined with gray dots, the upper-left corner, and the lower-rest space. Representative firing behaviours on each sub-region were simulated with triangular current stimulation (I). a1 to a4 show the non-bistable firing patterns. b1 to b4 characterize the fully bistable firing patterns on the boundary of the bistable solution space: b1 & b2 for time courses of membrane potentials (V_m) and b3 & b4 for the frequency-current (F - I) relationship. The somatic and dendritic membrane potentials are indicated by the gray and black colors. Circled letters indicate the corresponding location on the DDVA plane. T is simulation time. Note that scale bars for V_m , I (*i.e.* I_a and I_b) and T have different ranges.

3.3.4 Distribution of physiological DDVA values

The results from Figure 3-5 showed that the asymmetric model had a large bistable solution space that extended well beyond the default values for DDVA ($A_{SD} = 0.89$ and $A_{DS} = 0.26$). The numerical simulations treated the two DDVA properties as independent, however in physiologically based models the DDVA properties are a function of distance from the soma, D_{path} in Chapter 2 (Kim et al., 2009). To determine the spatial relationship between bistable solutions of the two-compartment model and anatomically determined DDVA properties, we calculated DDVA as a function of distance from five reconstructed motor neurons. Figure 3-6 shows that the physiological DDVA values existed within the solution space of the asymmetric model. The distances where physiological DDVA values were within the bistable solution space ranged from $D_{path}=128 \mu\text{m}$ at $A_{DS}=0.46$ to $D_{path}=577 \mu\text{m}$ at $A_{DS}=0.03$. This range of distances matches the hypothesized location of calcium PIC channels (at least $300 - 500 \mu\text{m}$ away from the soma) estimated in experimental (Ballou et al., 2006; Heckman et al., 2003) and theoretical studies (Carlin et al., 2000b; Elbasiouny et al., 2005; Grande et al., 2007). The starting point for the DDVA properties of the asymmetric model was determined from anatomical model V1 at a distance of $300 \mu\text{m}$ from the soma. The DDVA values for all five anatomical models at $D_{path} = 300 \mu\text{m}$ are shown in Figure 3-6 (black dots within the solution space). All of these points were located inside the solution space of the reduced model.

The coincident spatial relationship between DDVA derived from anatomical models and bistable solutions of the asymmetric model suggests that the ability of the reduced models to retain physiological DDVA properties may be important for modeling nonlinear dynamical behaviour of motor neurons.

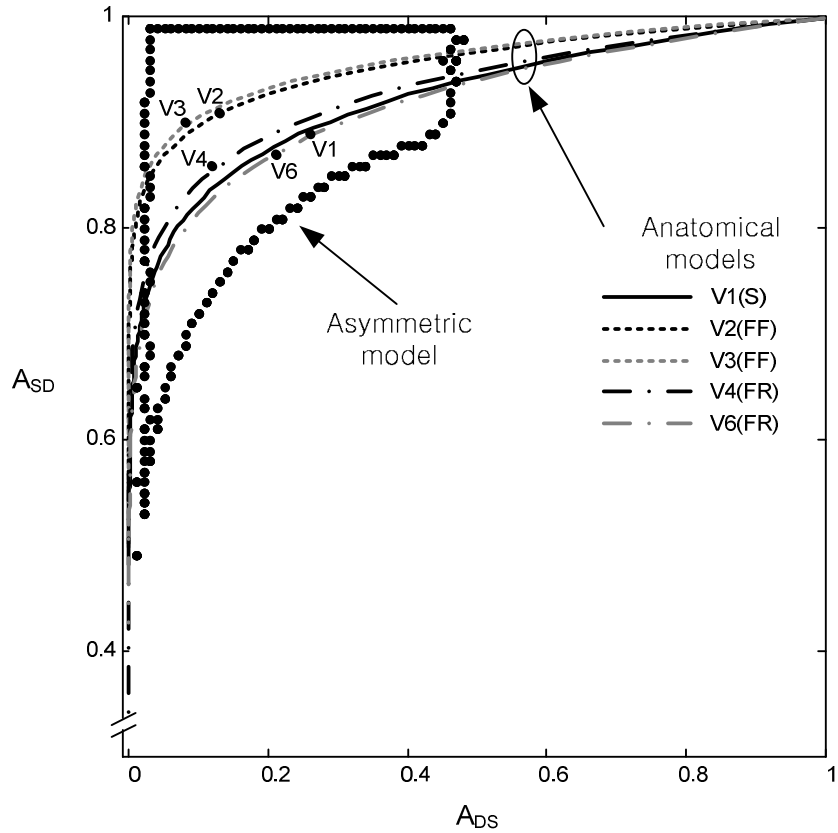


Figure 3-6. Coincidence of bistable solution space with physiological DDVA properties on DDVA domain. The bistable solution space of the asymmetric model is outlined by black dots on the DDVA plane. Physiological DDVA properties characterized from anatomically reconstructed motor neurons (V1-V4, V6 from Chapter 2 (Kim et al., 2009)) were distributed along the various types of lines on the same DDVA plane for determining the interception area. The lines of physiological DDVA values started from the point of $(A_{SD}=1, A_{DS}=1)$ and ended at the point of $(A_{SD}=0.33, A_{DS}=0)$ as a function of the distance from the soma up to maximum dendritic terminal. Black solid circles on the DDVA lines indicate default DDVA values calculated at the distance of $300 \mu\text{m}$ for different anatomical models, *e.g.* default DDVA properties for V1 are $A_{SD}=0.89$ and $A_{DS}=0.26$, which is also used for the default DDVA for the asymmetric model.

3.4 DISCUSSION

Our analytical and numerical results supported the hypothesis that asymmetric coupling between the soma and dendrites significantly influences the nonlinear dynamics of reduced two-compartment models. Furthermore the four physiological firing patterns reported for rat motor neurons (Bennett et al., 2001) were observed in the model as a function of coupling asymmetry. The results suggest that asymmetric coupling is an important concept in producing physiological firing patterns.

3.4.1 *Interaction of coupling parameters with firing patterns*

Input resistance of the soma and dendritic compartments was a major difference between symmetric and asymmetrically coupled models. Input resistance in the symmetric model was identical for both compartments and changed as a function of the coupling parameter (G_C). In contrast, input resistances of the two compartments in the asymmetric model were independent. The input resistance of the soma was constant while the dendritic input resistance changed as a function of the coupling parameters (A_{SD} , A_{DS}). The relative difference in input resistance between the soma and dendrites can be quantified by calculating the coupling index, the ratio of A_{SD} to A_{DS} in Equation (3-7). The coupling index equal to 1.0 (*i.e.* $A_{SD}=A_{DS}$) indicates that the input resistances of the soma and dendrites are identical. When the coupling index is greater than 1.0 (*i.e.* $A_{SD}>A_{DS}$) the input resistance in the dendrites is larger than in the soma, and vice versa (*i.e.* $A_{SD}<A_{DS}$). The differences in input resistance as a function of the coupling coefficient were associated with differences in the variety of firing patterns produced by the asymmetric model. Experimental observations have classified four types of firing behaviour in motor neurons based on frequency-current (F-I) relationship during triangular current stimulation (Bennett et al., 2001): Type I (linearly overlapping F-I relationship without self-sustained firing), Type II (clockwise F-I relationship with firing rate adaptation), Type III (linearly overlapping F-I relationship with

self-sustained firing), and Type IV (counterclockwise F-I relationship with self-sustained firing). The asymmetric model showed all four types of firing patterns (Figure 3-5). Type I and II firing patterns were present when the coupling index (or the difference in input resistances) was relatively small, *e.g.* $A_{SD}/A_{DS} = 1$ at a1 in Figure 3-5. Type III firing patterns occurred when the coupling index (or the difference in input resistances) was relatively large, *e.g.* $A_{SD}/A_{DS} = 95$ at a4 in Figure 3-5. Type IV firing patterns were generated when the coupling index (or the difference in input resistances) was moderate between above two firing cases, *e.g.* $A_{SD}/A_{DS} = 3.4$ at the default coupling parameter values ($A_{SD}=0.89$, $A_{DS}=0.26$).

3.4.2 *Importance of initial values of coupling parameters for bistable firing behaviour*

The coupling parameters in the asymmetric model were initialized with values within the physiological range ($A_{SD}=0.89$, $A_{DS}=0.26$), which are different from those in the symmetric model ($A_{SD}=A_{DS}=0.5$ in Booth & Rinzel 1995). By releasing the uniformity condition of the specific membrane resistivity in the symmetric model, we compared the bistable solutions between two models while varying coupling parameters (*i.e.* A_{SD} and A_{DS} for both models) on the DDVA domain. Our numerical results showed that fully bistable firing, *i.e.* type IV behaviour, in the asymmetric model occurred over a much larger area than in the symmetric model (Figure 3-7). Although this comparison is not without limitations, since the active membrane parameters and system properties of the two models were not identical, the difference in the solutions may in part be due to the fact that the asymmetric model had a larger dendritic input resistance when compared to the symmetric model with the same total surface area. Using Equation (3-7) and the initial values for the coupling parameters the input resistance for the dendrite was $(0.89/0.26)*1.9 = 6.5$ for the asymmetric and $(0.5/0.5)*4.3 = 4.3$ for the symmetric model. This result implies that the size of bistable solutions (*i.e.* robustness of bistability) for the asymmetric model may be

significantly influenced by the initial coupling values, which are directly associated with the excitability of the dendritic compartment (Equation (3-7)).

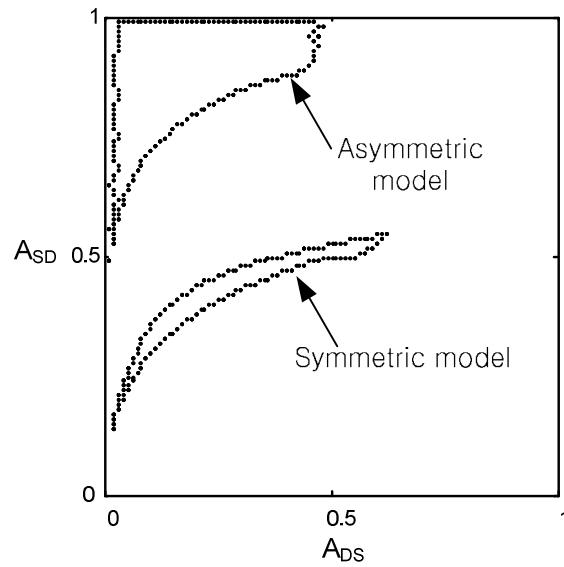


Figure 3-7. Variability of bistable solution space on DDVA domain. The size of the bistable solution space was different in the reduced models with different initial DDVA values. The lower outline of black dots shows the bistable solution space for the symmetric model with the default value of $A_{SD}=A_{DS}=0.5$. The upper outline of black dots shows the bistable solution space for the asymmetric model with the default value of $A_{SD}=0.89$ and $A_{DS}=0.26$.

3.4.3 Comparison with other studies

The relationship between input resistance at the dendrites and attenuation of synaptic potentials as they propagate toward the soma has been of interest because of the influence on spatial and temporal integration (Katz and Miledi, 1963; Rall and Rinzel, 1973; Rinzel and Rall, 1974). The nonlinear dynamic behavior driven by the activation of voltage-dependant membrane mechanisms in the dendrites is likely to be influenced by both directions of voltage attenuation (*i.e.* DDVA). Our analytical results showed that subthreshold depolarization of the dendritic membrane potential was a function of both DDVA properties (Equation (3-13)).

The practical insights into electrophysiological coupling between the soma and the dendrites have been previously reported using single input-single output (SISO) analysis and reduced abstract models based on two-port theory (*i.e.* π - and equivalent T-network) (Carnevale and Johnston, 1982; Jaffe and Carnevale, 1999). This analysis showed that electrophysiological coupling could be characterized by direction-dependant voltage/current attenuation and the direction-independent transfer resistance phenomenon. Given the relationship between input resistance and DDVA properties in Equation (3-7), the transfer resistances of the asymmetric model ($V_S/I_D = R_{N,S} \cdot A_{SD}$ and $V_D/I_S = R_{N,D} \cdot A_{DS}$ for each direction) were *symmetric* and the same as those derived for the T-network model (Jaffe and Carnevale, 1999). While the final form of the equations that we derived was not novel, this is the first analysis to derive these equations from a conductance based compartmental approach that is grounded in biophysical reality. Our result demonstrated the validity of the new modeling approach starting from fully reconstructed anatomical models in Chapter 2 (Kim et al., 2009) and being able to write the system of equations to retain both DDVA and transfer resistance coupling characteristics.

Gutmann (1991) used an ideal cable formalism to emphasize that electrotonic separation between the soma and current source was responsible for the N-shaped

current-voltage curve required to generate bistable behaviour of motor neurons. Booth and Rinzel (1995) used a theoretical coupling property (*i.e.* coupling conductance, G_C) to manipulate electrotonic separation in a two-compartment modeling framework. Using dynamic systems theory, they showed that bistable firing behaviour resulted when there was a simultaneous saddle-node bifurcation in the dendritic compartment and a stable limit cycle in the somatic compartment. They found that these necessary conditions for bistable firing happened for a small range of intermediate G_C values. Their results reinforced the conclusion that the ionic current underlying spiking in the soma and currents generating plateau potentials in the dendrites needed to be electrotonically separated. However neither of these two reduced modeling approaches provided a precise quantitative prediction about the physical distance of separation needed for bistable firing behaviour. Our two-compartment modeling framework provides this prediction, D_{path} . We used the physiological property of DDVA as the coupling parameters in the new reduced model. We found that bistable firing behaviour happened in a circumscribed region of the DDVA domain. Since D_{path} determines the DDVA parameters, we checked to see if this area was intersected by the DDVA values calculated across the range of D_{path} for five reconstructed motor neuron models (Fig. 3-6). The values of D_{path} at the boundaries of the intersection with the bistable area provided a quantitative prediction of the physical location of dendritic ion channels that generate plateau potentials. Our predictions that the separation distance is between 128 – 577 μm matches with theoretical estimates based on multicompartment anatomical models (Bui et al., 2006; Carlin et al., 2000b; Elbasiouny et al., 2005) and experimental measures (Ballou et al., 2006; Heckman et al., 2003). This result supports the conclusion that our reduced modeling approach provides valid predictions.

Similar to the conclusion of Booth and Rinzel (1995), bistable firing behaviour (*i.e.* Type IV) in our two-compartment model required the simultaneous presence of a stable limit cycle originating in the soma and a saddle-node bifurcation in the dendrite. The reason Type IV firing was restricted to a small area of the DDVA

domain was the influence of the ratio of DDVA parameters on input resistance of the dendrite (Equation (3-7)). In our modeling framework, the input resistance of the soma is controlled while the input resistance of the dendrite is a function of D_{path} and its relationship to A_{SD} and A_{DS} . Thus in our framework we can explore the role of electrotonic separation while maintaining somatic input resistance and allowing dendritic input resistance to change as a function of D_{path} in the same fashion as anatomically based multicompartment models (see Fig. 2-6 in Chapter 2 (Kim et al., 2009)). This is not possible in symmetrically coupled two-compartment models that use a theoretical coupling property like G_C to manipulate electrotonic separation because the input resistance of both compartments is the same and changes as a function G_C . The independent input resistances in the asymmetric model also played a role in generating other physiological firing patterns (*i.e.* Type I-III). Unlike Type IV firing patterns, Type I or II firing patterns occurred only when saddle node bifurcations at the dendritic compartment were absent during somatic spiking (see Fig. 3-3(b2) and 3-3(b3)). The absence of the saddle node bifurcation resulted because of the reduced input resistance of the dendrite with these DDVA parameters.

3.4.4 *Limitations in current modeling approach*

A fundamental assumption of two-compartment modeling approaches is that the complex anatomy of a single neuron can be lumped into two compartments. Our approach treats the dendritic compartment as a point over the dendrites at a specified distance from the soma. By choosing this modeling approach, the potential influence of individual dendrite properties on the dynamical behavior is lost. We chose this approximation to get a general understanding of how electrotonic coupling affected the nonlinear dynamics of reduced models. An advantage is that the relatively low dimension of the system equations facilitates mathematical analysis (Rinzel and Ermentrout, 1998). The dendritic compartment in the new reduced modeling could be extended to represent the multiple dendrites by applying the new DDVA properties measured between the soma and

the multiple dendritic points at the same distance from the soma, but for the general analysis as in this study it should be first clear whether the new DDVA properties systematically change for specific neuron morphology (Kim et al., 2009). In the case where individual dendrite properties might be more important, such as the staircase-like multiple inward currents observed in motor neurons (Carlin et al., 2009), the new reduced modeling would not be appropriate.

Our analysis of the effects of DDVA was restricted to the steady-state condition (*i.e.* DC input). This choice was made because of our interest in the plateau potential produced in the dendrites, which is well approximated by a DC signal. Voltage attenuation of transient signals (*i.e.* AC input), such as back-propagating action potentials, might be another intrinsic factor that affects the activation of voltage-gated ion channels in the dendrites (Hausser et al., 2000; Larkum et al., 1996; Larkum et al., 1999; Stuart et al., 1997). The DDVA analysis including AC signals is more complex: voltage attenuation is larger for AC than for DC signals (Tsai et al., 1994). The incorporation of DDVA with AC input into analytical solutions for reduced two-compartment models and the resulting effect on nonlinear dynamics remains to be done.

The system parameters of our reduced modeling approach are determined based on data measured from single neurons: input resistance and time constant as well the DDVA properties estimated from anatomical reconstructions. Measurement errors would be expected to generate disagreement in nonlinear dynamics between the reduced model and *in vivo* motor neuron behaviour. One potential experimental error results from the impalement of cytoplasmic membrane by a sharp microelectrode, resulting in a decrease in the estimated specific membrane resistivity of the soma (Holmes and Rall, 1992b; Major et al., 1993; Thurbon et al., 1998; Zengel et al., 1985). The presence of a somatic shunt has a significant effect on the DDVA properties (Kim et al., 2009). Dendritic input resistance of the reduced models, as a function of distance from the soma, does not match anatomical models that include a shunt (not published). If we assume that motor

neurons *in vivo* do not have a somatic shunt, then our reduced model is well suited to modeling their behaviour.

The Morris-Lecar formulation of active membrane mechanisms, while convenient for qualitative analysis of dynamics, is too simplified to allow comparison with specific motor neuron ion channel physiology (Carlin et al., 2000b; Hounsgaard and Mintz, 1988; Lee and Heckman, 1999b; Li and Bennett, 2003; Schwindt and Crill, 1980c). However, lumped description of inward and outward currents was sufficient for the purpose of the present theoretical study: to determine if DDVA alters nonlinear dynamics of model neurons. The simplicity of Morris-Lecar mechanisms allowed us to find a unique set of parameters (Table 3-1) for the asymmetric model that generated qualitatively similar bistable firing behaviour as the original symmetric model (Booth & Rinzel, 1995). It is unknown if a single set of standard parameters will be found when a full complement of physiological ion channels are included in our reduced modeling framework.

3.5 CONCLUSION

As far as we know, the current study is the first to show the direct interaction between physiological coupling properties (*i.e.* DDVA) and nonlinear dynamics of reduced two-compartment models. Asymmetric coupling between the soma and dendrites is a fundamental property that influences firing patterns and the area of the bistable solutions in the reduced models.

3.6 APPENDIX FOR CHAPTUER 3

The system equations of the asymmetric two-compartment model in Figure 3-1 were derived based on the previous dimensionless reduced model (Booth and

Rinzel, 1995), in which Morris-Lecar membrane excitability (Morris and Lecar, 1981) was employed to produce bistable firing patterns.

The membrane potential at the somatic compartment, $V_S(t)$:

$$C_m \dot{V}_S = -G_{Na} m_{S\infty} (V_S - E_{Na}) - G_{K,S} n_S (V_S - E_K) - G_{m,S} (V_S - E_{Leak}) - \frac{G_C}{p} (V_S - V_D) + I_S \quad (3-A1)$$

$$m_{S\infty}(V_S) = 0.5[1 + \tanh\{(V_S - v_{1S})/v_{2S}\}] \quad (3-A2)$$

$$\dot{n}_S = \phi_S \{n_{S\infty}(V_S) - n_S\} / \tau_S(V_S), \quad (3-A3)$$

where $n_{S\infty}(V_S) = 0.5[1 + \tanh\{(V_S - v_{3S})/v_{4S}\}]$ and $\tau_S(V_S) = [\cosh\{(V_S - v_{3S})/(2v_{4S})\}]^{-1}$

The membrane potential at the dendritic compartment, $V_D(t)$:

$$C_m \dot{V}_D = -G_{Ca} m_{D\infty} (V_D - E_{Ca}) - G_{K,D} n_D (V_D - E_K) - G_{m,D} (V_D - E_{Leak}) - \frac{G_C}{1-p} (V_D - V_S) \quad (3-A4)$$

$$m_{D\infty}(V_D) = 0.5[1 + \tanh\{(V_D - v_{1D})/v_{2D}\}] \quad (3-A5)$$

$$\dot{n}_D = \phi_D \{n_{D\infty}(V_D) - n_D\} / \tau_D(V_D), \quad (3-A6)$$

where $n_{D\infty}(V_D) = 0.5[1 + \tanh\{(V_D - v_{3D})/v_{4D}\}]$ and $\tau_D(V_D) = [\cosh\{(V_D - v_{3D})/(2v_{4D})\}]^{-1}$

Regular firing was mediated by lumped inward ($G_{Na} \cdot m_{S\infty}$) and outward ($G_{K,S} n_S$) conductances at the somatic compartment. Similarly the activation of plateau potential was regulated by lumped inward ($G_{Ca} \cdot m_{D\infty}$) and outward ($G_{K,D} n_D$) conductances at the dendritic compartment. Definitions and standard values of membrane parameters in the system equations were provided in Table 3-1.

3.7 BIBLIOGRAPHY FOR CHAPTER 3

Ballou, E. W., Smith, W. B., Anelli, R., and Heckman, C. J. (2006). Measuring dendritic distribution of membrane proteins. *J Neurosci Methods* 156, 257-266.

- Bennett, D. J., Hultborn, H., Fedirchuk, B., and Gorassini, M. (1998). Synaptic activation of plateaus in hindlimb motoneurons of decerebrate cats. *J Neurophysiol* 80, 2023-2037.
- Bennett, D. J., Li, Y., and Siu, M. (2001). Plateau potentials in sacrocaudal motoneurons of chronic spinal rats, recorded in vitro. *J Neurophysiol* 86, 1955-1971.
- Booth, V., and Rinzel, J. (1995). A minimal, compartmental model for a dendritic origin of bistability of motoneuron firing patterns. *J Comput Neurosci* 2, 299-312.
- Booth, V., Rinzel, J., and Kiehn, O. (1997). Compartmental model of vertebrate motoneurons for Ca²⁺-dependent spiking and plateau potentials under pharmacological treatment. *J Neurophysiol* 78, 3371-3385.
- Brunel, N. (2003). Dynamics and plasticity of stimulus-selective persistent activity in cortical network models. *Cereb Cortex* 13, 1151-1161.
- Bui, T. V., Ter-Mikaelian, M., Bedrossian, D., and Rose, P. K. (2006). Computational estimation of the distribution of L-type Ca(2+) channels in motoneurons based on variable threshold of activation of persistent inward currents. *J Neurophysiol* 95, 225-241.
- Carlin, K. P., Bui, T. V., Dai, Y., and Brownstone, R. M. (2009). Staircase currents in motoneurons: insight into the spatial arrangement of calcium channels in the dendritic tree. *J Neurosci* 29, 5343-5353.
- Carlin, K. P., Jiang, Z., and Brownstone, R. M. (2000a). Characterization of calcium currents in functionally mature mouse spinal motoneurons. *Eur J Neurosci* 12, 1624-1634.
- Carlin, K. P., Jones, K. E., Jiang, Z., Jordan, L. M., and Brownstone, R. M. (2000b). Dendritic L-type calcium currents in mouse spinal motoneurons: implications for bistability. *Eur J Neurosci* 12, 1635-1646.

- Carnevale, N. T., and Johnston, D. (1982). Electrophysiological characterization of remote chemical synapses. *J Neurophysiol* 47, 606-621.
- Cotel, F., Antri, M., Barthe, J. Y., and Orsal, D. (2009). Identified ankle extensor and flexor motoneurons display different firing profiles in the neonatal rat. *J Neurosci* 29, 2748-2753.
- Cullheim, S., Fleshman, J. W., Glenn, L. L., and Burke, R. E. (1987a). Membrane area and dendritic structure in type-identified triceps surae alpha motoneurons. *J Comp Neurol* 255, 68-81.
- Cullheim, S., Fleshman, J. W., Glenn, L. L., and Burke, R. E. (1987b). Three-dimensional architecture of dendritic trees in type-identified alpha-motoneurons. *J Comp Neurol* 255, 82-96.
- Dechter, R. (2003). *Constraint processing* (San Francisco: Morgan Kaufmann Publishers).
- Doiron, B., Laing, C., Longtin, A., and Maler, L. (2002). Ghostbursting: a novel neuronal burst mechanism. *J Comput Neurosci* 12, 5-25.
- Donohue, D. E., and Ascoli, G. A. (2008). A comparative computer simulation of dendritic morphology. *PLoS Comput Biol* 4, e1000089.
- Egorov, A. V., Hamam, B. N., Fransen, E., Hasselmo, M. E., and Alonso, A. A. (2002). Graded persistent activity in entorhinal cortex neurons. *Nature* 420, 173-178.
- Eken, T., and Kiehn, O. (1989). Bistable firing properties of soleus motor units in unrestrained rats. *Acta Physiol Scand* 136, 383-394.
- Elbasiouny, S. M., Bennett, D. J., and Mushahwar, V. K. (2005). Simulation of dendritic CaV1.3 channels in cat lumbar motoneurons: spatial distribution. *J Neurophysiol* 94, 3961-3974.

Ermentrout, B. (2002). *Simulating, analyzing, and animating dynamical systems : a guide to XPPAUT for researchers and students* (Philadelphia, Pa.: Society for Industrial & Applied Mathematics ; [Sunbury-on-Thames : Electronica Books & Media]).

Grande, G., Bui, T. V., and Rose, P. K. (2007). Estimates of the location of L-type Ca²⁺ channels in motoneurons of different size: a computational study. *J Neurophysiol* 97, 4023-4035.

Gutman, A. (1991). Bistability of dendrites. *Int J Neural Syst* 1, 291-304.

Hausser, M., Spruston, N., and Stuart, G. J. (2000). Diversity and dynamics of dendritic signaling. *Science* 290, 739-744.

Heckman, C. J., Lee, R. H., and Brownstone, R. M. (2003). Hyperexcitable dendrites in motoneurons and their neuromodulatory control during motor behavior. *Trends Neurosci* 26, 688-695.

Holmes, W. R., and Rall, W. (1992). Estimating the electrotonic structure of neurons with compartmental models. *J Neurophysiol* 68, 1438-1452.

Hounsgaard, J., Hultborn, H., Jespersen, B., and Kiehn, O. (1988). Bistability of alpha-motoneurons in the decerebrate cat and in the acute spinal cat after intravenous 5-hydroxytryptophan. *J Physiol* 405, 345-367.

Hounsgaard, J., and Kiehn, O. (1989). Serotonin-induced bistability of turtle motoneurons caused by a nifedipine-sensitive calcium plateau potential. *J Physiol* 414, 265-282.

Hounsgaard, J., and Kiehn, O. (1993). Calcium spikes and calcium plateaux evoked by differential polarization in dendrites of turtle motoneurons in vitro. *J Physiol* 468, 245-259.

Hounsgaard, J., and Mintz, I. (1988). Calcium conductance and firing properties of spinal motoneurons in the turtle. *J Physiol* 398, 591-603.

- Jaffe, D. B., and Carnevale, N. T. (1999). Passive normalization of synaptic integration influenced by dendritic architecture. *J Neurophysiol* 82, 3268-3285.
- Jones KE, C. K., J. R., et al. (2000). Simulation techniques for localising and identifying the kinetics of calcium channels in dendritic neurons. *Neurocomputing* 32, 173-180.
- Katz, B., and Miledi, R. (1963). A Study of Spontaneous Miniature Potentials in Spinal Motoneurons. *J Physiol* 168, 389-422.
- Kiehn, O. (1991). Plateau potentials and active integration in the 'final common pathway' for motor behaviour. *Trends Neurosci* 14, 68-73.
- Kiehn, O., and Eken, T. (1997). Prolonged firing in motor units: evidence of plateau potentials in human motoneurons? *J Neurophysiol* 78, 3061-3068.
- Kim, H., Major, L. A., and Jones, K. E. (2009). Derivation of cable parameters for a reduced model that retains asymmetric voltage attenuation of reconstructed spinal motor neuron dendrites. *J Comput Neurosci* 27, 321-336.
- Larkum, M. E., Rioult, M. G., and Luscher, H. R. (1996). Propagation of action potentials in the dendrites of neurons from rat spinal cord slice cultures. *J Neurophysiol* 75, 154-170.
- Larkum, M. E., Zhu, J. J., and Sakmann, B. (1999). A new cellular mechanism for coupling inputs arriving at different cortical layers. *Nature* 398, 338-341.
- Lee, R. H., and Heckman, C. J. (1996). Influence of voltage-sensitive dendritic conductances on bistable firing and effective synaptic current in cat spinal motoneurons in vivo. *J Neurophysiol* 76, 2107-2110.
- Lee, R. H., and Heckman, C. J. (1998a). Bistability in spinal motoneurons in vivo: systematic variations in persistent inward currents. *J Neurophysiol* 80, 583-593.

- Lee, R. H., and Heckman, C. J. (1998b). Bistability in spinal motoneurons in vivo: systematic variations in rhythmic firing patterns. *J Neurophysiol* *80*, 572-582.
- Lee, R. H., and Heckman, C. J. (1999). Paradoxical effect of QX-314 on persistent inward currents and bistable behavior in spinal motoneurons in vivo. *J Neurophysiol* *82*, 2518-2527.
- Lee, R. H., and Heckman, C. J. (2000). Adjustable amplification of synaptic input in the dendrites of spinal motoneurons in vivo. *J Neurosci* *20*, 6734-6740.
- Li, W. C., Soffe, S. R., Wolf, E., and Roberts, A. (2006). Persistent responses to brief stimuli: feedback excitation among brainstem neurons. *J Neurosci* *26*, 4026-4035.
- Li, Y., and Bennett, D. J. (2003). Persistent sodium and calcium currents cause plateau potentials in motoneurons of chronic spinal rats. *J Neurophysiol* *90*, 857-869.
- Llinas, R., and Sugimori, M. (1980). Electrophysiological properties of in vitro Purkinje cell somata in mammalian cerebellar slices. *J Physiol* *305*, 171-195.
- Mainen, Z. F., and Sejnowski, T. J. (1996). Influence of dendritic structure on firing pattern in model neocortical neurons. *Nature* *382*, 363-366.
- Major, G., Evans, J. D., and Jack, J. J. (1993). Solutions for transients in arbitrarily branching cables: I. Voltage recording with a somatic shunt. *Biophys J* *65*, 423-449.
- Morris, C., and Lecar, H. (1981). Voltage oscillations in the barnacle giant muscle fiber. *Biophys J* *35*, 193-213.
- Pinsky, P. F., and Rinzel, J. (1994). Intrinsic and network rhythmogenesis in a reduced Traub model for CA3 neurons. *J Comput Neurosci* *1*, 39-60.

Rall, W., and Rinzel, J. (1973). Branch input resistance and steady attenuation for input to one branch of a dendritic neuron model. *Biophys J* 13, 648-687.

Rinzel, J., and Ermentrout, B. (1998). Analysis of neural excitability and oscillations. *Methods in neuronal modeling: from ions to networks*, C. Koch and I. Segev. Cambridge, MA, MIT Press: 251–291.

Rinzel, J., and Rall, W. (1974). Transient response in a dendritic neuron model for current injected at one branch. *Biophys J* 14, 759-790.

Schwindt, P. C., and Crill, W. E. (1980). Properties of a persistent inward current in normal and TEA-injected motoneurons. *J Neurophysiol* 43, 1700-1724.

Simon, M., Perrier, J. F., and Hounsgaard, J. (2003). Subcellular distribution of L-type Ca²⁺ channels responsible for plateau potentials in motoneurons from the lumbar spinal cord of the turtle. *Eur J Neurosci* 18, 258-266.

Steriade, M. (1999). Coherent oscillations and short-term plasticity in corticothalamic networks. *Trends Neurosci* 22, 337-345.

Stuart, G., Spruston, N., Sakmann, B., and Hausser, M. (1997). Action potential initiation and backpropagation in neurons of the mammalian CNS. *Trends Neurosci* 20, 125-131.

Thurbon, D., Luscher, H. R., Hofstetter, T., and Redman, S. J. (1998). Passive electrical properties of ventral horn neurons in rat spinal cord slices. *J Neurophysiol* 80, 2485-2502.

Tsai, K. Y., Carnevale, N. T., Claiborne, B. J., and Brown, T. H. (1994). Efficient mapping from neuroanatomical to electrotonic space. *Network: Computation in Neural Systems* 5, 21 - 46

Zengel, J. E., Reid, S. A., Sybert, G. W., and Munson, J. B. (1985). Membrane electrical properties and prediction of motor-unit type of medial gastrocnemius motoneurons in the cat. *J Neurophysiol* 53, 1323-1344.

CHAPTER 4: Frequency response of the passive dendritic trees that constrains the bistable firing behaviour of a reduced neuron model

Glossary

| | |
|----------------|-----------------------------------------------------------------|
| VGIC | Voltage Gated Ion Channel |
| PIC | Persistent Inward Current |
| DDVA | Direction Dependant Voltage Attenuation |
| AC | Alternating Current |
| DC | Direct Current |
| VA_{SD}^{DC} | Voltage Attenuation factor from Soma to Dendrites with DC input |
| VA_{DS}^{DC} | Voltage Attenuation factor from Dendrites to Soma with DC input |
| VA_{SD}^{AC} | Voltage Attenuation factor from Soma to Dendrites with AC input |
| CI | Characteristic Index |
| TTP | Time To onset of Plateau potential |
| TES | Time to End of Somatic spiking |
| DSF | Difference in Spiking Frequency |

4.1 INTRODUCTION

Transient electrical signals generated at the cell body such as action potentials propagate down to the axonal terminals and also backward into the dendritic trees to interact with a number of voltage-gated ion channels (VGICs). The physical separation of the VGICs responsible for plateau potentials, in the dendrites, from

the spiking generating mechanisms, in the soma, facilitates bistable firing behaviour observed in many neurons: the coexistence of two stable states given the same current input (Brunel, 2003; Egorov et al., 2002; Hounsgaard and Kiehn, 1989; Li et al., 2006; Llinas and Sugimori, 1980; Steriade, 1999). The bistable firing patterns have been extensively investigated in motor neurons (Lee and Heckman, 1996; Li and Bennett, 2003; Schwindt and Crill, 1980c), showing the experimental characteristics under triangular current stimulation protocol: 1) the higher firing frequency during the descending phase of current stimulation than the ascending phase, leading to the counter-clockwise frequency hysteresis in the frequency-current relationship (Lee and Heckman, 1998a; Lee and Heckman, 1998b) and 2) the sustained firing at the lower current intensity during the descending phase of current stimulation than the current threshold for the spiking during the ascending phase (Bennett et al., 2001). L-type Ca^{2+} channels slowly activated at low voltage and generating persistent inward currents (PICs), have been suggested to be responsible for plateau potentials that give rise to bistable firing behaviour (Booth et al., 1997; Carlin et al., 2000a; Hounsgaard and Mintz, 1988; Li and Bennett, 2003; Schwindt and Crill, 1980c; Svirskis and Hounsgaard, 1997). Anatomically, the calcium mediated PIC channels have been shown to be concentrated on the dendritic branches physically distal to the soma i.e. 300-500 μm (Ballou et al., 2006; Carlin et al., 2000b; Elbasiouny et al., 2005; Grande et al., 2007; Heckman et al., 2003).

The nonlinear (i.e. bistable) dynamics of motor neurons is governed by the spatio-temporal interaction between different types of somatic and dendritic VGICs. This interaction has been shown to be significantly influenced by signal propagations of the complex dendritic systems in our previous study (Kim and Jones, 2010). The dendritic signaling properties were characterized there by measuring voltage attenuations from the soma to all single points over anatomically reconstructed dendrites and vice versa, with direct-current (DC) inputs which corresponded to the somatic excitatory current stimulation and dendritic plateau potential generating currents in the experimental context. For a

analytical and numerical investigation, we have developed a biophysically derived two-compartment modeling framework where all passive membrane parameters were analytically determined to retain direction-dependent voltage attenuations (DDVAs) for the dendritic DC-signaling, as well as essential biophysical properties including input resistance and time constant (Kim et al., 2009). Analytically manipulating DDVA properties in this reduced modeling framework, it was found that the DDVAs were tightly correlated to the input resistance in the dendrites and thus variations of DDVA property profoundly altered the firing output behaviour of the reduced MN model showing all types of firing patterns observed experimentally: Type I-IV (Bennett et al., 2001), and fully and partially bistable firing (Lee and Heckman, 1998b).

In addition to the DC signals over the dendrites, the alternating-current (AC) signaling has also been observed to be essentially involved in bistable firing of motor neurons. To generate fully bistable or Type IV firing (i.e. counter-clockwise frequency hysteresis with sustained firing) using triangular current stimulation at the soma, the current threshold for generating action potentials must be lower than the threshold for plateau potentials. Thus action potentials may propagate back into the dendrites and play an important role in the activation of dendritic VGICs (Larkum et al., 1996), that generate the plateau potential and associated bistable firing patterns in experimental data.

In this study, we presented the importance of dendritic AC signaling property in understanding the potential impact of back-propagating action potentials on bistable firing patterns. The spatial frequency-response of the passive dendrites in anatomically reconstructed motor neurons was first characterized for the AC signal with a fixed frequency (i.e. 250 Hz corresponding to a action potential width of about 2 milliseconds). We expanded our previous reduced modeling framework reflecting only dendritic DC-signaling (hereafter referred to as a DC-RM) to incorporate the characterized AC signaling property of the dendrites (the expanded reduced modeling was referred to as a DC/AC-RM). Then active

membrane mechanisms were added to the passive DC/AC-RM modifying Morris-Lecar formulation. Evaluating the nonlinear dynamics (i.e. bistable firing) of the new reduced motor neuron model over the whole range of the AC signal attenuation along with the DC signaling properties (i.e. DDVA), we demonstrated how the dendritic AC signaling influenced the interaction of the back-propagating action potentials on the model bistability. Finally, we assessed how bistable behaviour of the new reduced model compared with the physiological dendritic signaling properties directly measured from anatomically-reconstructed motor neuron models for both DC and AC signals.

4.2 METHODS

4.2.1 *Anatomical neuron models*

The anatomical data of five type-identified cat α -motor neurons, contributed by Robert Burke's lab, were downloaded from <http://NeuroMorpho.Org> (Ascoli, 2006) The individual anatomical data was translated into the NEURON simulation environment (Carnevale and Hines, 2005) using the Import3D tool and were corrected to match the soma geometry to the dimensions previously reported (Cullheim et al., 1987a). We used the non-uniform specific membrane resistivity ($R_m \Omega \cdot \text{cm}^2$) with the same values as previously reported (Table 4-1), assuming a cytoplasmic resistivity (R_a) of $70 \Omega \cdot \text{cm}$ and a specific membrane capacitance (C_m) of $1 \mu\text{F}/\text{cm}^2$. The electrotonics (i.e. input resistance and system time constant) of all passive anatomical models were well matched to those measured experimentally.

Table 4-1. Passive membrane properties of the type-identified anatomical motor neuron models

| Cells | | R_m | |
|--------------|------|-------|----------|
| Motor Neuron | Type | Soma | Dendrite |
| V1 (36/4) | S | 455 | 15,500 |
| V2 (38/2) | FF | 66 | 17,000 |
| V3 (41/2) | FF | 70 | 20,000 |
| V4 (42/4) | FR | 120 | 17,000 |
| V6 (43/5) | FR | 225 | 11,000 |

Cell numbers and unit types in the first column matched with those in (Fleshman et al., 1988); Specific membrane resistivity, R_m , was non-uniformly assigned with lower value in the soma compared to dendrites.

4.2.2 Frequency response analysis

Because of its spatial geometry, the frequency response (i.e. amplitude ratio and phase shift) (Phillips and Harbor, 2000) of the passive dendritic system was determined as a function of both signal frequency (ω_f) and path length (D_{path}) from the soma. The spatial variations of frequency response over the dendrites were first characterized with the constant ω_f , then the dendritic response to the AC signals with various ω_f (i.e. frequency vector) was evaluated at the fixed D_{path} where the PIC channels are believed to be clustered on the dendrites. For the spatial frequency response analysis, action potentials propagating into the dendrites were represented with a sinusoidal wave (i.e. AC) with the characteristic frequency ($\omega_{f,C}$) of 250 Hz. The frequency was selected because the average spike width for motor neurons is about 2 ms (Coombs et al., 1955) and assuming the spike represents half a period of a sinusoidal input, i.e. 4 ms period is equivalent to 250 Hz. Applying this AC signal to the soma of the anatomical models in Table 4-1, the characteristic frequency response was calculated between the soma and all individual points over the dendritic trees as a function of D_{path} using the Impedance class of NEURON software. The amplitude ratio and phase shift data were separately plotted like a Bode plot with respect to D_{path} and fit with a single function to represent the overall response trend. For the comparison of the characteristic frequency response in different types of anatomical motor neuron models, the amplitude (VA) and phase (Φ) response at the particular distance from the soma were represented in a plane vector and plotted by a graph such as a Nyquist plot with respect to D_{path} in a complex domain consisting of Imaginary (Im) and Real (Re) axis. The real (x) and imaginary (y) component of the frequency-response vector can be formulated in the general form,

$$x = VA(\omega_f, D_{\text{Path}}) \cdot \cos(\Phi(\omega_f, D_{\text{Path}})) \quad (4-1)$$

$$y = VA(\omega_f, D_{\text{Path}}) \cdot \sin(\Phi(\omega_f, D_{\text{Path}})) \quad (4-2)$$

The distance and angle of the individual points from the origin in the complex plane correspond to the amplitude and phase response of the dendrites measured at the specific D_{path} (refer to Fig. 4-1(d) for details).

Over the wide range of ω_f , the new reduced modeling approach for the dendritic AC signaling was validated by comparing the frequency response between the reduced and anatomically reconstructed models at the fixed D_{path} (i.e. 300 μm).

4.2.3 Reduced neuronal modeling

The analytical expansion of the previous conductance based two-compartment modeling framework (i.e. DC-RM) to retain the dendritic AC signaling property was possible by allowing the membrane capacitance in individual compartments to be independent.

4.2.3.1 Passive electrical properties

Under the Kirchhoff's current law, the passive dynamics of the DC/AC-RM was governed by the following current-balance equations for each compartment,

$$C_{m,S} \dot{V}_S = -G_{m,S}(V_S - E_{Leak}) - \frac{G_C}{p}(V_S - V_D) + I_S \quad (4-3)$$

$$C_{m,D} \dot{V}_D = -G_{m,D}(V_D - E_{Leak}) - \frac{G_C}{1-p}(V_D - V_S) + I_D \quad (4-4)$$

where V_S and V_D are membrane potentials in the somatic and dendritic compartment. $C_{m,S}=53.103$ and $C_{m,D}=0.39$ are membrane capacitances normalized by somatic and dendritic surface area. $G_{m,S}=5.067$ and $G_{m,D}=0.044$ are membrane conductances normalized with somatic and dendritic surface area. $G_C=0.299$ is coupling conductance normalized with total surface area. $E_{Leak} = -0.7$ is reversal potential for leak current. I_S and I_D are the current density injected at the soma and dendritic compartment. All passive model parameters in Equation (4-3) & (4-4) were analytically determined by solving the inverse equations (refer to Results 3.2

and Appendix A) for the essential biophysical properties directly measured from the anatomical model (i.e. V1 in Table 4-1): input resistance ($R_N=1.9 \text{ M}\Omega$), system time constant ($\tau_m=10.4 \text{ ms}$), and the distance-dependent signal propagation properties between the soma and dendrites; the soma-to-dendrite voltage attenuations with DC ($VA_{SD}^{DC}(D_{\text{path}}=300\mu\text{m})=0.89$) and AC ($VA_{SD}^{AC}(D_{\text{path}}=300\mu\text{m})=0.49$) input, the dendrite-to-soma voltage attenuation with DC input ($VA_{DS}^{DC}(D_{\text{path}}=300\mu\text{m})=0.26$), and the morphological factor ($p=0.168$) defined by the ratio of somatic to total surface area. The values of three soma-dendrite signaling properties and p were determined when D_{path} was specified to separate two compartments. All units are dimensionless unless specifically stated (Booth and Rinzel, 1995).

4.2.3.2 Active electrical properties

The bistable firing behaviour of the DC/AC-RM was generated by the interaction between action potential and plateau potential generating membrane mechanisms. The spiking at the soma was mediated by fast Na^+ and delayed-rectified K^+ currents ($\sum I_{A,S}$) formulated on the Morris-Lecar model (Morris and Lecar, 1981), whereas the plateau potentials at the dendrites were evoked by voltage- and time-dependent L-type Ca^{2+} and delayed-rectified K^+ currents ($\sum I_{A,D}$) modifying the Morris-Lecar membrane excitability where the inward current mediated by Ca^{2+} was instantaneously activated. After the passive membrane properties were specified in the section 2.3.1, the active currents $\sum I_{A,S}$ and $\sum I_{A,D}$ were added to the soma corresponding to the right-hand side of the system equation (4-3) and the dendrite corresponding to the right hand side of the equation (4-4). The dynamics of individual active currents were governed by following conductance based equations,

$$\sum I_{A,S} = -G_{Na}m_{S\infty}(V_S - E_{Na}) - G_{K,S}n_S(V_S - E_K) \quad (4-5)$$

$$m_{S\infty}(V_S) = 0.5 \left(1 + \tanh \frac{V_S + 0.01}{0.15} \right)$$

$$\dot{n}_S = 0.2 \left(\frac{n_{S\infty}(V_S) - n_S}{\tau_S(V_S)} \right)$$

$$\text{where } n_{S\infty}(V_S) = 0.5 \left(1 + \tanh \frac{V_S + 0.04}{0.1} \right), \tau_S(V_S) = \left(\cosh \frac{V_S + 0.04}{0.1} \right)^{-1}$$

$$\sum I_{A,D} = -G_{Ca} m_D (V_D - E_{Ca}) - G_{K,D} n_D (V_D - E_K) \quad (4-6)$$

$$\dot{m}_D = 0.2 \left(\frac{m_{D\infty}(V_D) - m_D}{\tau_{mD}(V_D)} \right)$$

$$\text{where } m_{D\infty}(V_D) = 0.5 \left(1 + \tanh \frac{V_D - 0.07}{0.1} \right), \tau_{mD}(V_D) = \left(\cosh \frac{V_D}{0.1} \right)^{-1}$$

$$\dot{n}_D = 0.2 \left(\frac{n_{D\infty}(V_D) - n_D}{\tau_{nD}(V_D)} \right)$$

$$\text{where } n_{D\infty}(V_D) = 0.5 \left(1 + \tanh \frac{V_D}{0.1} \right), \tau_{nD}(V_D) = \left(\cosh \frac{V_D}{0.1} \right)^{-1}$$

All maximum conductance and equilibrium potential values in Equation (4-5) and (4-6) were adopted from bistable DC-RM, so that the bifurcation structure for the bistable firing behaviour was conserved in the DC/AC-RM: a Hopf bifurcation at the onset of somatic spiking and a saddle-node bifurcation at the onset of the dendritic plateau potential. Bifurcation analysis demonstrating these dynamics is presented in Results (see (a2) & (b2) in Fig. 4-4). $G_{Na}=11.0$ and $G_{K,S}=14.0$ are maximum conductances for voltage-gated Na^+ and K^+ currents in the soma. $G_{Ca}=0.89$ and $G_{K,D}=0.44$ are maximum conductances for voltage-gated Ca^{2+} and K^+ current in the dendrite. $E_{Na}=1.0$, $E_{Ca}=1.0$ and $E_K = -0.7$ are reversal potentials for Na^+ , Ca^{2+} and K^+ respectively. All units are dimensionless unless specifically stated.

4.2.4 Simulation

We evoked the bistable firing patterns using triangular current stimulation to the somatic compartment. Based on the time courses of somatic and dendritic membrane potentials and their instantaneous firing frequencies, three characteristic indexes were identified to evaluate the presence of the bistable firing patterns (Kim and Jones, 2010): Time To onset of Plateau potential (TTP), Time to End of somatic Spiking (TES) and Difference in Spiking Frequency (DSF). Briefly, the positive TTP, TES and DSF represent the delayed onset of the plateau potential in the dendrites, the sustained firing during the down phase of current stimulation and counter-clockwise frequency hysteresis respectively. The details of all three characteristic indexes are illustrated in Fig. 4-3. Bistable firing behaviour was operationally determined when all three indexes had positive values. This analysis is commonly referred to as the constraints inference method with three constraints ($TTP > 0$, $TES > 0$, and $DSF > 0$) (Dechter, 2003). Numerical bifurcation analysis of the DC/AC-RM was first conducted for three representative AC signal attenuations. Then the simulations were done with the DC/AC-RM keeping the active properties constant and independently varying three biophysical signaling parameters (i.e. VA_{SD}^{DC} , VA_{DS}^{DC} and VA_{SD}^{AC}) from the default value. We evaluated the three characteristic indexes at each location of the three dimensional parameter space, where the location (x, y, z) is defined by the value $(VA_{SD}^{DC}, VA_{DS}^{DC}, VA_{SD}^{AC})$. The solution parameter space for the model bistability was defined as a volume where all three characteristic indexes were positive. If the dendritic signaling only for DC components is predominant in determining the bistable firing behaviour of the reduced model, the volume of solution space will not change as a function of VA_{SD}^{AC} . Then the bistable solution space would be completely defined by the DC signaling parameters (VA_{SD}^{DC} and VA_{DS}^{DC}) and the DC/AC-RM would not be needed.

4.3 RESULTS

4.3.1 Frequency response of the anatomically reconstructed models

Applying the AC signal with the fixed frequency of 250 Hz to the soma, the distributed frequency response (amplitude and phase) of the anatomically reconstructed motor neuron models was characterized along the path length (D_{path}) of their dendrites from the soma. Figure 4-1a and 4-1b shows the anatomy of one of the anatomical models (V1 in Table 4-1) and the amplitude (or voltage) attenuation of the input signal that is caused by low pass filtering effects of the passive dendrites. The amplitude of the AC signal decayed exponentially with the increasing distance from the soma. The degree of amplitude attenuation was more severe for the AC ($\omega_f = 250$ Hz) than DC ($\omega_f = 0$ Hz) signal injected to the soma. Whereas the soma-to-dendrite AC amplitude attenuation was less than the dendrite-to-soma DC amplitude attenuation at most values of D_{path} . The amplitude response data (filled black circles) was fit with a single exponential function (solid black line) to quantify the rate of amplitude attenuation with a voltage (or exponential) decay constant (η). The η was also used in our reduced modeling approach to estimate the degree of signal attenuation at the specific D_{path} from the soma.

Figure 4-1c shows the phase lag behind the AC input signal along the path of the dendrites. As D_{path} approached the dendritic terminals, the phase lag was increased from 0 to -2π radians. The distance at which the signal became out-of-phase (i.e. $-\pi$ or 2 ms lag with 250 Hz signal) was relatively far from the soma (i.e. $D_{\text{path}}=1200$ μm). Even at the most distal branch terminal of the dendritic trees (i.e. $D_{\text{path}} = 1854$ μm), the signal phase was delayed only by approximately -2π radians or 4 ms. The overall phase response data (filled black circles) decayed not exponentially, but rather slowly fitting to a cubic polynomial function (solid black line) as a function of D_{path} .

Figure 4-1d demonstrates the overall frequency response including both the amplitude ratio and phase shift in a complex domain as the D_{path} appears as a

parameter. It was clear in Fig. 4-1(b) & 4-1(c) that the amplitude of the AC signal more rapidly decreased than the phase response as D_{path} increased from 0 to infinity. Resultantly the overall shape of the spatial frequency response (solid gray line in Fig. 4-1(d)) was similar to that of a first-order system response (compare the solid gray line in Fig. 4-2(b)) with respect to the distance instead of the signal frequency. The voltage-gated ion channels responsible for the bistable firing behaviour have been suggested to be distributed at least $D_{\text{path}} = 300 - 500 \mu\text{m}$ away from the soma, based on experimental (Ballou et al., 2006; Heckman et al., 2003) and theoretical studies (Carlin et al., 2000b; Elbasiouny et al., 2005; Grande et al., 2007). At the average over this range, the amplitude of the AC signal attenuated by 71 % compared to the input signal, whereas the phase was lagged only by 13 % (i.e. 0.26π or 0.52 ms lag) of -2π radians that is the phase lag at the most end of the dendrites (i.e. $D_{\text{path}} = 1854 \mu\text{m}$). At $D_{\text{path}} = 666.1 \mu\text{m}$ where the phase (delay time) was delayed by 25 % (i.e. $-\pi/2$ or 1 ms lag) of -2π radians, the signal amplitude decayed by almost 80 % of the input amplitude. Furthermore the time scale of signal delay (i.e. maximum 4 ms at the dendritic terminal with 250Hz signal) was much faster compared to the activation time constant (at least 30 ms) of the PICs originated in the dendrites (Booth et al., 1997; Carlin et al., 2000b; Powers, 1993). These results indicate that the changes in the signal delay within 2π radians or 4 ms may not make significant effects on the onset timing of the PIC channels which has been shown to be critical to determine the type of firing patterns in motor neurons (Bennett et al., 2001).

Figure 4-1 illustrates a representative frequency response of the type-identified anatomical motor neuron models in Table 4-1. The four other types of motor neuron models showed qualitatively similar results (Appendix B).

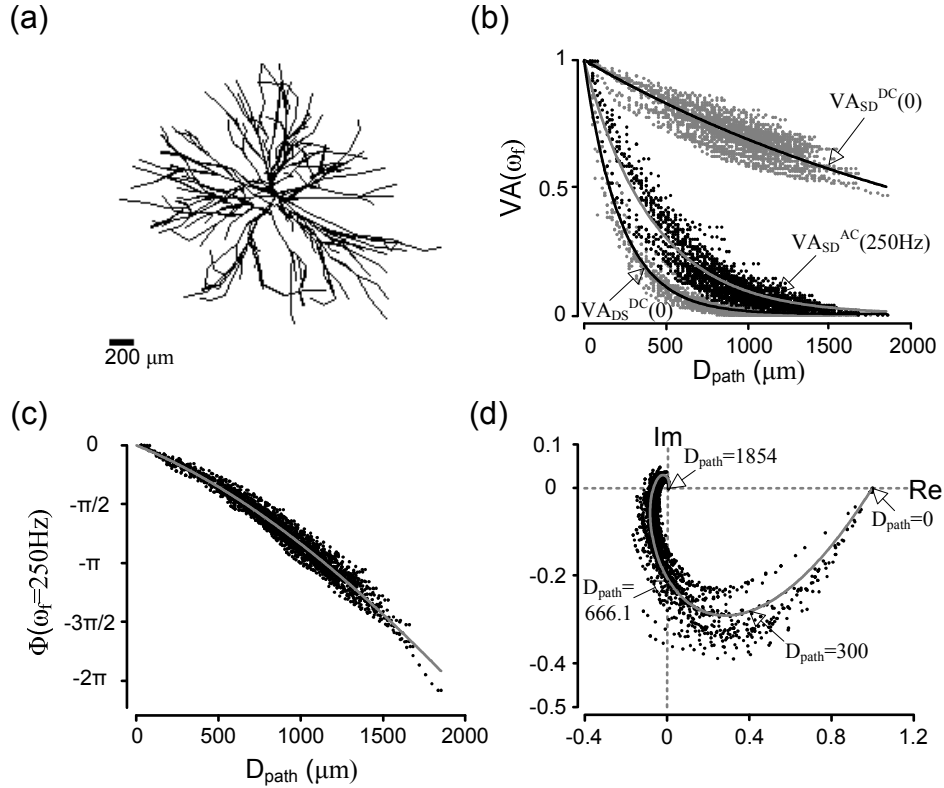


Figure 4-1. Spatial frequency response of an anatomically reconstructed motor neuron model. (a). Morphology of a representative motor neuron (V1 in Table 4-1). (b). Amplitude response (VA): the voltage attenuation data ($VA_{SD}^{AC}(250\text{Hz})$ in the middle black dots) for the soma-to-dendrite AC signal with the fixed frequency, $\omega_f=250$ Hz, was superimposed on that for the DC signals in the same direction ($VA_{SD}^{DC}(0)$ in the top gray dots) and in the opposite direction ($VA_{DS}^{DC}(0)$ in the bottom gray dots) as a function of the path length (D_{path}) from the soma. Each data set was fitted with a single exponential function: $\exp(-D_{\text{path}}/2678.7)$ for the $VA_{SD}^{DC}(0)$ (upper black line), $\exp(-D_{\text{path}}/420.1)$ for the $VA_{SD}^{AC}(250\text{ Hz})$ (middle gray line) and $\exp(-D_{\text{path}}/225)$ for the $VA_{DS}^{DC}(0)$ (bottom black line). (c). Phase response (Φ): the phase delay data (black dots) was presented in radian as a function of D_{path} , fitting with a cubic polynomial function ($6.8 \cdot 10^{-11} \cdot D_{\text{path}}^3 - 9.2 \cdot 10^{-7} \cdot D_{\text{path}}^2 - 0.0018 \cdot D_{\text{path}}$ for gray line). The minus radians indicate the phase lag behind the input signal. (d). The vector representation of distance dependent frequency response in the complex plane consisting of

Imaginary (Im in the ordinate) and Real (Re in the abscissa) axis. The imaginary and real component of a vector pointing to the individual data points (black dots) were calculated using Equation (4-1) & (4-2). The distance and angle of the individual vectors from the origin correspond to the amplitude and phase response of the dendrites measured at the specific D_{path} in (b) and (c). Fitting curve (gray line) was also determined from (b) and (c).

4.3.2 Expansion of two-compartment modeling framework

Having characterized the spatial frequency response of the complex dendrites, the amplitude attenuation of the AC signal turned out to be much more sensitive to the distance from the soma than the phase lag. To retain the AC signal amplitude attenuation, we released the uniformity of the membrane capacitance in the DC-RM and derived inverse equations for five unknown cable parameters (i.e. $G_{m,S}$, $G_{m,D}$, $C_{m,S}$, $C_{m,D}$, G_C in Methods) from forward equations for five biophysical properties of complex anatomical models (i.e. R_N , τ_m , VA_{SD}^{DC} , VA_{DS}^{DC} and VA_{SD}^{AC}).

The inverse equations for $G_{m,D}$, $G_{m,D}$ and G_C were identical to those derived for the DC-RM since $G_{m,D}$, $G_{m,D}$ and G_C were perfectly constrained by R_N and DC signaling properties (VA_{SD}^{DC} and VA_{DS}^{DC}). Thus we derived here the inverse equations of $C_{m,D}$ and $C_{m,S}$, first for $C_{m,D}$ from the forward equation of VA_{SD}^{AC} and then for $C_{m,S}$ from the forward equation of τ_m . The inverse equations for DC model parameters (i.e. $G_{m,D}$, $G_{m,D}$ and G_C) were presented in Appendix A containing all forward and inverse equations for the DC-RM.

Defining V_S and V_D to be the voltage deviation from resting membrane potential in the soma and dendrites, Equation (4-4) can be rewritten in the form of,

$$C_{m,D} \dot{V}_D = -G_{m,D} V_D - \frac{G_C}{1-p} (V_D - V_S) + I_D \quad (4-7)$$

Applying Laplace transform

$$\int_0^{\infty} e^{-st} f(t) dt = F(s) \quad (4-8)$$

to the equation (4-7) with $I_D=0$, the equation (4-7) is transformed into a function of a parameter s ,

$$C_{m,D}(sV_D(s) - V_D(0)) = -G_{m,D}V_D(s) - \frac{G_C}{1-p}(V_D(s) - V_S(s)) \quad (4-9)$$

Then the transfer function from the soma to the dendrites is given in the s-domain,

$$VA_{SD}(s) = \frac{V_D(s)}{V_S(s)} = \frac{G_C}{G_C + G_{m,D}(1-p) + sC_{m,D}(1-p)} \quad (4-10)$$

where VA_{SD} represents the amplitude attenuation of the AC input signal propagating from the soma and dendrites.

Mathematically mapping the s-domain to the complex domain by inserting $j\omega$, the frequency-response function of the DC/AC-RM is,

$$VA_{SD}(j\omega) = \frac{G_C}{G_C + G_{m,D}(1-p) + j\omega C_{m,D}(1-p)} \quad (4-11)$$

The amplitude response corresponds to the magnitude of the complex number in Equation (4-11) given a particular input signal frequency (ω_f),

$$VA_{SD}^{AC} = |VA_{SD}(j\omega_f)| = \frac{G_C}{\sqrt{\{G_C + G_{m,D}(1-p)\}^2 + \{\omega_f C_{m,D}(1-p)\}^2}} \quad (4-12)$$

When ω_f is zero the equation (4-12) becomes identical to the soma-to-dendritic voltage attenuation (i.e. VA_{SD}^{DC}) for DC input (Appendix A).

Rearranging equation (4-12) to get the inverse equation for the dendritic membrane capacitance ($C_{m,D}$),

$$C_{m,D} = \frac{1}{\omega_f(1-p)} \sqrt{\frac{G_C^2}{(VA_{SD}^{AC})^2} - \{G_C + G_{m,D}(1-p)\}^2} \quad (4-13)$$

$C_{m,D}$ has been analytically determined from the forward equation of the VA_{SD}^{AC} given ω_f and D_{path} . Note that other passive membrane parameters (i.e. $G_{m,D}$ and G_C in Equation (4-13)) are predetermined given R_N and dendritic DC signal attenuations (VA_{SD}^{DC} and VA_{DS}^{DC}) measured at the specific D_{path} from the soma.

The inverse equation for the membrane capacitance in the soma ($C_{m,S}$) was derived from the forward equation for the system time constant (τ_m). Starting with V_S and V_D , the system equations (4-3) & (4-4) can be rearranged into the matrix form to get the system matrix,

$$\mathbf{A} = \begin{bmatrix} -\frac{1}{C_{m,S}} \cdot \left(\frac{G_C}{p} + G_{m,S} \right) & \frac{1}{C_{m,S}} \cdot \frac{G_C}{p} \\ \frac{1}{C_{m,D}} \cdot \frac{G_C}{1-p} & -\frac{1}{C_{m,D}} \cdot \left(\frac{G_C}{1-p} + G_{m,D} \right) \end{bmatrix} \quad (4-14)$$

The characteristic equation for the system matrix A is quadratic in a single scalar variable λ (i.e. the eigenvalue),

$$\left\{ \frac{1}{C_{m,S}} \left(\frac{G_C}{p} + G_{m,S} \right) - \lambda \right\} \cdot \left\{ \frac{1}{C_{m,D}} \left(\frac{G_C}{1-p} + G_{m,D} \right) - \lambda \right\} - \frac{1}{C_{m,S}C_{m,D}} \cdot \left\{ \frac{G_C^2}{p(1-p)} \right\} = 0 \quad (4-15)$$

Since Equation (4-15) is a second-order polynomial function, it has two solutions or eigenvalues (i.e. $\lambda_1 < \lambda_2$). The system time constant (τ_m) corresponds to the reciprocal of the smaller eigenvalue,

$$\tau_m = \frac{1}{\lambda_1} = \tau_{m,1}(\tau_{m,2} + \sqrt{\tau_{m,3}}) \quad (4-16)$$

where $\tau_{m,1} = \frac{0.5}{(1-p)(pG_{m,S}G_{m,D} + G_CG_{m,D}) + pG_{m,S}G_C}$

$\tau_{m,2} = p(1-p)(G_{m,S}C_{m,D} + G_{m,D}C_{m,S}) + (1-p)C_{m,D}G_C + pC_{m,S}G_C$

$$\begin{aligned} \tau_{m,3} = & \left[2pG_C^2 - 2(1-p)p^2 \left\{ (1-p)G_{m,D} + G_C \right\} G_{m,S} + 2p \left\{ 2pG_{m,D} - pG_C - G_{m,D} \right\} \right] C_{m,D} C_{m,S} G_C \\ & + 2p^2 (C_{m,S} - pC_{m,S} - pC_{m,D}) C_{m,S} G_{m,D} G_C + (1-p)^2 p^2 G_{m,S}^2 C_{m,D}^2 + (1-p)^2 G_C^2 C_{m,D}^2 \\ & + p^2 \left\{ (1-p)^2 G_{m,D}^2 + G_C^2 \right\} C_{m,S}^2 + 2p(1-p)^2 G_{m,S} C_{m,D}^2 G_C \end{aligned}$$

Given that the system time constant is a predetermined passive system property, the inverse equation for the $C_{m,S}$ was derived from Equation (4-15) in the form of,

$$C_{m,S} = \frac{\tau_m \left\{ p(1-p)\tau_m G_{m,S} G_{m,D} + pG_{m,S} (\tau_m G_C - C_{m,D}) + P^2 G_{m,S} C_{m,D} + (1-p) (\tau_m G_C G_{m,D} - G_C C_{m,D}) \right\}}{p \left\{ (1-p) (\tau_m G_{m,D} - C_{m,D}) + \tau_m G_C \right\}} \quad (4-17)$$

It should be noted that the $C_{m,S}$ must be lastly determined in the DC/AC-RM because it includes all passive membrane parameters ($G_{m,S}$, $G_{m,D}$, G_C and $C_{m,D}$).

4.3.3 Frequency response of reduced neuron models

To validate the new reduced modeling approach and determine if explicitly adding AC frequency response added features compared to the DC-RM, the frequency response of the DC/AC-RM was compared to the corresponding anatomical motor neuron model (V1 in Table 4-1) and DC-RM at the same distance from the soma ($D_{\text{path}} = 300 \mu\text{m}$), for signal frequencies that were not used in developing the new modeling framework.

Starting with equation (4-10) and adding the passive electrotonic properties we rewrite the equation as a general first-order transfer function,

$$VA_{SD}(s) = \frac{K}{\tau s + 1} \quad \text{where } K = \frac{G_C}{G_C + G_{m,D}(1-p)}, \quad \tau = \frac{C_{m,D}(1-p)}{G_C + G_{m,D}(1-p)} \quad (4-18)$$

Evaluating equation (4-18) at $s=j\omega_f$, the frequency response of the first-order system is described by the well known amplitude and phase equations,

$$|VA_{SD}(j\omega_f)| = \frac{K}{\sqrt{1 + (\omega_f\tau)^2}}, \quad \angle VA_{SD}(j\omega_f) = \arctan\left(-\frac{\omega_f}{\tau}\right) \quad (4-19)$$

As ω_f in Equation (4-19) increases from zero to infinity, the magnitude of $VA_{SD}(j\omega_f)$ decreases from a value of $K=1$ to zero and the phase lag increases from 0 to $-\pi/2$ radians. This analytical estimation of the frequency-response was simulated for both DC-RM ($C_{m,S}=C_{m,D}=C_m$) and DC/AC-RM ($C_{m,S}\neq C_{m,D}$), and compared to their corresponding anatomical model (V1 in Table 4-1) at different input signal frequencies (ω_f).

Figure 4-2a clearly shows that the frequency response of the DC/AC-RM is much closer to the physiological response directly measured from the anatomical model, compared to the DC-RM. At the frequencies used to characterize the DC/AC-RM ($\omega_f = 0$ and 250 Hz), the amplitude attenuation was the same in the DC/AC-RM and anatomical model as expected. However the phase lag, which was not included in the development of the DC/AC-RM, was different. The DC/AC-RM had a phase delay that was 0.11π radians greater than in the anatomical case. Amplitude was more attenuated in the anatomical model for frequencies less than 250 Hz but less attenuated above this frequency. The differences in attenuation were greatest at 100 and 700 Hz (not shown). Similarly the phase lag between the DC/AC-RM and anatomical model was same at 75 Hz. Phase was more delayed in the anatomical model for frequencies less than 75Hz but less delayed above this frequency. The differences in phase were maximized at 30 and 500 Hz by 0.04π and 0.12π radians. The frequencies maximizing the differences in frequency response were at least two times bigger or less than the characteristic frequency (i.e. 250 Hz).

Figure 4-2a also shows that the DC/AC-RM retaining the physiological AC signaling property transfers much larger amplitude of action potentials than the DC-RM. At $\omega_f = 250$ Hz, the amplitude attenuation was seven times less in the DC/AC-RM ($VA=0.49$) than the DC-RM ($VA=0.07$). This result gave us a

critical prediction that the dendrite of the DC/AC-RM might become more excitable due to its better transmission of AC signal amplitude than the DC-RM, leading to the more facilitation of the PIC channel activation in the dendrite.

In Figure 4-2b, the overall trend of frequency response (i.e. Nyquist plot) of the DC/AC-RM was compared to that of the complex anatomical model over the broad frequency range between 0 to infinity. The similarity in the shape of vector curve and the location of data points between two models supports that the physiological frequency response at particular distance from the soma may be represented by the first-order reduced dendritic system (indicated by gray graph).

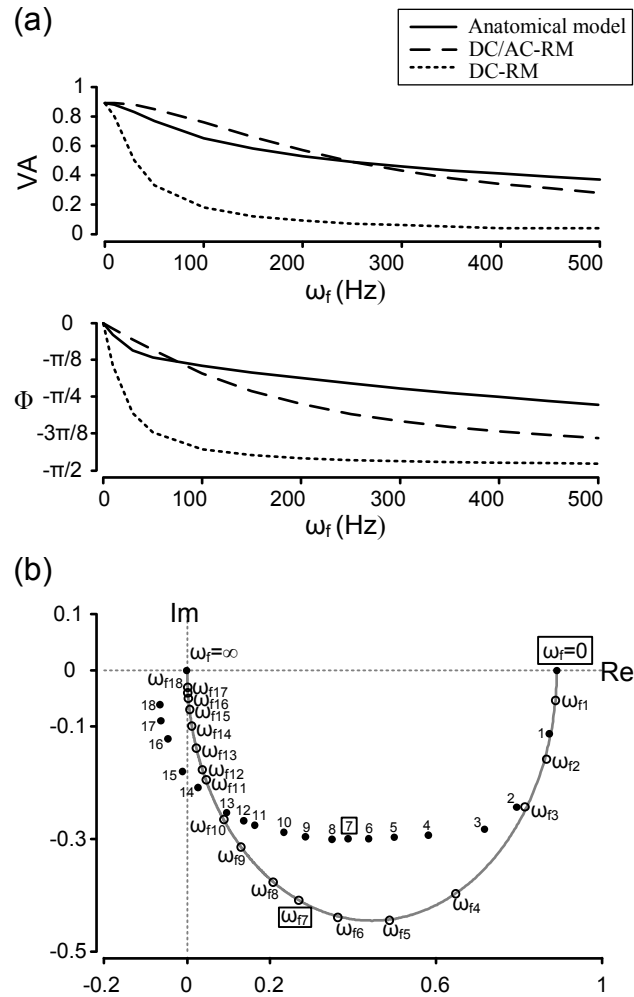


Figure 4-2. Comparison of the frequency response between the DC/AC-RM, DC-RM and anatomical motor neuron model. (a) Bode plot: amplitude (VA) and phase (Φ) response as a function of input signal frequency (ω_f). (b) Nyquist plot: integrated representation of frequency response in the complex domain consisting of Imaginary (Im) and Real (Re) axis. The overall frequency response of the DC/AC-RM and anatomical model is outlined with blank and filled black circles. The positions of the individual data points (i.e. both black circles) in the complex domain were calculated for the eighteen frequencies sampled between $\omega_f=0$ to infinity: $\omega_{fi} = \{10, 30, 50, 100, 150, 200, 250, 300, 400, 500, 700, 800, 1000, 1500, 2000, 3000, 4000, 5000\}$, where $i=1$ to 18. The frequencies for the anatomical case were indicated only by i . The gray graph represents the frequency response of the DC/AC-RM for the continuous frequency vector. The frequencies

for DC ($\omega_f=0$) and characteristic AC ($\omega_f=250\text{Hz}$) signals are highlighted with squares.

4.3.4 *Bistability of the reduced model with AC signaling property of the dendrites*

To determine if the DC/AC-RM produced the bistable firing patterns similar to the DC-RM we evaluated the firing response to triangular and current pulse inputs. Both current input protocols have been used extensively in experimental and computational studies on motor neuron bistability (Booth and Rinzel, 1995; Hounsgaard and Kiehn, 1989; Hounsgaard et al., 1988b). The triangular current stimulation has been used to demonstrate the counterclockwise frequency-current hysteresis as well as the sustained firing behaviour in the bistable motor neurons, whereas the alternating current pulses have been used to show the bistable state transitions in the steady-state condition.

4.3.4.1 Hyperexcitable dendrite in the DC/AC-RM

Having compared the frequency response between the DC/AC-RM, DC-RM and anatomical model with the fixed distance (i.e. $D_{\text{path}}=300$), we showed that the AC signal attenuation factor (i.e. $VA_{\text{SD}}^{\text{AC}}$) was seven times larger in the DC/AC- than DC-RM. To produce bistable firing patterns, we first assigned same kinetics and values of all active membrane parameters used in the DC-RM to the DC/AC-RM. However the PIC channels in the dendrite were simultaneously activated with firing at the soma, leading to the Type III firing (i.e. no frequency hysteresis with sustained firing behaviour). There was no way but to add the time constant to the activation kinetics of PIC channels in the dendrite to delay the onset timing of plateau potentials for the fully bistable firing pattern (or Type IV). Otherwise net inward current in the subthreshold region for the dendritic plateau potential had to be vanished, which is not physiologically plausible (Schwindt and Crill, 1980b; Schwindt and Crill, 1980c). This result indicates that the variations of AC signal attenuation may affect the dendritic excitability resulting in the changes in current threshold and onset timing of the plateau potential.

4.3.4.2 Bistable firing patterns

Figure 4-3(a) illustrates the firing response of the DC/AC-RM to triangular current injection. As the current stimulation to the soma increased, the somatic membrane potential (V_S) depolarized and then initiated a repetitive spikes followed by a jump to a higher firing frequency. This frequency jump was attributed to the activation of the plateau potential mediated by the PIC channels in the dendrite. The higher firing frequency associated with the PICs sustained during the descending phase of current stimulation. This nonlinear firing behaviour clearly appeared as the counter-clockwise frequency hysteresis in the frequency-current domain (Figure 4-3(b)), which has been considered as an indicator for the bistability of the motor neurons. For the fully bistable firing (or Type IV firing) as shown in Fig. 4-3(a), three characteristic indexes (CIs) indicating the presence of the model bistability were all positive: *Time To onset of Plateau potential* (TTP) had a positive value since somatic spiking preceded the dendritic plateau onset. As the stimulation decreased toward the value of current threshold determined on the upward phase, the firing frequency remained elevated resulting in a positive *Difference in Spiking Frequency* (DSF). As the current stimulation continued to decrease, the model continued to fire well past the current threshold resulting in a positive value for *Time to End of somatic Spiking* (TES).

Figure 4-3(c) demonstrates that the model can produce two types of the bistable switching behaviour at the same level of steady current stimulation to the soma. At the default steady current level, the transition between the resting state (or stable equilibrium point) and repetitive firing state (or stable limit cycle) was induced by applying brief depolarizing and hyperpolarizing current pulses. Likewise, the switch-on and -off of the higher frequency firing state from the lower frequency firing state were evoked by short depolarizing and hyperpolarizing current pulses over the depolarized steady current level.

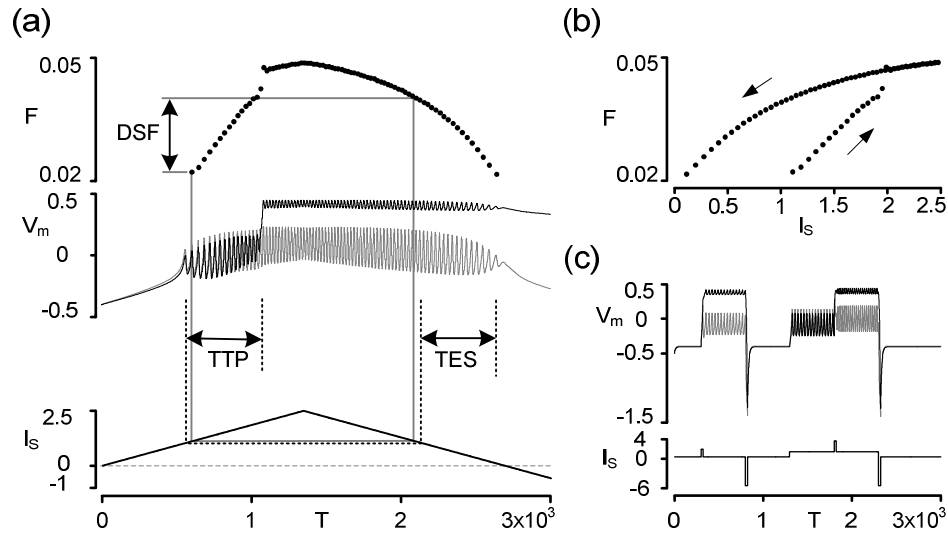


Figure 4-3. Bistable firing behaviour of the DC/AC-RM. (a). Time course of membrane potentials (gray line for somatic and black line for dendritic compartment in the middle) during the triangular current stimulation to the soma (bottom) and their instantaneous frequencies (top). Three characteristic indexes for detecting the model bistability: Time To onset of Plateau potential (TTP), Time to End of somatic Spiking (TES) and Difference in Spiking Frequency (DSF). (b) The hysteretic relationship of the frequency responses to current stimuli for the case of (a). (c). Switching behaviour of membrane potentials (solid gray line for somatic and solid black line for dendritic compartment) under the briefly depolarizing and hyperpolarizing current stimulation protocol (bottom).

4.3.5 *Dependence of the reduced model dynamics on dendritic AC signaling property*

4.3.5.1 Insights from bifurcation analysis

Figure 4-4 shows the positive correlation of the AC signal attenuation (i.e. VA_{SD}^{AC}) to the dendritic excitability which was indirectly evaluated by the current threshold in the soma ($I_{S,TH}$ indicated by gray line with arrow) for the plateau potential in the dendrite. When VA_{SD}^{AC} decreased by six times less than the default value (i.e. $VA_{SD}^{AC}=0.49$), the $I_{S,TH}$ increased by about 1.8 times larger than the initial $I_{S,TH}$ (i.e. $I_S=2$). In contrast, when VA_{SD}^{AC} increased by 1.7 times larger than the default VA_{SD}^{AC} , the $I_{S,TH}$ decreased by about 0.8 times less than the initial $I_{S,TH}$. Since the input resistance in the soma ($R_{N,S}$) was a constraint to the DC/AC-RM, the constant slope of V_S-I_S line in the subthreshold region in Fig. 4-(a1) to 4-(a3) was expected. Similarly the input resistance in the dendrite ($R_{N,D}$, indicated by the slope of V_D-I_D line in Fig. 4-(b1) to 4-(b3)) could be expected to be constant in the subthreshold region by the relationship derived by Kim and Jones (2010) (i.e. $R_{N,D}=R_{N,S}*VA_{SD}^{DC}/VA_{DS}^{DC}$). However the current threshold (i.e. rheobase) for the spiking at the soma was insensitive to changes in the AC signaling properties, which indicates that the rheobase might be independent of dendritic signaling properties (i.e. VA_{SD}^{DC} , VA_{DS}^{DC} and VA_{SD}^{AC}) in the DC/AC-RM. The results of bifurcation analysis gave us the critical prediction that the solution space for the bistable firing behaviour of the DC/AC-RM will be constrained by all three signal propagation properties of the dendrites that give rise to appropriate dendritic excitability for plateau potentials in the dendritic compartment.

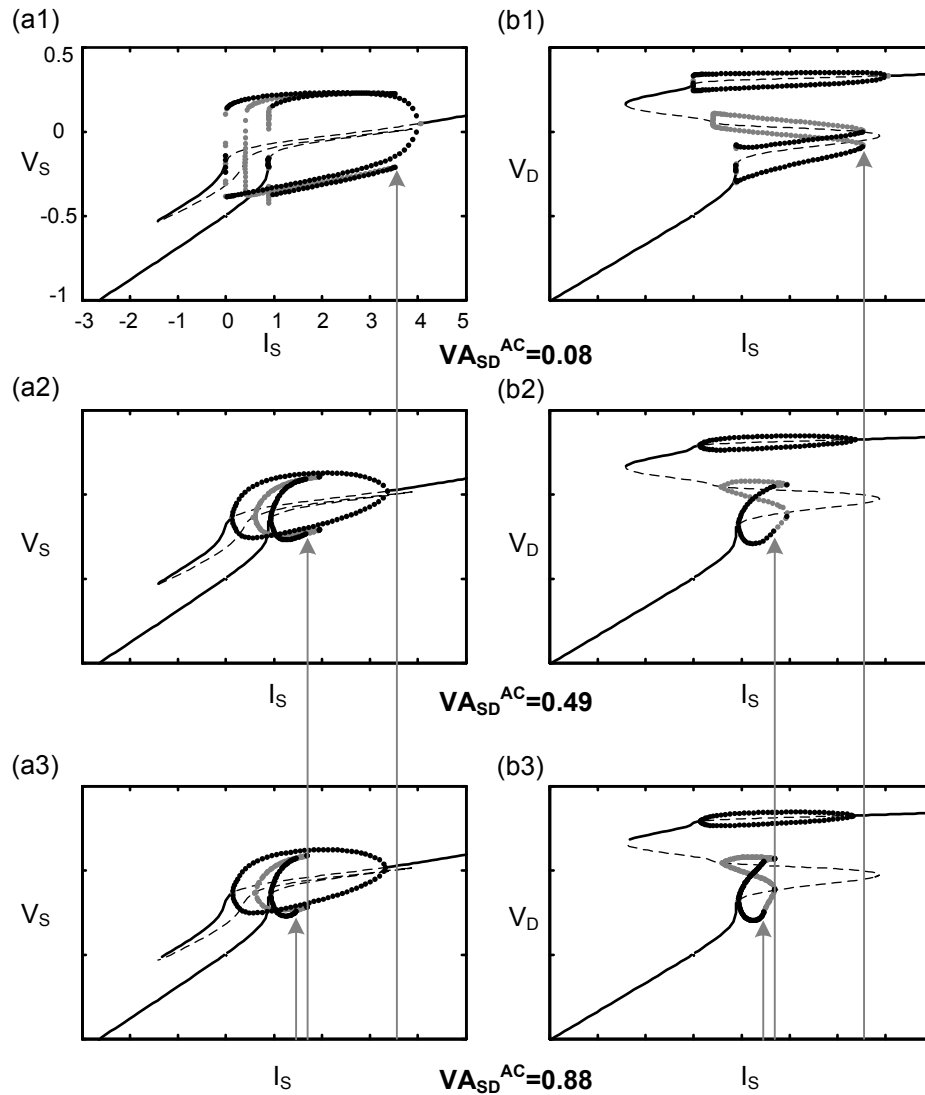


Figure 4-4. Bifurcation structures at the soma (left column) and dendrite (right column) of the DC/AC-RM with increasing AC signal attenuations ($V_{ASDAC} = 0.08, 0.49$ and 0.88) and constant DC signal attenuations ($V_{ASDDC}=0.89$ and $V_{ADSDC}=0.26$). The left and right columns show changes of the membrane potential in the somatic (V_S) and dendritic (V_D) compartment, with the steady current injection to the soma (I_S). For all figures, the stability of fixed points was indicated by black solid line for the stable state and black dashed line for the unstable state. Both stable (black filled circles) and unstable (gray filled circles) limit cycles were outlined with maximum and minimum amplitudes of membrane

potential oscillation. The gray solid lines with arrows indicate the current intensity at which the plateau potential is evoked. Note that somatic spiking is initiated at the same bifurcation point regardless of changes in VA_{SD}^{AC} , and the slope of the V_S-I_S and V_D-I_S curves in the subthreshold region are constant. All model parameters (refer to Method) were held constant, but membrane capacitances were systematically changed according to VA_{SD}^{AC} values: $C_{m,S}=\{19.944, 53.103, 54.583\}$ and $C_{m,D}=\{2.851, 0.39, 0.039\}$, where values in curly braces are in the increasing order of VA_{SD}^{AC} .

4.3.5.2 Bistable solution space

Figure 4-3 showed that all CIs were positive in the DC/AC-RM at the default values of three dendritic signaling properties ($VA_{SD}^{DC}=0.89$, $VA_{DS}^{DC}=0.26$, $VA_{SD}^{AC}=0.49$). To investigate the influence of the dendritic AC signaling on the model bistability, we systematically varied three voltage attenuation values that were independently parameterized in the DC/AC-RM. Evaluating the CIs as a function of the three voltage attenuations, we identified the solution parameter space where the model produced the fully-bistable firing behaviour. The firing patterns outside the bistable solution space were qualitatively similar to the DC-RM dynamics.

Figure 4-5(a) shows the distribution of bistable solution points in the three-dimensional voltage attenuation parameter space. The overall solution parameter sets were rather one-sided to the region in the upper left corner of the VA_{SD}^{DC} – VA_{SD}^{DC} plane where VA_{SD}^{DC} is larger than VA_{DS}^{DC} . This result was attributed to the dependency of the dendritic input resistance on DC signaling properties: $R_{N,D}=R_{N,S}*VA_{SD}^{DC}/VA_{DS}^{DC}$. To generate bistable firing the DC/AC-RM must have sufficiently large input resistance in the dendrite that is directly proportional to VA_{SD}^{DC} and inversely to VA_{DS}^{DC} .

However the horizontal cross-section areas of the solution volume dramatically changed as a function of VA_{SD}^{AC} . Fig. 4-5(b) illustrates the variations of location and size of horizontal solution space at three representative values of VA_{SD}^{AC} (i.e. 0.07, 0.21 and 0.73). The cross-section area was maximized at around $VA_{SD}^{AC}=0.73$ and minimized at both vertical ends of the solution volume ($VA_{SD}^{AC}=0.01$ for the lower and 0.99 for the upper). The shift in the location of horizontal solution spaces indicates that the dendritic AC signaling property (i.e. VA_{SD}^{AC}) is tightly correlated to the dendritic excitability that determines the activation of plateau potentials responsible for the bistable firing behaviour. In addition, the exponential increase of the horizontal cross-section areas as a function of VA_{SD}^{AC}

indicates that the VA_{SD}^{AC} is also crucial to stabilize the model bistability against changes in DC signal propagation properties (i.e. VA_{SD}^{DC} and VA_{DS}^{DC}).

The insets of Fig. 4-5(a) in the right of Fig. 4-5(b) show the systematic changes in the bistable firing patterns within the bistable solutions space. Six representative firing patterns were sampled along the boundary of the bistable solution volume. As VA_{SD}^{AC} increased from point a1 ($VA_{SD}^{AC} = 0.21$) to a2 ($VA_{SD}^{AC} = 0.87$), the frequency hysteresis significantly decreased due to the early onset of plateau potential indicated by the arrow in the inset of a2. Similarly, the increase of VA_{SD}^{DC} from b1 (0.85) to b2 (0.95) and the decrease of VA_{DS}^{DC} from c2 (0.39) and c1 (0.11) resulted in the almost simultaneous activation of somatic spiking with dendritic VGICs responsible for the plateau potential. These results show that all parameter sets within the solution volume in Fig. 4-5(a) can produce the fully-bistable firing behaviour as shown in Fig. 4-3. However the current threshold (i.e. rheobase indicated by arrows) for the spike initiation was constant in all six frequency (F)–current (I) relationships ((a1)–(c2) of Fig. 4-5(a)), which indicates that the rheobase in the DC/AC-RM might be independent of all voltage attenuation parameters (i.e. VA_{SD}^{AC} , VA_{SD}^{DC} and VA_{DS}^{DC}).

Similar to the DC-RM (see Fig. 3-5 in Chapter 3), three types of firing behaviours were identified outside the solution space based on F-I curve during triangular current stimulation (Bennett et al., 2001): 1) Type I (linearly overlapping F-I relationship without sustained firing) or II (clockwise F-I relationship with firing rate adaptation) firing in the space below a1 and b1 without the activation of plateau potentials, 2) Type III firing (linearly overlapping F-I relationship with sustained firing) in the space left of c2 and upper of b2 with simultaneous activation of plateau potentials with firing, and 3) the synchronized firing between the somatic and dendritic compartments in the space right of c1 including partially bistable firing with the activation of plateau potential that was turned off in the descending phase of current stimulation prior to approaching the current threshold for the firing in the ascending phase.

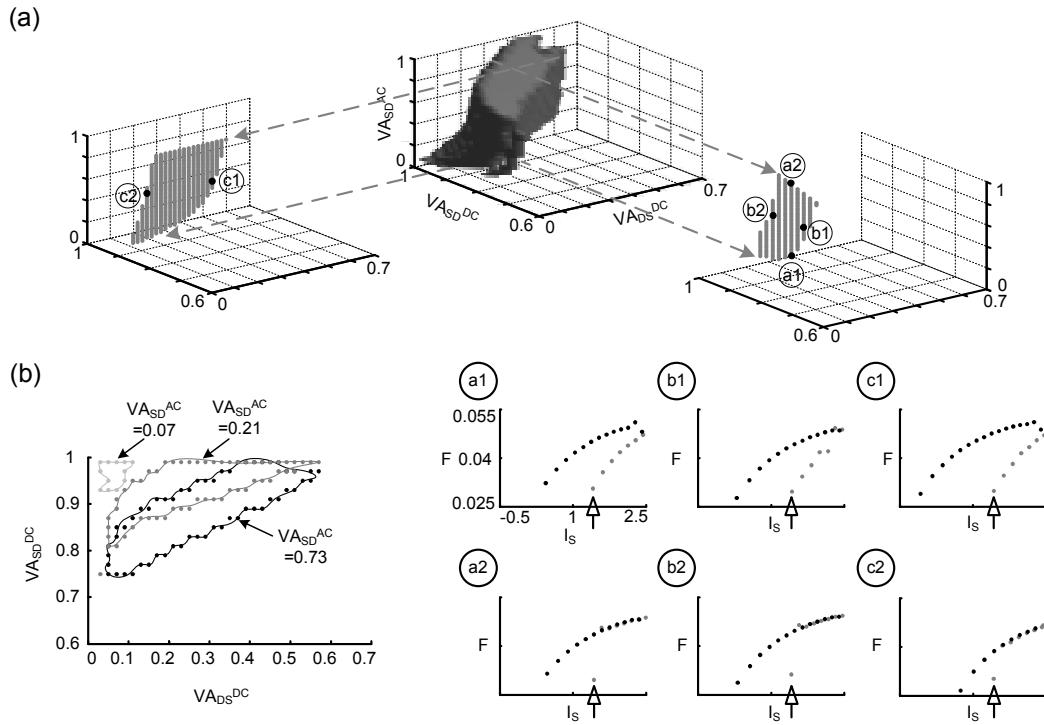


Figure 4-5. Bistable solution space of the DC/AC-RM. (a). The solution parameter sets for the fully bistable firing behaviour of the DC/AC-RM were volumized with gray patches in the three-dimensional parameter space (VA_{SD}^{DC} , VA_{DS}^{DC} and VA_{SD}^{AC}). Two representative cross section areas of the solution volume at $VA_{SD}^{DC}=0.89$ (for left gray dots) and $VA_{SD}^{DC}=0.26$ (for right gray dots) were plotted in separate insets indicated by gray dashed arrows. Six representative solution points (a1–a2, b1–b2 and c1–c2) were selected along the boundary of two cross section areas for showing the fully bistable firing patterns. Circled numbers in six frequency (F)–somatic current (I_s) relationships correspond to the boundary points at each cross section of the solution volume. Black arrows indicate the current threshold for initiating the spike. (b). Cross sectional areas at different levels of amplitude attenuation of the AC signal (VA_{SD}^{AC}) on the VA_{SD}^{DC} – VA_{DS}^{DC} plane.

4.3.6 *Spatial relationship of the bistable solution space*

The results from Fig. 4-5 showed that the DC/AC-RM had a large bistable solution space that expanded well beyond the default values for voltage attenuation ($V_{ASD}^{DC}=0.89$, $V_{ADS}^{DC}=0.26$ and $V_{ASD}^{DC}=0.49$). The numerical simulations treated the three voltage attenuation properties as independent, however in physiologically based models the voltage attenuation properties are a function of distance from the soma, D_{path} in Fig. 4-1. To determine the spatial relationship between bistable solutions of the two-compartment model and anatomically determined voltage attenuation properties, we calculated voltage attenuation properties as a function of distance from five reconstructed motor neurons in Table 4-1. Figure 4-6 shows that the physiological voltage attenuation values of V1 existed within the solution space of corresponding DC/AC-RM. The distance where physiological voltage attenuation values for the anatomical model V1 was within the bistable solution space ranged from $D_{path}=125 \mu\text{m}$ at $V_{ASD}^{AC}=0.74$ to $D_{path}=630 \mu\text{m}$ at $V_{ASD}^{AC}=0.22$. This range of distances matches the hypothesized location of calcium PIC channels (at least 300–500 μm away from the soma) estimated in experimental (Ballou et al., 2006; Heckman et al., 2003) and theoretical studies (Carlin et al., 2000b; Elbasiouny et al., 2005; Grande et al., 2007). The starting point for the voltage attenuation properties of the DC/AC-RM was determined from anatomical model V1 at a distance of 300 μm from the soma. It should be noted that the physiological voltage attenuation values for V1 (S), V4 (FR) and V5 (FR) fully went through the solution space, but V2 (FF) and V3 (FF) were partially intercepted. This might imply the type dependency of the bistable firing behaviour of motor neurons (Lee and Heckman, 1998b). The coincident spatial relationship between voltage attenuation values derived from anatomical models and bistable solutions of the DC/AC-RM suggests that the ability of the reduced models to retain physiological AC signal propagation property (V_{ASD}^{DC}) may be important for modeling nonlinear dynamical behaviour of motor neurons.

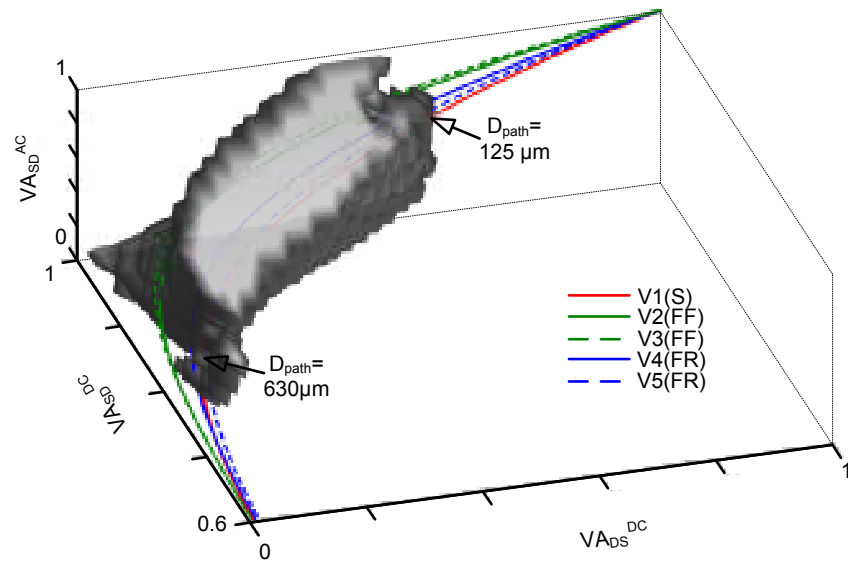


Figure 4-6. Coincidence of bistable solution space with physiological voltage attenuation properties. The bistable solution space of the DC/AC-RM is outlined by gray patches in the three dimensional parameter space consisting of V_{ASD}^{DC} , V_{ADS}^{DC} and V_{ADS}^{AC} . To determine the interception area, physiological voltage attenuation values calculated from anatomically reconstructed motor neurons (V1–V4, V6 in Table 4-1) were superimposed on the same solution space using the various types of lines with different colors. The lines of physiological voltage attenuation values started from the point of ($V_{ASD}^{DC}=1$, $V_{ADS}^{DC}=1$, $V_{ADS}^{AC}=1$) and ended at the point of ($V_{ASD}^{DC}=0.6$, $V_{ADS}^{DC}=0$, $V_{ADS}^{AC}=0.04$) as a function of the distance from the soma up to maximum dendritic terminal. The arrows indicate the boundary points of intersection between the solution space and physiological voltage attenuations of the anatomical model V1.

4.4 DISCUSSION

We demonstrated how the AC signals like action potentials propagating into the dendrites influence the bistable firing output of reduced motor neuron models. The AC signaling property characterized from the frequency response analysis of the dendrites was found to be an essential biophysical parameter to determine the dendritic excitability for generating plateau potentials. The onset timing of the plateau potentials and the solution space (i.e. robustness) for the model bistability were tightly correlated to the degree of the AC signal attenuation, as well as DC signaling. This result supports that at least three dendritic signaling properties (i.e. V_{ASD}^{DC} , V_{ADS}^{DC} and V_{ADS}^{AC}) should be considered in reduced neuron modeling to produce the physiological neuron bistability.

4.4.1 *Passive versus active propagation of action potentials in motor neurons*

To our knowledge, it is not still clear whether the action potentials propagate passively or actively into the dendrites of spinal motor neurons in adult mammalian animals. But using the organotypic preparation of rat spinal cord neurons, Larkum and his colleagues (1999) have suggested that some of dendritic trees of ventral horn neurons may have voltage-gated Na^+ channels that may mediate the active back-propagation of action potentials and the activation of Ca^{2+} influx. However, their spinal neurons seem to be very different from those of the adult motor neurons in vivo in terms of the signal propagation properties between the soma and dendrites. The amplitude attenuation of the AC signal propagating anatomically reconstructed passive dendrites of cat motor neurons (Fig. 4-1) turned out to be similar to that of actively propagating action potentials experimentally observed from the rat ventral horn neurons up to the distance of 450 μm from the soma. Furthermore the voltage attenuations of anatomically reconstructed motor neurons have been shown to be different from those of ideal passive cable models that they used to estimate passive back-propagation of action potentials (Kim et al., 2009). Thus it might be possible that the action

potentials passively propagate until interacting with PIC channels concentrated on the dendrites away from the soma by about 300–500 μm . Alternatively, if adult motor neurons propagate action potentials actively (i.e. larger $V_{A_{SD}}^{AC}$), the robustness of the bistable firing behaviour (defined by the size of solution space in Fig. 4-5(b)) might become significantly improved. Further experimental measurements are required for the clarification of this issue in mammalian motor neurons in the spinal cord. The physiological effects of the back-propagating action potentials on the activation of dendritic VGIC channels may be indirectly measured by comparing the current threshold for the plateau potentials with to without spike blockers (e.g. TTX or QX314) in the same cell.

4.4.2 Retrograde signaling of action potentials for short-term plasticity

It has been suggested that the facilitation of L-type Ca^{2+} channels generating plateau potentials is essential to evoke the use-dependant plasticity in the dendritic integration of synaptic inputs in the turtle motor neurons (Svirskis and Hounsgaard, 1997). In their experiments using current pulses to the soma, the voltage threshold for the spike was typically lower than that for the plateau potentials. Thus the action potentials generated at the soma were likely to propagate into the dendrites and interact with L-type Ca^{2+} channels, which implies that the facilitation of Ca^{2+} channels underlying dendritic short-term plasticity might be significantly influenced by the dendritic signaling properties for the back-propagating action potentials. This inference supports that the dendritic propagation property for both DC and AC signals is a critical factor influencing not only the bistable firing outputs but also the dendritic processing of various synaptic inputs, based on the same mechanism of varying the facilitation effects (also called ‘warming up’) on the L-type Ca^{2+} channel in the dendrites.

4.4.3 Type-dependency of AC signal attenuation property

Motor neurons have been classified into three groups based on mechanical properties of muscle fibers that they innervate: Slow-twitch (S)-, Fast-twitch fatigue-resistant (FR)- and Fast-twitch fatigable (FF)-type. It has been suggested that the morphological properties of the dendrites may be related to the motor neuron types (Cullheim et al., 1987a; Cullheim et al., 1987b). Thus the dendritic AC signaling property might depend on the motor neuron type-related morphology. In order to resolve this issue, we reconstructed six type-identified anatomical dendrites. For each type-specific morphology, voltage decay coefficient (η) was calculated fitting the amplitude response of the dendrites (Fig. 4-1(b)) to a single exponential function while varying the cell input resistance from 0.4 to 4.0 M Ω . Figure 4-7 showed that η values were not clustered into a specific motor neuron type at the same input resistance, suggesting that the AC signal attenuation might not be type-specific, rather genetic. However more samples of type-identified motor neuron models might be needed to clarify the inconclusive result.

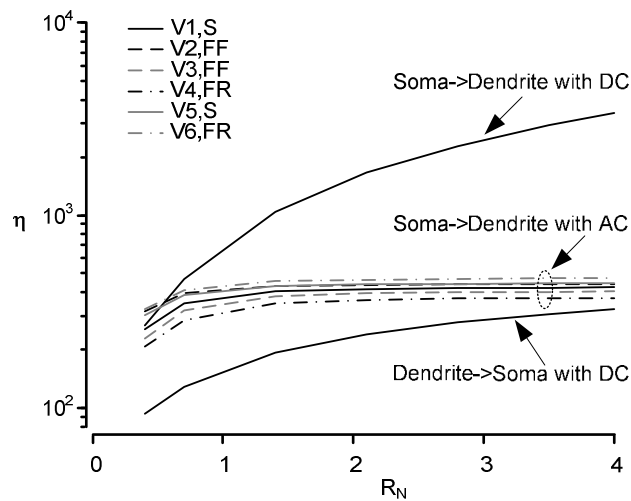


Figure 4-7. Relationship between the exponential decay coefficient (η) of the amplitude attenuation and input resistance (R_N) for six type-identified anatomical motor neuron models. η for the AC signal was plotted in the middle on R_N values ranged from 0.4 to 4.0 M Ω for the soma-to-dendrite direction. The scattered distribution of different line types indicates no clustering by motor neuron types. Note that the relationship between η and R_N is significantly between transient and steady-state signal cases for both directions.

4.4.4 *Comparison with other studies*

Previous computational studies on the signal propagation properties of the dendrites have been focused on understanding how effectively the synaptic effects evoked in the dendritic branches contribute to the generation of action potentials in the soma (Jaffe and Carnevale, 1999; Rall and Rinzel, 1973; Rinzel and Rall, 1974). Many efforts have been made on showing the functional roles of retrograde signaling of action potentials that actively propagate by the various voltage-gated channels over the dendritic trees of pyramidal neurons in the brain (Hausser et al., 2000; Larkum et al., 1999; Stuart et al., 1997). However the dendritic AC signaling properties have not been explicitly investigated in the spinal motor neurons. As far as we know, we are the first to characterize the frequency response of the fully reconstructed motor neuron dendrites with empirically determined cable properties and developed the analytical method to map both DC and AC signaling properties of the anatomically reconstructed dendrites into the two-compartment modeling domain.

The new reduced modeling framework (i.e. DC/AC-RM) was directly expanded from the previous physiological two-compartment modeling (i.e. DC-RM) that can capture the DC signal propagation properties for both directions (i.e. from the soma to dendrites and vice versa). The main difference in system equations was the non-uniform membrane capacitances (Equation (4-3) & (4-4)) in the new model. The membrane capacitance at the dendrite in the new modeling framework turned out to influence not only the AC signal attenuation (Equation (4-12)), but also the membrane capacitance at the soma (Equation (4-17)). Thus the membrane capacitance at the soma was ten times larger in the DC/AC-RM than in the DC-RM, resulting in three times less in the initial firing rate in the DC/AC-RM case where the dendritic AC signaling was specifically reflected. If considering appropriate units (e.g. ms for time in Figure 4-3), the initial firing rate (i.e. 20 Hz) of the expanded model was more close to the physiological range. This result

supports that reflecting the dendritic AC signaling property is also essential to constrain the shape of the action potentials in the reduced modeling framework.

In order to produce bistable firing patterns in the new reduced modeling framework, we first applied Morris-Lecarr membrane excitability that are mediated by instantaneously activated inward currents and slowly activated outward currents. Unlike in the DC-RM the instantaneous activation of L-type Ca^{2+} channels in the dendrites could not generate the delayed onset of plateau potential which is essential for the fully bistable firing, without adding the time constant to the activation kinetics of dendritic L-type Ca^{2+} channels. In fact, the experimental and computational studies have suggested the slow kinetics of persistent inward currents mediated by L-type Ca^{2+} channels in the dendrites for the motor neuron bistability (Carlin et al., 2000a; Carlin et al., 2000b; Li and Bennett, 2003; Powers, 1993; Svirskis and Hounsgaard, 1997). Thus reflecting the dendritic AC signaling properties in the reduced modeling framework resulted in realistically constraining the kinetics of L-type Ca^{2+} channels, leading to the generation of the physiological bistable firing behaviour.

Owing to the uniformity of membrane capacitance (i.e. $C_m = C_{m,S} = C_{m,D}$) in the DC-RM, the soma-to-dendrite AC voltage attenuation was arbitrarily determined depending on passive membrane parameters (G_C , $G_{m,S}$ and $G_{m,D}$). It turned out that the default value of soma-to-dendrite AC voltage attenuation (VA in Fig. 4-2(a)) in the DC/AC-RM was seven times larger than in the DC-RM case. Although the direct comparison of the solution space between two cases is difficult, it was obvious that the size of solution space in the DC/AC-RM significantly varied according to the level of the AC amplitude attenuation. In Figure 4-5(b), the solution space size at $V_{A_{SD}}^{AC}=0.07$ (initial value in the DC-RM) was almost ten times less than at $A_{SD}^{AC}=0.49$ (initial value in the DC/AC-RM). The physiological value of the dendritic AC signal property significantly improved the robustness of the model bistability. This result implies that the actively back-propagating action potentials might further contribute to stabilize

the bistable firing behaviour of motor neurons against changes in electrical structure of the dendrites.

4.4.5 Limitations in current modeling approach

The biophysical parameters of dendritic signaling properties (Fig. 4-1(b)) for the realistic two-compartment modeling were measured as a function of the path length (i.e. D_{path}) between the soma and individual points over the dendrites where VGICs were assumed to be placed. However the VGICs could be uniformly distributed over all points of the dendrites that are separated by the same distance from the soma, then might differently alter the bistable firing patterns. The main difference between two distribution conditions, one and all dendritic points, is the amount of effective PIC currents approaching the soma that are mediated by dendritic VGICs. Due to the parallel structure of the dendritic trees, the influence of back-propagation action potentials on the activation of dendritic VGICs can be identical regardless of the between two cases. Therefore this assumption seems to be reasonable for the theoretical purpose of this study in terms of the bistability of the reduced model.

The specific membrane capacitance at the dendrite ($C_{m,D}$) was determined as a function of the coupling conductance (G_C), dendritic membrane conductance ($G_{m,D}$), morphological factor (p), and soma-to-dendrite AC voltage attenuation (VA_{SD}^{AC}) in the DC/AC-RM (Equation (4-13)). In order to get real values of $C_{m,D}$, the inside of the square root in Equation (4-13) should be positive and thus the necessary and sufficient condition is,

$$\frac{G_C}{G_C + G_{m,D}(1-p)} = VA_{SD}^{DC} > VA_{SD}^{AC} \quad (4-20)$$

Although this condition may limit the robustness of our inverse methods, it appears to be the intrinsic property of the complex dendritic systems: the soma-to-

dendrite DC voltage attenuation is less than the AC case (Fig. 4-1(b)). This signal-dependant inequality of signal propagation from the soma to dendrites has been graphically demonstrated in the electrotonic space where the length of the dendritic branches representing the signal attenuation was longer for AC than for DC signal (Carnevale et al., 1997). Thus the new reduced modeling would not be appropriate when the AC signals actively propagate into the dendrites so that V_{ASD}^{DC} is less than V_{ADS}^{AC} . In this case, the associated active membrane mechanisms should be considered additionally.

While the Morris-Lecar formulation of active membrane mechanisms is convenient for qualitative analysis of dynamics, it is too simplified to capture all aspects of physiological spike shape mediated by specific motor neuron ion channel physiology (Carlin et al., 2000b; Hounsgaard and Mintz, 1988; Lee and Heckman, 1999b; Li and Bennett, 2003; Schwindt and Crill, 1980c). However lumped description of inward and outward currents was sufficient for the purpose of the present theoretical study: to determine if the dendritic AC signaling property is important in generating nonlinear dynamics of motor neurons.

4.5 CONCLUSION

To our knowledge, this is the first frequency response analysis of the passive dendritic trees in spinal motor neurons. The degree of the amplitude attenuation of the AC signals (i.e. action potentials) is a critical factor in forming and stabilizing the physiological bistable firing behaviour in the reduced neuron models.

4.6 APPENDIX A FOR CHAPTER 4

Forward and inverse equations for the DC-RM (Kim et al., 2009). The system equations are identical to the DC/AC-RM except for the uniform membrane

capacitance (i.e. $C_m=C_{m,S}=C_{m,D}$). Essential electrotonic properties that constrain the model parameters (i.e. $G_{m,S}$, $G_{m,D}$, C_m , G_C) are input resistance ($r_{N,S}$), system time constant (τ_m), and directional voltage attenuations (i.e. VA_{SD}^{DC} and VA_{DS}^{DC}) with the DC input. Note that forward equations for $r_{N,S}$, τ_m , VA_{SD}^{DC} and VA_{DS}^{DC} , and inverse equations for $G_{m,S}$, $G_{m,D}$ and G_C are not influenced in the DC/AC-RM to retain the amplitude attenuation of the AC signals (i.e. VA_{SD}^{AC}).

► Forward equations:

$$r_{N,S} = \frac{V_S}{I_S} = \frac{P}{G_C} \left(\frac{G_{m,S}}{G_C} P + \frac{G_{m,D}(1-p)}{G_C + G_{m,D}(1-p)} \right)^{-1} \quad (4-A1)$$

$$\tau_m = R_{\text{eff}} C_m \quad (4-A2)$$

$$R_{\text{eff}} = \frac{2P(P-1)}{\sqrt{G_C^2 + 2(G_{m,S} - G_{m,D}) \cdot (1-2P) \cdot (1-P)PG_C + (G_{m,S}^2 + G_{m,D}^2 - 2G_{m,S}G_{m,D}) \cdot (1-P)^2 P^2 + P(P-1)(G_{m,S} + G_{m,D}) - G_C}}$$

$$VA_{SD}^{DC} = \frac{V_D}{V_S} = \frac{G_C}{G_C + G_{m,D}(1-p)} \quad (4-A3)$$

$$VA_{DS}^{DC} = \frac{V_S}{V_D} = \frac{G_C}{G_C + G_{m,S}P} \quad (4-A4)$$

► Inverse equations:

$$G_{m,S} = \frac{1 - VA_{DS}^{DC}}{r_N(1 - VA_{SD}^{DC} VA_{DS}^{DC})} \quad (4-A5)$$

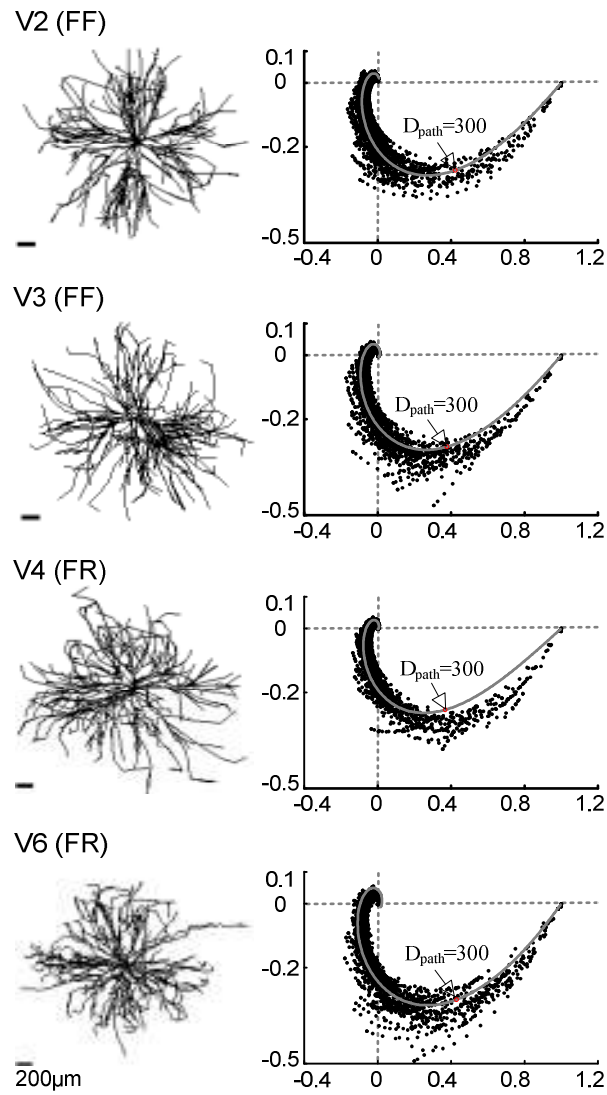
$$G_{m,D} = \frac{pVA_{DS}^{DC}(1 - VA_{SD}^{DC})}{(1-p)r_N VA_{SD}^{DC}(1 - VA_{SD}^{DC} VA_{DS}^{DC})} \quad (4-A6)$$

$$G_C = \frac{pVA_{DS}^{DC}}{r_N(1 - VA_{SD}^{DC} VA_{DS}^{DC})} \quad (4-A7)$$

$$\tau_m = R_{\text{eff}} C_m \quad (4-A8)$$

4.7 APPENDIX B FOR CHAPTER 4

Morphology and frequency response of four type-identified anatomically reconstructed motor neuron models in Table 4-1.



4.8 BIBLIOGRAPHY FOR CHAPTER 4

Ascoli, G. A. (2006). Mobilizing the base of neuroscience data: the case of neuronal morphologies. *Nat Rev Neurosci* 7, 318-324.

Ballou, E. W., Smith, W. B., Anelli, R., and Heckman, C. J. (2006). Measuring dendritic distribution of membrane proteins. *J Neurosci Methods* 156, 257-266.

Bennett, D. J., Li, Y., and Siu, M. (2001). Plateau potentials in sacrocaudal motoneurons of chronic spinal rats, recorded in vitro. *J Neurophysiol* 86, 1955-1971.

Booth, V., and Rinzel, J. (1995). A minimal, compartmental model for a dendritic origin of bistability of motoneuron firing patterns. *J Comput Neurosci* 2, 299-312.

Booth, V., Rinzel, J., and Kiehn, O. (1997). Compartmental model of vertebrate motoneurons for Ca²⁺-dependent spiking and plateau potentials under pharmacological treatment. *J Neurophysiol* 78, 3371-3385.

Brunel, N. (2003). Dynamics and plasticity of stimulus-selective persistent activity in cortical network models. *Cereb Cortex* 13, 1151-1161.

Carlin, K. P., Jiang, Z., and Brownstone, R. M. (2000a). Characterization of calcium currents in functionally mature mouse spinal motoneurons. *Eur J Neurosci* 12, 1624-1634.

Carlin, K. P., Jones, K. E., Jiang, Z., Jordan, L. M., and Brownstone, R. M. (2000b). Dendritic L-type calcium currents in mouse spinal motoneurons: implications for bistability. *Eur J Neurosci* 12, 1635-1646.

Carnevale, N. T., and Hines, M. L. (2005). *The NEURON book* (Cambridge ; New York: Cambridge University Press).

- Carnevale, N. T., Tsai, K. Y., Claiborne, B. J., and Brown, T. H. (1997). Comparative electrotonic analysis of three classes of rat hippocampal neurons. *J Neurophysiol* 78, 703-720.
- Coombs, J. S., Eccles, J. C., and Fatt, P. (1955). The electrical properties of the motoneurone membrane. *J Physiol* 130, 291-325.
- Cullheim, S., Fleshman, J. W., Glenn, L. L., and Burke, R. E. (1987a). Membrane area and dendritic structure in type-identified triceps surae alpha motoneurons. *J Comp Neurol* 255, 68-81.
- Cullheim, S., Fleshman, J. W., Glenn, L. L., and Burke, R. E. (1987b). Three-dimensional architecture of dendritic trees in type-identified alpha-motoneurons. *J Comp Neurol* 255, 82-96.
- Dechter, R. (2003). *Constraint processing* (San Francisco: Morgan Kaufmann Publishers).
- Egorov, A. V., Hamam, B. N., Franssen, E., Hasselmo, M. E., and Alonso, A. A. (2002). Graded persistent activity in entorhinal cortex neurons. *Nature* 420, 173-178.
- Elbasiouny, S. M., Bennett, D. J., and Mushahwar, V. K. (2005). Simulation of dendritic CaV1.3 channels in cat lumbar motoneurons: spatial distribution. *J Neurophysiol* 94, 3961-3974.
- Fleshman, J. W., Segev, I., and Burke, R. B. (1988). Electrotonic architecture of type-identified alpha-motoneurons in the cat spinal cord. *J Neurophysiol* 60, 60-85.
- Grande, G., Bui, T. V., and Rose, P. K. (2007). Estimates of the location of L-type Ca²⁺ channels in motoneurons of different size: a computational study. *J Neurophysiol* 97, 4023-4035.

- Hausser, M., Spruston, N., and Stuart, G. J. (2000). Diversity and dynamics of dendritic signaling. *Science* 290, 739-744.
- Heckman, C. J., Lee, R. H., and Brownstone, R. M. (2003). Hyperexcitable dendrites in motoneurons and their neuromodulatory control during motor behavior. *Trends Neurosci* 26, 688-695.
- Hounsgaard, J., and Kiehn, O. (1989). Serotonin-induced bistability of turtle motoneurons caused by a nifedipine-sensitive calcium plateau potential. *J Physiol* 414, 265-282.
- Hounsgaard, J., Kiehn, O., and Mintz, I. (1988). Response properties of motoneurons in a slice preparation of the turtle spinal cord. *J Physiol* 398, 575-589.
- Hounsgaard, J., and Mintz, I. (1988). Calcium conductance and firing properties of spinal motoneurons in the turtle. *J Physiol* 398, 591-603.
- Jaffe, D. B., and Carnevale, N. T. (1999). Passive normalization of synaptic integration influenced by dendritic architecture. *J Neurophysiol* 82, 3268-3285.
- Kim, H., and Jones, K. E. (2010). Asymmetric electrotonic coupling between the soma and dendrites alters the bistable firing behaviour of reduced models. *J Comput Neurosci*, DOI 10.1007/s10827-10010-10284-x.
- Kim, H., Major, L. A., and Jones, K. E. (2009). Derivation of cable parameters for a reduced model that retains asymmetric voltage attenuation of reconstructed spinal motor neuron dendrites. *J Comput Neurosci* 27, 321-336.
- Larkum, M. E., Rioult, M. G., and Luscher, H. R. (1996). Propagation of action potentials in the dendrites of neurons from rat spinal cord slice cultures. *J Neurophysiol* 75, 154-170.
- Larkum, M. E., Zhu, J. J., and Sakmann, B. (1999). A new cellular mechanism for coupling inputs arriving at different cortical layers. *Nature* 398, 338-341.

- Lee, R. H., and Heckman, C. J. (1996). Influence of voltage-sensitive dendritic conductances on bistable firing and effective synaptic current in cat spinal motoneurons in vivo. *J Neurophysiol* 76, 2107-2110.
- Lee, R. H., and Heckman, C. J. (1998a). Bistability in spinal motoneurons in vivo: systematic variations in persistent inward currents. *J Neurophysiol* 80, 583-593.
- Lee, R. H., and Heckman, C. J. (1998b). Bistability in spinal motoneurons in vivo: systematic variations in rhythmic firing patterns. *J Neurophysiol* 80, 572-582.
- Lee, R. H., and Heckman, C. J. (1999). Paradoxical effect of QX-314 on persistent inward currents and bistable behavior in spinal motoneurons in vivo. *J Neurophysiol* 82, 2518-2527.
- Li, W. C., Soffe, S. R., Wolf, E., and Roberts, A. (2006). Persistent responses to brief stimuli: feedback excitation among brainstem neurons. *J Neurosci* 26, 4026-4035.
- Li, Y., and Bennett, D. J. (2003). Persistent sodium and calcium currents cause plateau potentials in motoneurons of chronic spinal rats. *J Neurophysiol* 90, 857-869.
- Llinas, R., and Sugimori, M. (1980). Electrophysiological properties of in vitro Purkinje cell somata in mammalian cerebellar slices. *J Physiol* 305, 171-195.
- Morris, C., and Lecar, H. (1981). Voltage oscillations in the barnacle giant muscle fiber. *Biophys J* 35, 193-213.
- Phillips, C. L., and Harbor, R. D. (2000). *Feedback control systems*, 4th edn (London: Prentice Hall International).
- Powers, R. K. (1993). A variable-threshold motoneuron model that incorporates time- and voltage-dependent potassium and calcium conductances. *J Neurophysiol* 70, 246-262.

- Rall, W., and Rinzel, J. (1973). Branch input resistance and steady attenuation for input to one branch of a dendritic neuron model. *Biophys J* 13, 648-687.
- Rinzel, J., and Rall, W. (1974). Transient response in a dendritic neuron model for current injected at one branch. *Biophys J* 14, 759-790.
- Schwindt, P. C., and Crill, W. E. (1980a). Effects of barium on cat spinal motoneurons studied by voltage clamp. *J Neurophysiol* 44, 827-846.
- Schwindt, P. C., and Crill, W. E. (1980b). Properties of a persistent inward current in normal and TEA-injected motoneurons. *J Neurophysiol* 43, 1700-1724.
- Steriade, M. (1999). Coherent oscillations and short-term plasticity in corticothalamic networks. *Trends Neurosci* 22, 337-345.
- Stuart, G., Spruston, N., Sakmann, B., and Hausser, M. (1997). Action potential initiation and backpropagation in neurons of the mammalian CNS. *Trends Neurosci* 20, 125-131.
- Svirskis, G., and Hounsgaard, J. (1997). Depolarization-induced facilitation of a plateau-generating current in ventral horn neurons in the turtle spinal cord. *J Neurophysiol* 78, 1740-1742.

CHAPTER 5: GENERAL DISCUSSION

5.1 THESIS SUMMARY

The main goal of this thesis research was to investigate the roles of the dendrites in the input-output properties of MNs that retain active membrane mechanisms responsible for generating bistable firing behaviour. To derive biophysical principles underlying the MN bistability, the reverse-engineering approach was employed to directly map the essential biophysical parameters empirically measurable from the MNs into the reduced modeling framework, maintaining the traceability between the target MN and its corresponding reduced model based on the physical distance from the soma. As a result, the novel reduced modeling approach that retains the physiological signal propagation properties of the dendrites with DC input was developed in Chapter 2. Analyzing this modeling approach in Chapter 3, it was revealed that the dendritic excitability resulting from the directional signaling properties of the dendrites is a critical factor determining the bistable firing behaviour of the reduced MN model. Through the frequency response analysis of the dendrites in Chapter 4, the steady-state AC signaling like the action potentials propagating into the dendrites turned out to significantly facilitate the activation of the PIC channels, leading to changes in not only bistable firing patterns but also the robustness of the model bistability. All these results support that the complex dendritic signaling properties between the soma and dendrites play an essential role in determining and stabilizing the bistable firing behaviour of the MNs *in vivo*.

5.2 ASYMMETRIC SIGNALING IN DENDRITIC NEURONS

Since the concept of electrotonic distance ($X=x/\lambda$, x is a physical distance from the soma and λ is space constant) was first introduced in Rall's modeling framework (i.e. infinite cable modeling), X has been used in many literature as a convenient measure to represent how far one point on the dendritic branches is electrically separated away from the soma. However the degree of electrotonical separation between the soma and dendrites depends on the direction and type of the propagating signals. For instance, the electrotonic distance from the dendrites to soma was much longer than from the soma to dendrites. The electrotonic distance was more extended with the AC than DC inputs regardless of propagation direction. Thus the single variable X is not sufficient to represent the complex electrotonic structure of the complex dendritic systems. This issue is not new, but has been graphically emphasized by highlighting the signal-dependent electromorphology of the dendrites only in the electrotonic domain (Carnevale et al., 1995; Tsai et al., 1994). In this thesis, I demonstrated that the complex signaling properties of the anatomically reconstructed motor neurons systematically vary as a function of the physical distance from the soma and fit well to a single exponential function for each propagation direction. The usage of the physical distance instead of abstract variable X would be very useful in interpreting the results from the computational modeling framework in the context of the target neuron in vivo. I believe that the physical distance based representation of the dendritic signaling will benefit to reducing the gap between computational and experimental studies on the dendritic computations.

5.3 PHYSIOLOGICAL REDUCED MODELING FRAMEWORK

The distance-based characterization of the dendritic signaling properties allowed us to develop the physiological reduced modeling framework, where the model parameters are analytically determined to retain the essential electric properties of

the MNs in vivo. The reduced MN model used in this thesis was specified directly from anatomically reconstructed MN models following seven modeling steps:

- 1) Import the anatomical MN data downloaded from www.neuromorpho.org into NEURON software environment.
- 2) Assign the empirically estimated passive membrane properties (i.e. R_m , R_i and C_m) to the anatomical MNs.
- 3) Conduct electrotonic analysis using Impedance class in NEURON (Chapter 2 & 4): the input resistance (R_N) and time constant (τ_m) at the soma, and three signal propagation properties (A_{SD}^{DC} , A_{SD}^{AC} and A_{DS}^{DC}) of the dendrites and morphological factor (p) as a function of the distance from the soma (i.e. D_{path}).
- 4) Determine the location of PIC channels away from the soma to specify D_{path} .
- 5) Choose A_{SD}^{DC} , A_{SD}^{AC} , A_{DS}^{DC} and p at the specified D_{path} from the electrotonic data in the step 3.
- 6) Solve inverse equations (Chapter 4) for the passive membrane parameters ($G_{m,S}$, $G_{m,D}$, $C_{m,S}$, $C_{m,D}$ and G_C) of the reduced model given essential electric properties (R_N , τ_m , A_{SD}^{DC} , A_{SD}^{AC} , A_{DS}^{DC} and p) of the anatomical MNs.
- 7) Assign active membrane mechanisms (i.e. modified Morris-Lecar membrane excitability) to the somatic and dendritic compartment, and adjust maximum conductance density values to generate action and plateau potentials observed experimentally.

It is worth noting that the essential electric properties for the step 5 may also be directly measured from the real MNs using simultaneous whole-cell recordings from the soma and dendrites (Larkum et al., 1996; Stuart et al., 1993).

Alternatively, Hodgkin and Huxley type of membrane mechanisms may also be employed in the step 7 matching the voltage-clamping data for the excitable membrane or voltage-gated ion channels. In this case, the further measurement of the MN properties such as rheobase, AHP properties and effective PIC currents at

the soma might be required to constrain the maximum conductance values of the various types of voltage-gated channels in both somatic and dendritic compartments.

Although the reduced modeling approach has been extensively used to investigate the neuronal dynamics using mathematical analysis, the uniqueness of the model parameter values and the suitability of reduction assumptions have been pointed out. The new reduction method has effectively resolved these issues by analytically solving the inverse problems for the model parameters given essential biophysical properties of single neuron, and by applying two-port theory that allowed us to reflect the electrical structure of the whole dendritic trees. Since the new reduction methodology we have developed is general, I believe that this approach may significantly facilitate the realistic construction and computational exploration of complex neural networks for both physiological and artificial neural systems.

5.4 BIOPHYSICAL PRINCIPLE UNDERLYING MOTOR NEURON BISTABILITY

The nonlinear (i.e. bistable) firing behaviour observed at the soma of the spinal MNs has been clearly shown to be mediated by plateau potentials that are generated by the activation of persistent inward current (PIC) channels in the dendrites. The analysis of the reduced modeling framework reflecting the physiological signaling properties of the dendrites gave us an insight into the underlying biophysical principle of the MN bistability. The critical factor to determine the bistability turned out to be the local excitability over the passive dendrites, that could be modulated by the complex signaling properties between the soma and dendrites. For instance, the local input resistance in the dendrites was tightly correlated to the asymmetric DC signaling as well as the input resistance at the soma. The frequency response of the dendrites was also significant in determining the dendritic impedance level. Thus in order to get the

reduced MN model fully bistable, the values of the three dendritic signaling parameters (i.e. V_{SD}^{DC} , V_{SD}^{AC} and V_{DS}^{DC}) must be confined in the isolated parameter space that could hold the local excitability of the dendrites in an appropriate level (i.e. not too low and high for the delayed onset of plateau potentials). This was why to generate bistable firing behaviour the PIC channels should be distributed over the intermediate distance range (e.g. 300-850 μm) away from the soma in the anatomically reconstructed MN model (Elbasiouny et al., 2005). Hence the spatially distributed and passively manageable excitability over the complex dendritic trees seems to be an optimal design principle to minimize the energy expenditure for maintaining variety in active membrane mechanisms in neurons. I propose that all three dendritic signaling properties determining the excitability of the dendrites should be considered in the physiological reduced modeling. The new reduced modeling may be used as a minimal neuron model for the neural network software or hardware.

5.5 FUTURE WORKS: REALISTIC MOTOR UNIT POOL MODELING

The theoretical reduced modeling framework developed in this thesis may provide a kind of abstract template that can be instantiated to several hundreds of individual motor neurons with different membrane properties that consist of a heterogeneous motor neuron pool in the spinal cord.

Realization of theoretical MN model: For the realistic instantiation, it is first necessary to know how significantly the input-output properties of the reduced model are different from its corresponding complex MN. Recently, this issue has been investigated comparing the physiological bistable firing behaviour of an anatomically reconstructed MN (Elbasiouny et al., 2005) to the reduced case. The types and kinetics of all voltage-gated ion channels used in the anatomical model were applied identically to the reduced model, except the maximum conductances

that were adjusted to match the whole-cell properties such as rheobase (I_{rheo}), afterhyperpolarization (AHP) and effective PIC ($I_{N,\text{PIC}}$). The distance (D_{path}) for the separation of two compartments was chosen to the location (in average 600 μm from the soma) of PIC channels that was used to produce bistable firing behaviour in the anatomical case. The cable parameters of the reduced model were analytically determined using inverse equations to retain R_N , τ_m , $V_{\text{ASD}}^{\text{DC}}$, $V_{\text{ASD}}^{\text{AC}}$ and $V_{\text{ADS}}^{\text{DC}}$ of the original cell, where three dendritic signaling factors were measured directly from the anatomical model at $D_{\text{path}} = 600 \mu\text{m}$ from the soma. The maximum conductances for spiking at the soma were first numerically determined to match I_{rheo} and AHP of the anatomical model, and then $I_{N,\text{PIC}}$ constrained the maximum conductance of L-type Cav1.3 channels for plateau potentials at the dendrites. The firing output pattern (e.g. initial firing rates, primary and secondary slope, and overall shape of frequency hysteresis) of the reduced model to the same triangular current stimulation was amazingly similar to that of the anatomical model. This result showed not only the possible realization of the theoretical modeling framework, but also that the dendritic signaling properties identified in this thesis are essential to determine the bistable firing output in MNs. This study was presented in the Motoneuron Meeting in Paris (Kim and Jones, 2010).

Assignment of type-related electrical properties to the realistic reduced MNs: In the spinal cord of mammalian animals, electrical properties of MNs are not discrete but continuously change over different motor unit types (i.e. S-, FR- and FF types). Some electrical properties such as R_N , τ_m and I_{rheo} have been reported to be strongly correlated with MN types in a broad range of values: $0.4 < R_N < 4.0 \text{ M}\Omega$, $5 < \tau_m < 17 \text{ ms}$ and $3 < I_{\text{rheo}} < 40 \text{ nA}$ (Zengel et al., 1985). In particular, R_N has been shown to be proportionally related to τ_m whereas inversely to I_{rheo} . In addition, $V_{\text{ASD}}^{\text{DC}}$, $V_{\text{ASD}}^{\text{AC}}$ and $V_{\text{ADS}}^{\text{DC}}$ at a particular D_{path} have been shown to vary as a function of R_N that determined the voltage decay coefficient (η) for each signaling property. This dependency on R_N has facilitated the automation of realistic MN pool modeling, by allowing to formulate all essential biophysical

properties as a function of two variables (R_N and D_{path}) with a noise factor (e.g. zero mean Gaussian randomness) that represents the variance of values at a particular R_N and D_{path} . However little has been known about the distribution of D_{path} over the MN pool that indicates the location of plateau potential generating PIC channels in the dendrites. Our preliminary result using the unified formulation scheme has suggested that there were strong interactions between the biophysical parameters that distinguish motor neurons of different types, the localization of PICs and nonlinear firing patterns (Kim and Jones, 2010).

Construction of a motor unit pool model: In order to complete modeling of a single MN pool, the distribution of the number of MNs over the range of R_N must be specified to control the composition of MN types in the pool (e.g. the number of S-type MNs \gg FR-type $>$ FF-type). Then incorporating the type specific firing-force muscle models including nonlinearities in muscle force output (Sandercock and Heckman, 2001), the motor unit pool model may be efficiently implemented under the object-oriented, distributed-computing software design paradigm with a database application. The global pattern of the motor unit pool dynamics may be characterized while varying key bifurcation parameters (e.g. excitatory and inhibitory synaptic inputs, spatiotemporal properties of voltage-gated ion channels and level of neuromodulation) based on the nonlinear dynamical systems theory (Siegel, 1990).

Importance of the realistic motor unit pool model: The bistable firing behaviour has been suggested to systematically vary over the different types of MNs within the MN pool (Lee and Heckman, 1998a; Lee and Heckman, 1998b). Furthermore it has become clear that neuromodulatory control of voltage gated channels in MN dendrites is essential in specifying both their basic electrical properties and their nonlinear dynamics. However these physiological properties influencing the MN dynamics has been ignored in models of the pool of motor units forming a single muscle to investigate motor control mechanisms in the spinal cord (Fuglevand et al., 1993; Heckman and Binder, 1991). The biophysically-plausible,

physiologically–realistic motor unit pool model seems to be essential to investigate the fundamental issue in movement science: how MNs convert synaptic inputs to action potentials that generate excitation and contraction in skeletal muscle fibers. The realistic modeling of the motor units is a critical step for reverse–engineering the structure and organization of motor commands in normal and pathological states. This has also implications for the field of biomimetic robotics with multi-body dynamics and brain-machine interfaces.

5.6 BIBLIOGRAPHY FOR CHAPTER 5

Carnevale, N. T., Tsai, K. Y., Claiborne, B. J., and Brown, T. H. (1995). The electronic transformation: a tool for relating neuronal form and function. *Advances in Neural Information Processing* 7, 69 - 76.

Elbasiouny, S. M., Bennett, D. J., and Mushahwar, V. K. (2005). Simulation of dendritic CaV1.3 channels in cat lumbar motoneurons: spatial distribution. *J Neurophysiol* 94, 3961-3974.

Fuglevand, A. J., Winter, D. A., and Patla, A. E. (1993). Models of recruitment and rate coding organization in motor-unit pools. *J Neurophysiol* 70, 2470-2488.

Heckman, C. J., and Binder, M. D. (1991). Computer simulation of the steady-state input-output function of the cat medial gastrocnemius motoneuron pool. *J Neurophysiol* 65, 952-967.

Kim, H., and Jones, K. E. (2010). A realistic reduced modeling approach for dynamic simulations of spinal motor neuron pool. *Motoneuron Meeting in Paris*, July 9-13.

Larkum, M. E., Rioult, M. G., and Luscher, H. R. (1996). Propagation of action potentials in the dendrites of neurons from rat spinal cord slice cultures. *J Neurophysiol* 75, 154-170.

- Lee, R. H., and Heckman, C. J. (1998a). Bistability in spinal motoneurons in vivo: systematic variations in persistent inward currents. *J Neurophysiol* 80, 583-593.
- Lee, R. H., and Heckman, C. J. (1998b). Bistability in spinal motoneurons in vivo: systematic variations in rhythmic firing patterns. *J Neurophysiol* 80, 572-582.
- Sandercock, T. G., and Heckman, C. J. (2001). Whole muscle length-tension properties vary with recruitment and rate modulation in areflexive cat soleus. *J Neurophysiol* 85, 1033-1038.
- Siegel, R. M. (1990). Non-linear dynamical system theory and primary visual cortical processing. *Physica D* 42, 385-395.
- Stuart, G. J., Dodt, H. U., and Sakmann, B. (1993). Patch-clamp recordings from the soma and dendrites of neurons in brain slices using infrared video microscopy. *Pflugers Arch* 423, 511-518.
- Tsai, K. Y., Carnevale, N. T., Claiborne, B. J., and Brown, T. H. (1994). Efficient mapping from neuroanatomical to electrotonic space. *Network: Computation in Neural Systems* 5, 21 - 46
- Zengel, J. E., Reid, S. A., Sybert, G. W., and Munson, J. B. (1985). Membrane electrical properties and prediction of motor-unit type of medial gastrocnemius motoneurons in the cat. *J Neurophysiol* 53, 1323-1344.